論文 / 著書情報
Article / Book Information

題目(和文)	Ca3PbOにおける三次元ディラック電子の観測
Title(English)	Observation of Three-Dimensional Dirac Fermions in Ca3PbO
著者(和文)	小畑由紀子
Author(English)	Yukiko Obata
出典(和文)	学位:博士(理学), 学位授与機関:東京工業大学, 報告番号:甲第10750号, 授与年月日:2018年3月26日, 学位の種別:課程博士, 審査員:細野 秀雄,川路 均,平松 秀典,中辻 寛,松石 聡
Citation(English)	Degree:Doctor (Science), Conferring organization: Tokyo Institute of Technology, Report number:甲第10750号, Conferred date:2018/3/26, Degree Type:Course doctor, Examiner:細野 秀雄,川路 均,平松 秀典,中辻 寛,松石 聡
学位種別(和文)	博士論文
Type(English)	Doctoral Thesis

Observation of Three-Dimensional Dirac Fermions in Ca_3PbO

Yukiko Obata
2018
Department of Materials Science and Engineering
Interdisciplinary Graduate School of Science and Engineering
Tokyo Institute of Technology

Contents

Chapter 1 General Introduction

Before discussing each chapter showing experiments on three-dimensional Dirac fermion system Ca_3PbO, in this first chapter, the relevant theoretical backgrounds are briefly introduced.

1.1. Berry phase and Berry curvature

The Berry phase [1] has become one of the key concepts in diverse branches of physics. Over the last three decades, it has been gradually realized that the Berry phase of the electronic wave functions can have a substantial impact on material properties and play a key role in a variety of phenomena [2] including polarization [3,4], orbital magnetism [5–7], and various (quantum [8–10], anomalous [11,12], or spin [13–16]) Hall effects. The Berry phase can be regarded as the Aharonov-Bohm phase of a charged particle traveling along a loop including a magnetic flux, whereas the Berry curvature, a vector quantity related to the Berry phase by integration, can be regarded as an effective magnetic flux density (or magnetic field) in a parameter space (***k***-space for our interests) [2]. In particular, the notion of Berry phase is crucial for the understanding of topological phenomena. [17,18]. The following discussions in this section (1.1) are based on Ref. [2]. We first discuss how the Berry phase emerges during the adiabatic evolution of a quantum state. Then we look at the local description of the Berry phase in terms of the Berry curvature.

We consider a Bloch Hamiltonian describing the electrons in a solid, spanned by a set of adiabatic, time-dependent parameters, represented by $\boldsymbol{k} = (k_1, k_2, \ldots)$, i.e.,

$$H = H(\boldsymbol{k}), \boldsymbol{k} = \boldsymbol{k}(t) \tag{1.1}$$

The Schrödinger equation for this system is written such that

$$H(\boldsymbol{k})|u_n(\boldsymbol{k})\rangle = E_n(\boldsymbol{k})|u_n(\boldsymbol{k})\rangle \tag{1.2}$$

where $|u_n(\boldsymbol{k})\rangle$ is the *n*th Bloch state described by a function that is smooth and single valued along a path *C* in $\boldsymbol{k}$ space. Suppose that $\boldsymbol{k}$ travels from $\boldsymbol{k}_0$ $(\boldsymbol{k}(0) = \boldsymbol{k}_0)$ and returns to its original value $\boldsymbol{k}(T) = \boldsymbol{k}_0$ along a closed loop *C*. The wave function $|\psi_n(t)\rangle$ can be expressed as follows.

$$|\psi_n(t)\rangle = e^{i\gamma_n(t)} \exp\left[-\frac{i}{\hbar}\int_0^t dt' E_n\,\boldsymbol{k}(t')\right] \left|u_n\big(\boldsymbol{k}(t')\big)\right\rangle \tag{1.3}$$

Where the second exponential represents the dynamical phase factor. Plugging Eq. (1.3) into the time-dependent Schrödinger equation

$$i\,\hbar\frac{\partial}{\partial t}|\psi_n(t)\Big\rangle = H\big(\boldsymbol{k}(t)\big)|\psi_n(t)\rangle \tag{1.4}$$

and multiplying it from the left by $\left\langle n\big(\boldsymbol{k}(t)\big)\right|$, we find that $\gamma_n(t)$ can be described as a path integral in the $\boldsymbol{k}$ space as follows.

$$\gamma_n(t) = \oint_C d\boldsymbol{k} \cdot \boldsymbol{A}_n(\boldsymbol{k}) \tag{1.5}$$

where $\boldsymbol{A}_n(\boldsymbol{k})$ is a vector-quantity function

$$\boldsymbol{A}_n(\boldsymbol{k}) = i\langle u_n(\boldsymbol{k})|\nabla_{\boldsymbol{k}}|u_n(\boldsymbol{k})\rangle \tag{1.6}$$

This vector $\boldsymbol{A}_n(\boldsymbol{k})$ is defined as the Berry connection or the Berry vector potential in $\boldsymbol{k}$ space. Equation (1.5) demonstrates that in addition to the dynamical phase factor, the physical system obtains the Berry phase $\gamma_n(t)$. Furthermore, the rotation of $\gamma_n(t)$ is the Berry curvature

$$\boldsymbol{\Omega}_n(\boldsymbol{k}) = \nabla_{\boldsymbol{k}} \times \boldsymbol{A}_n(\boldsymbol{k}) \tag{1.7}$$

Inserting the Eq. (1.7) into Eq. (1.5) and using Stokes's theorem, we obtain another expression for $\gamma_n(t)$

$$\gamma_n(t) = \int_S d\boldsymbol{S} \cdot \boldsymbol{\Omega}_n(\boldsymbol{k}) \tag{1.8}$$

Since the Berry curvature is expressed as $\boldsymbol{\Omega}_n(\boldsymbol{k}) = \nabla_{\boldsymbol{k}} \times \boldsymbol{A}_n(\boldsymbol{k})$, $\gamma_n(t)$ and $\boldsymbol{\Omega}_n(\boldsymbol{k})$ can be regarded as the magnetic flux and magnetic flux density (or magnetic field), respectively.

Apparently, $\boldsymbol{A}_n(\boldsymbol{k})$ depends on the gauge $\xi(\boldsymbol{k})$. By transforming the Bloch function

$$\left|u_n\big(\boldsymbol{k}(t)\big)\right\rangle \rightarrow e^{i\xi(\boldsymbol{k})}\left|u_n\big(\boldsymbol{k}(t)\big)\right\rangle \tag{1.9}$$

$\boldsymbol{A}_n(\boldsymbol{k})$ changes as

$$\boldsymbol{A}_n(\boldsymbol{k}) \rightarrow \boldsymbol{A}_n(\boldsymbol{k}) - \frac{\partial}{\partial \boldsymbol{k}}\xi(\boldsymbol{k}) \tag{1.10}$$

Subsequently, $\gamma_n(t)$ described by Eq. (1.5) will be transformed by the change in the gauge $\xi\big(\boldsymbol{k}(0)\big) - \xi\big(\boldsymbol{k}(T)\big)$, where $\boldsymbol{k}(0)$ and $\boldsymbol{k}(T)$ represent the initial and final positions on a closed path *C*. It is important to remember that the phase of the basis function $\left|u_n\big(\boldsymbol{k}(t)\big)\right\rangle$ is single valued. This requires $e^{i\xi(\boldsymbol{k})}$, shown in Eq. (1.9), to be also single valued. From this requirement, Berry predicted [1]

$$\xi\big(\boldsymbol{k}(0)\big) - \xi\big(\boldsymbol{k}(T)\big) = 2\pi \times \text{integer} \tag{1.11}$$

This suggests that $\gamma_n(t)$ can be only transformed by $2\pi n$, where n is an integer, through the change in the gauge and that it cannot be canceled out. Thus, for a closed path *C*, $\gamma_n(t)$ is a gauge-invariant physical quantity and so is $\boldsymbol{\Omega}_n(\boldsymbol{k})$.

In general, one can produce a closed path in the $\boldsymbol{k}$ space by applying either a magnetic field or an electric field. In case of using a magnetic field, we can generate a cyclotron motion of electrons along a closed orbit in the $\boldsymbol{k}$ space. This way the Berry phase can be observed in various magneto-oscillatory experiments [19–21], which have been reported in $LaRuIn_5$ [22] and more recently graphene [23–25].

To understand how the Berry phase is calculated, we consider the following simple Bloch Hamiltonian describing the two-band model of the electrons in a crystal,

$$H(\boldsymbol{k}) = \boldsymbol{d}(\boldsymbol{k}) \cdot \boldsymbol{\sigma} \tag{1.12}$$

where $\boldsymbol{\sigma}$ are the Pauli matrices and $\boldsymbol{d}(\boldsymbol{k})$ is a vector that parameterizes the Hamiltonian. In particular, we focus on the case of linear energy-momentum dispersion $\boldsymbol{d}(\boldsymbol{k}) = \boldsymbol{k}$, i.e. Dirac dispersion. In this case, the calculation of the Berry curvature simply gives

$$\boldsymbol{\Omega}_n(\boldsymbol{k}) = \pm\frac{1}{2}\frac{\boldsymbol{k}}{k^3} \tag{1.13}$$

where the positive and negative signs represent lower and upper bands, respectively. Dirac [26] interpreted that Eq. (1.13) represents the field produced by a monopole at $\boldsymbol{k} = 0$, where the two energy levels become degenerate, implying the emergence of the Dirac points. Integrating the Berry curvature around a sphere encompassing the Dirac point yields

$$\frac{1}{2\pi}\int_S d\boldsymbol{S} \cdot \boldsymbol{\Omega}_n(\boldsymbol{k}) = \pm 1 \tag{1.14}$$

This suggests that the Dirac point can be viewed as the magnetic monopoles and anti-monopoles in $\boldsymbol{k}$-space. Equation (1.14) further implies that the Berry curvature over a closed manifold is quantized in the units of 2π and represents the total number of monopoles inside the manifold. This number is defined as the Chern number.

1.2. Bulk-boundary correspondence

One of the fundamental concepts of topological phenomena is the bulk-boundary correspondence. We consider a bulk system at its boundary, which breaks the crystal symmetry of the bulk. To make up for the broken symmetry at the boundary, the edge state is needed so that the whole system, combining bulk and edge, can recover the

symmetry. The bulk states in topological systems are known to be robust against perturbations, and so are the edge states owing to the bulk-boundary correspondence. This concept underlies various topological phenomena, and several examples are described below. The discussions are based on references [17,27–29].

1.2.1. 2D quantum Hall state

1.2.1.1. Bulk state

The 2D quantum Hall (QH) state is a good example to start off our discussions. For convenience, we let $\hbar = \mathrm{c} = 1$. Suppose that an electrical field E_y is applied along *y*-axis. Following the arguments in Ref. [27], we let the vector potential $A_y = -E_y t$. The crystal momentum transforms as follows.

$$\left(k_x, k_y\right) \rightarrow \left(k_x, k_y - E_y t\right) \equiv \boldsymbol{k}(t) \tag{1.15}$$

Thus, the Hamiltonian $H\left(\boldsymbol{k}(t)\right)$ depends on time as well. Subsequently, the electric current $\langle J_x \rangle$ along *x*- axis is calculated as follows.

$$\langle J_x \rangle = -e \sum_{n \le E_F} \int_{\mathrm{BZ}} \frac{d^2k}{(2\pi)^2} \left\langle u^n_{\boldsymbol{k}(t)} \right| \frac{\partial H_{\boldsymbol{k}(t)}}{\partial k_x} \left| u^n_{\boldsymbol{k}(t)} \right\rangle \tag{1.16}$$

$$= ie \sum_{n \le E_F} \int_{\mathrm{BZ}} \frac{d^2k}{(2\pi)^2} \left(\left\langle \frac{\partial u^n_{\boldsymbol{k}(t)}}{\partial k_x} \right| \dot{u}^n_{\boldsymbol{k}(t)} \right\rangle - \left\langle \dot{u}^n_{\boldsymbol{k}(t)} \right| \frac{\partial u^n_{\boldsymbol{k}(t)}}{\partial k_x} \Big\rangle \Big) \tag{1.17}$$

$$= E_y \frac{e^2}{2\pi} \sum_{n \le E_F} \int_{\mathrm{BZ}} \frac{d^2k}{2\pi i} \left(\left\langle \frac{\partial u^n_{\boldsymbol{k}(t)}}{\partial k_x} \middle| \frac{\partial u^n_{\boldsymbol{k}(t)}}{\partial k_y} \right\rangle - \left\langle \frac{\partial u^n_{\boldsymbol{k}(t)}}{\partial k_y} \middle| \frac{\partial u^n_{\boldsymbol{k}(t)}}{\partial k_x} \right\rangle \right) \tag{1.18}$$

$$= E_y \frac{e^2}{2\pi} \sum_{n \le E_F} \int_{\mathrm{BZ}} \frac{d^2k}{2\pi} \Omega_z(\boldsymbol{k}) \tag{1.19}$$

where $\sum_{n \le E_F}$ and $\int_{\mathrm{BZ}} d^2k$ represent the sum of the all the bands below the Fermi level E_F and the crystal momentum integrated over the whole Brillouin zone (BZ), respectively. From the first line to the second line, partial integration and $i\frac{\partial}{\partial t}\left|u^n_{\boldsymbol{k}(t)}\right\rangle = H\left(\boldsymbol{k}(t)\right)\left|u^n_{\boldsymbol{k}(t)}\right\rangle$ are employed. Equation (1.19) demonstrates that the Hall conductivity

σ_{xy} can be expressed as

$$\sigma_{xy} = \frac{e^2}{2\pi}\sum_{n\leq E_F}\int_{\mathrm{BZ}}\frac{d^2k}{2\pi}\Omega_z(\boldsymbol{k}) \tag{1.20}$$

$$\equiv \frac{e^2}{2\pi}N_{ch} \tag{1.21}$$

where N_{ch} represents the Chern number. This equation implies that N_{ch} takes integer values as long as the E_F stays inside the band gap [2]. Thus, σ_{xy} is quantized to a certain integer, remaining intact against external perturbations.

1.2.1.2. Relation to the boundary

Now we discuss the relation between the bulk and the boundary. First we look at an infinite system where only the contribution from the bulk is included. Using the Maxwell's equations and the continuity equation, the current $\langle \boldsymbol{J} \rangle$ and the electron density $\langle \rho_e \rangle$ can be described as follows.

$$\langle J_i \rangle = \sigma_{xy}\sum_j \epsilon_{ij} E_j \tag{1.22}$$

$$\langle \dot{\rho_e} \rangle = \nabla \cdot \langle \boldsymbol{J} \rangle \tag{1.23}$$

$$= \sigma_{xy}\nabla \times \boldsymbol{E} = \sigma_{xy}\frac{\partial B}{\partial t} \tag{1.24}$$

$$\therefore \langle \rho_e \rangle = \sigma_{xy} B \tag{1.25}$$

Next, to understand the effect of the boundary, we consider a semi-infinite system where the region $x \geq 0$ is occupied by quantized Hall states and $x < 0$ by a vacuum. We suppose that the electron confinement potential behaves as a step function. Equations (1.22) and (1.25) are modified as follows.

$$\langle J_i \rangle = \theta(x)\sigma_{xy}\sum_j \epsilon_{ij} E_j \tag{1.26}$$

$$\langle \rho_e \rangle = \theta(x)\sigma_{xy} B \tag{1.27}$$

Subsequently, the continuity equation can be represented as

$$\langle \dot{\rho_e} \rangle + \nabla \cdot \langle \boldsymbol{J} \rangle = \frac{\partial \theta(x)}{\partial x} \sigma_{xy} E_y \tag{1.28}$$

$$= \delta(x) \sigma_{xy} E_y \tag{1.29}$$

$$= \delta(x) \frac{e^2}{2\pi} N_{ch} E_y \tag{1.30}$$

where N_{ch} is given by Eq. (1.21). Thus, the time derivative of the charge in the bulk can be derived by performing spatial integration as follows.

$$\frac{\partial}{\partial t} Q_{\text{bulk}} = L \frac{e^2}{2\pi} N_{ch} E_y \tag{1.31}$$

where $L \ll 1$ represents the length of the system along the *y*-axis. This indicates that the charge is not conserved if we only look at the bulk in the system. Therefore, it is necessary to let the boundary state (or edge state in this case) break the charge conservation through such phenomena as chiral anomaly [30] (Adler-Bell Jackiw anomaly [31,32]) to cancel out the charge variation resulting from the bulk so that the system as a whole (bulk and edge) can maintain the charge conservation.

Due to this bulk edge correspondence, there exist the 1D chiral edge states, as depicted in Fig. 1.1. They are chiral in that the electrons travel in one direction only along the edge. These states are robust against disorder because there exit no states that can be used for backscattering [17]. To calculate the time derivative of the charge in the edge, we start with the linear energy-momentum dispersion relation of the edge state near the E_F as follows [see Fig. 1.1(b)].

$$E_k = v(\delta k_y - eE_y t) \tag{1.32}$$

where δk_y and v represent the momentum measured from the E_F and the fermi velocity, respectively. This shows that the change in the number of carriers ΔN for the time Δt can be expressed as

$$\Delta N = -\frac{v}{|v|} \frac{eE_y \Delta t}{\frac{L}{2\pi}} \tag{1.33}$$

Subsequently, the time derivative of the charge in the edge is

$$\frac{\partial}{\partial t} Q_{\text{edge}} = -e \lim_{\Delta t \to 0} \frac{\Delta N}{\Delta t} = \chi L \frac{e^2}{2\pi} \frac{v}{|v|} E_y \tag{1.34}$$

where χ represents the chirality $\chi = -\text{sgn}(v)$. Therefore, as long as the N_{ch} of such edge states are generated with $\chi = \text{sgn}(N_{ch})$, the conservation of the charge in the whole system (bulk and edge) is maintained. Given that N_{ch} remains intact against perturbations as long as the band gap stays open, the 1D chiral edge states remain intact against perturbations as well.

1.2.2. 2D quantum spin Hall state

The 2D quantum spin Hall (QSH) state, also known as the 2D topological insulator, is analogous to the 2D QH state except for a critical difference: the existence of an external magnetic field. The 2D QH states break the time-reversal symmetry (TRS) owing to the applied magnetic field so that the quantized Hall effect can emerge, whereas the 2D QSH states conserve the TRS [33].

1.2.2.1. In case where S_z is conserved

First, we consider systems where S_z is conserved. Suppose that we have a QH system with spins pointing upward (spin-up) in parallel to the magnetic field *B* applied along $+z$-axis in which the spin-up electrons travel counterclockwise along the edge. Next, we consider a counterpart system with spins pointing downward (spin-down) in parallel to the magnetic field *B* applied along $-z$-axis in which the spin-down electrons travel clockwise along the edge. By overlapping these two systems together, we obtain a TRS system where spin-up and spin-down electrons travel in the opposite directions along the edge, defined as helical state, as depicted in Fig. 1.2. Instead of calculating the

electrical Hall current that does not exist under TRS, we calculate spin Hall current which denotes the difference of spin-up and spin-down currents as follows.

$$\langle J_x^s \rangle = \frac{1}{2e}(\langle J_x^{\uparrow} \rangle - \langle J_x^{\downarrow} \rangle) \tag{1.35}$$

$$= \frac{1}{2e}(\sigma_{xy}^{\uparrow} E_y - \sigma_{xy}^{\downarrow} E_y) \tag{1.36}$$

$$= \sigma_{xy}^{s} E_y \tag{1.37}$$

where σ_{xy}^{s}, N_{Ch}^{S}, $\langle J_x^{\uparrow} \rangle$, and $\langle J_x^{\downarrow} \rangle$ represent the spin Hall conductivity, spin Churn number, spin-up current, and spin-down current, respectively. They are described as follows.

$$\sigma_{xy}^{s} = \frac{1}{2e}(\sigma_{xy}^{\uparrow} - \sigma_{xy}^{\downarrow}) \tag{1.38}$$

$$= \frac{e}{2\pi} N_{\mathrm{Ch}}^{S} \tag{1.39}$$

$$N_{\mathrm{Ch}}^{S} \equiv \frac{1}{2}(N_{\mathrm{Ch}}^{\uparrow} - N_{\mathrm{Ch}}^{\downarrow}) \tag{1.40}$$

$$\langle J_x^{\uparrow} \rangle = \sigma_{xy}^{\uparrow} E_y \tag{1.41}$$

$$= E_y \frac{e^2}{2\pi} N_{\mathrm{Ch}}^{\uparrow} \tag{1.42}$$

$$= E_y \frac{e^2}{2\pi} \sum_{n \le E_F} \int_{\mathrm{BZ}} \frac{d^2k}{2\pi} \Omega_z^{\uparrow}(\boldsymbol{k}) \tag{1.43}$$

$$\langle J_x^{\downarrow} \rangle = \sigma_{xy}^{\downarrow} E_y \tag{1.44}$$

$$= E_y \frac{e^2}{2\pi} N_{\mathrm{Ch}}^{\downarrow} \tag{1.45}$$

$$= E_y \frac{e^2}{2\pi} \sum_{n \le E_F} \int_{\mathrm{BZ}} \frac{d^2k}{2\pi} \Omega_z^{\downarrow}(\boldsymbol{k}) \tag{1.46}$$

Given that S_z is conserved, $N_{\mathrm{Ch}}^{\uparrow}$ and $N_{\mathrm{Ch}}^{\downarrow}$ take integer values, implying that $N_{\mathrm{Ch}}^{S} = \frac{1}{2}(N_{\mathrm{Ch}}^{\uparrow} - N_{\mathrm{Ch}}^{\downarrow})$ also takes integer values because $N_{ch} = N_{\mathrm{Ch}}^{\uparrow} + N_{\mathrm{Ch}}^{\downarrow} = 0$ under TRS. Therefore, the system has $N_{\mathrm{Ch}}^{\uparrow}$ $(= -N_{\mathrm{Ch}}^{\downarrow})$ number of spin-up (spin-down) edge states traveling along the edge, leading to N_{Ch}^{S} number of helical edge states.

1.2.2.2. In case where S_z is not conserved

1.2.2.2.1. Kramers theorem

Next, we consider a system with TRS where S_z is not conserved. In a real material, there generally exist such interactions, notably spin orbital interactions $\boldsymbol{L} \cdot \boldsymbol{S}$ [33,34], that break the conservation of S_z. In this subsection, it is revealed that when the number of helical edge states is odd, the edge states remain gapless, but when it is even, they become gapped, transforming the system into a topologically trivial one. The Kramers pair at the time reversal invariant momentum (TRIM) $\Gamma_i = -\Gamma_i + G$, where G is the reciprocal wave vector, is the key to understanding the gap-opening mechanism.

We consider a TR operator Θ defined as follows

$$\Theta = i\sigma_y K = JK,\ J = \begin{bmatrix} 0 & 1 \\ -1 & 0 \end{bmatrix} \tag{1.48}$$

where K is a complex conjugate operator (an anti-unitary operator) and σ_y is the y-component of the Pauli matrix. Θ acts on $\boldsymbol{L}$ and $\boldsymbol{S}$ as follows.

$$\boldsymbol{L} \mapsto \boldsymbol{L}' = \Theta \boldsymbol{L} \Theta^{-1} = -\boldsymbol{L} \tag{1.49}$$

$$\boldsymbol{S} \mapsto \boldsymbol{S}' = \Theta \boldsymbol{S} \Theta^{-1} = -\boldsymbol{S} \tag{1.50}$$

Thus, if we have a system represented by a Hamiltonian with the spin orbital interaction H_{SO}, Θ acts on H_{SO} as follows.

$$H_{SO} = f(\boldsymbol{k}) \boldsymbol{L} \cdot \boldsymbol{S}, \quad f \in \mathbb{R} \tag{1.49}$$

$$H_{SO} \mapsto \Theta H_{SO} \Theta^{-1} = f(\boldsymbol{k})^* (-\boldsymbol{L}) \cdot (-\boldsymbol{S}) = H_{SO} \tag{1.49}$$

Therefore, the system with the spin orbital interaction is TR-invariant. In general, under TRS, the Bloch Hamiltonian satisfies

$$H(-\boldsymbol{k}) = \Theta H(\boldsymbol{k}) \Theta^{-1} \tag{1.50}$$

$$[H, \Theta] = \Theta H - H\Theta = 0 \tag{1.51}$$

For systems with spin 1/2, the Schrödinger equation is represented as

$$H(\boldsymbol{k})|u(\boldsymbol{k})\rangle = E|u(\boldsymbol{k})\rangle, \tag{1.52}$$

$$|u(\boldsymbol{k})\rangle = \begin{pmatrix} u(\boldsymbol{k})^{\uparrow} \\ u(\boldsymbol{k})^{\downarrow} \end{pmatrix} \tag{1.53}$$

Owing to TR-invariance, the Hamiltonian satisfies

$$\Theta H(\boldsymbol{k})|u(\boldsymbol{k})\rangle = H(\boldsymbol{k})\Theta|u(\boldsymbol{k})\rangle, \tag{1.54}$$

$$= E\Theta|u(\boldsymbol{k})\rangle, \tag{1.55}$$

Thus,

$$\left|u(\boldsymbol{k})^{\Theta}\right\rangle = \Theta|u(\boldsymbol{k})\rangle \tag{1.56}$$

$$H(\boldsymbol{k})\left|u(\boldsymbol{k})^{\Theta}\right\rangle = E\left|u(\boldsymbol{k})^{\Theta}\right\rangle \tag{1.57}$$

This shows that $\left|u(\boldsymbol{k})^{\Theta}\right\rangle$ has the same energy eigenvalue as $|u(\boldsymbol{k})\rangle$. Furthermore,

$$\langle u(\boldsymbol{k})\left|u(\boldsymbol{k})^{\Theta}\right\rangle = (u(\boldsymbol{k})^{*\uparrow}, u(\boldsymbol{k})^{*\downarrow})(i\sigma_y)K\begin{pmatrix} u(\boldsymbol{k})^{\uparrow} \\ u(\boldsymbol{k})^{\downarrow} \end{pmatrix} \tag{1.58}$$

$$= (u(\boldsymbol{k})^{*\uparrow}, u(\boldsymbol{k})^{*\downarrow})\begin{bmatrix} 0 & 1 \\ -1 & 0 \end{bmatrix}\begin{pmatrix} u(\boldsymbol{k})^{*\uparrow} \\ u(\boldsymbol{k})^{*\downarrow} \end{pmatrix} \tag{1.59}$$

$$= (u(\boldsymbol{k})^{*\uparrow}, u(\boldsymbol{k})^{*\downarrow})\begin{pmatrix} u(\boldsymbol{k})^{*\downarrow} \\ -u(\boldsymbol{k})^{*\uparrow} \end{pmatrix} \tag{1.60}$$

$$= u(\boldsymbol{k})^{*\uparrow}u(\boldsymbol{k})^{*\downarrow} - u(\boldsymbol{k})^{*\downarrow}u(\boldsymbol{k})^{*\uparrow} = 0 \tag{1.61}$$

$$E(\boldsymbol{k}, \uparrow) = E(-\boldsymbol{k}, \downarrow) \tag{1.62}$$

At TRIM $\boldsymbol{\Gamma_i}$, $H_{\boldsymbol{\Gamma_i}} = H_{-\boldsymbol{\Gamma_i}+\boldsymbol{G}} = H_{-\boldsymbol{\Gamma_i}}$ is satisfied. Therefore, Eq. (1.61) demonstrates that the system is doubly degenerate at TRIM under TRS (Kramers theorem).

1.2.2.2.2. Z_2 classification

The Kramers degeneracy at TRIM is important for the Z_2 classification. Suppose that the perturbation with TRS is applied to the system. Such perturbation can be induced by the spin orbital coupling $\boldsymbol{L}\cdot\boldsymbol{S}$ which breaks the conservation of S_z while maintaining the TRS of the system. Now we examine whether the edge states remain gapless under the perturbation. The examples for $N_{\mathrm{Ch}}^{S} = 1, 2, 3$ are described in Fig. (1.3).

I. $N_{\mathrm{Ch}}^{S} = 1$: As illustrated in Fig. 1.3(a), the helical states cross at TRIM $\boldsymbol{\Gamma_i}$. Owing to the protection by TRS from the Kramers theorem, the crossing points at TRIM Γ_i remains ungapped under the perturbation.

II. $N_{\mathrm{Ch}}^{S} = 2$: There are two crossing points (black open circles) in Fig. 1.3(b) that are gapped because they are far from TRIM and lack the protection by TRS, consequently resulting in a normal insulator.

III. $N_{\mathrm{Ch}}^{S} = 3$: At least one Kramers pair remains ungapped, thereby allowing the edge states to remain gapless under perturbations.

As the three examples show, the edge states remain gapless if N_{Ch}^{S} is odd, whereas they become gapped if N_{Ch}^{S} is even. With the edge states broken, the system is topologically trivial.

1.2.2.3. Calculation of the Z_2 topological invariant ν

The above graphical discussions are mathematically developed in Ref. [35,36], and now the calculation of the Z_2 topological invariant number ν can be performed. Important consequences derived from the arguments in Ref [35,36] are briefly introduced here. For details, please consult the original papers.

1.2.2.4. With inversion symmetry

We consider a system that has inversion symmetry. The Z_2 topological invariant number ν can be calculated by the following equation.

$$(-1)^{\nu} = \prod_{i=1}^{4} \delta_i = \prod_{i=1}^{4} \prod_{m=1}^{N} \xi_{2m}(\Gamma_i) \tag{1.63}$$

where $\nu = 1(0)$ represents the topologically nontrivial (trivial) state. $\delta_i = \prod_{m=1}^{N} \xi_{2m}(\Gamma_i)$ is assigned to each TRIM $\boldsymbol{\Gamma_i}$ (i $= 1\sim4$ in 2D,

i. e., $(0,0), (0,\pi), (\pi,0), (\pi,\pi))$, and $\xi_{2m} = \xi_{2m-1} = \pm 1$ represents the parity eigenvalue at each TRIM $\boldsymbol{\Gamma_i}$ with m ranging from 1 to N, where 2N is the number of bands below E_F, which is assigned to reside inside the band gap, as illustrated in Figure 1.4. Given that the system has inversion symmetry, the Hamiltonian of the system satisfies

$$H = PHP^{-1} \Leftrightarrow H(-\boldsymbol{k}) = PH(\boldsymbol{k})P^{-1} \tag{1.64}$$

where P is the inversion operator. Equation (1.32) gives

$$H(\boldsymbol{k})|u(\boldsymbol{k})\rangle = E(\boldsymbol{k})|u(\boldsymbol{k})\rangle, \tag{1.65}$$

$$H(-\boldsymbol{k})(P|u(\boldsymbol{k})\rangle) = E(\boldsymbol{k})(P|u(\boldsymbol{k})\rangle) \tag{1.66}$$

This suggests that at TRIM $\boldsymbol{\Gamma_i}$, $|u(\boldsymbol{k})\rangle$ is the simultaneous eigenfunction of both the Hamiltonian $H_{\boldsymbol{\Gamma_i}}$ and the inversion operator P, confirming the existence of parity eigenvalues ξ_{2m} at TRIM $\boldsymbol{\Gamma_i}$.

In addition, since the inversion operator P does not change the spin, Eq. (1.66) implies

$$E(\boldsymbol{k},\uparrow) = E(-\boldsymbol{k},\uparrow) \tag{1.67}$$

In combination with Eq. (1.62), this demonstrates

$$E(\boldsymbol{k},\uparrow) = E(-\boldsymbol{k},\uparrow) = E(\boldsymbol{k},\downarrow) \tag{1.68}$$

Therefore, for the systems with TRS and inversion symmetry, all bands are doubly degenerate so that 2N bands are below E_F. At each doubly degenerate point, the parity eigenvalue is expressed as $\xi_{2m} = \xi_{2m-1} = \pm 1$. Parity eigenvalue ξ only takes ± 1 due to $P^2 = 1$.

1.2.2.5. Band inversion

This gives the essential rule that the Z_2 topological invariant number changes the value as band inversion occurs at some TRIM, leading to the phase transition from a topologically trivial sate to a topologically nontrivial state. Suppose that in a system with

a large lattice constant, the conduction and valence bands at $\boldsymbol{\Gamma_i} = 0$ are *s*-orbital and *p*-orbital like in the beginning, as depicted in Fig. 1.5(a). As the lattice constant *a* decreases, the hopping energy in the system accumulates to the point where the *s*- and *p*-like bands start to invert at TRIM $\boldsymbol{\Gamma_i}$ through the spin orbital coupling $\boldsymbol{L} \cdot \boldsymbol{S}$. Due to the increase in the spin orbital coupling, the gap opens so that the topological invariant number ν can be defined. If an odd number of band inversions occurs at TRIM, from Eq. (1.63), the parity eigenvalues below E_F changes sign, leading to a change in the Z_2 topological invariant number ν, transforming the system from the trivial insulator to topological insulator. The concept of band inversion allows the Z_2 topological invariant number ν to be easily calculated and plays an important role in the exploration for topological materials.

1.2.2.6. Without inversion symmetry

Next we consider a system without inversion symmetry. The formulation for this general case is discussed in Ref. [35]. The Z_2 topological invariant number ν can be calculated as follows.

$$(-1)^{\nu} = \prod_{i=1}^{4} \delta_i \tag{1.69}$$

$$\delta_i = \frac{\sqrt{\det[w(\boldsymbol{\Gamma_i})]}}{Pfw(\boldsymbol{\Gamma_i})} = \pm 1 \tag{1.70}$$

where $w(\boldsymbol{\Gamma_i})$ is a $2N \times 2N$ unitary matrix defined by $w_{mn}(\boldsymbol{k}) = \langle u_m(-\boldsymbol{k})|\Theta|u_n(\boldsymbol{k})\rangle$ (m, n ranges from 1 to 2N), and Pf stands for the Pfaffian, a function defined by antisymmetric matrix with $2N \times 2N$ dimensions. Pf has a property of $(Pf)^2 = 1$, allowing ν to take either 0 or 1. The system with $\nu = 0$ is a trivial insulator, whereas the system with $\nu = 1$ is a topological insulator.

1.2.3. 3D topological insulator

In this section, theoretical backgrounds for the 3D topological insulators (TI) under TRS are briefly introduced. The following discussions in this section (1.2.3) are mainly based on Ref. [28].

1.2.3.1. Bulk-boundary correspondence

Bulk-boundary correspondence also applies to 3D TIs. We consider a bulk system at its boundary surface, which breaks the TRS of the bulk. To make up for the broken TRS at the boundary surface, the surface state is needed so that the whole system, combining bulk and surface, can recover the symmetry. These surface states consist of an odd number of 2D Dirac cones with mass $m_i = 0$, where i represents the i^{th} Dirac cone, giving rise to the half-integer quantized Hall conductivity

$$\sigma_H = \sum_i^{2N-1} \frac{e^2}{2\pi} \frac{m_i}{|m_i|} \tag{1.71}$$

This formula shows that the Hall conductivity remains finite even in the limit $m_i \to 0$. Such a half Hall conductivity has been discussed for a long time in high-energy physics and termed the "parity anomaly" [34,37]. The concept of the parity anomaly was adopted by Haldane in 1988 to explain the emergence of nonzero quantized Hall conductance in 2D materials without an external magnetic field [37]. This broken TRS state on the surface makes up for the broken TRS state in the bulk, thereby recovering the TRS as a whole system.

The theoretical discussions on the bulk edge correspondence of 3D TIs are developed in Ref. [28]. Instead of going over the rigorous mathematical derivations systematically, the fundamental parts are briefly summarized here. Please consult the original paper for details. The essence is that when the boundary is absent, the bulk magneto-electric or topological term $S_\theta \sim \theta \int dt\, d^3x (\boldsymbol{E} \cdot \boldsymbol{B})$ satisfies TRS at $\theta = 0$ in

a trivial insulator and $\theta = \pi$ in a topological insulator. However, when the boundary is included, even for $\theta = \pi$, an extra term $\delta S_\theta \sim \int dt\, d^2x \epsilon_{ijk} A^i \partial^j A^k$ is generated under TR operation, breaking the TRS as long as only bulk is considered. To cancel out the extra term δS_θ, an additional surface term $S_{\theta surf} = -\delta S_\theta$ is needed. The expression exactly turns out to be the one for the 2D Dirac system such that $S_{\theta surf} = -\delta S_\theta \sim -\int dt\, d\boldsymbol{r} \epsilon_{ijk} A^i \partial^j A^k$, confirming the existence of the surface 2D Dirac cones in 3D TI.

1.2.3.2. Parity anomaly

As discussed above, parity anomaly is the key to the emergence of surface states in 3D TIs. In this section, we investigate this concept more carefully. We consider again the following simple expression, introduced in Eq. (1.12), for single 2D massive Dirac Hamiltonian.

$$H(\boldsymbol{k}) = \boldsymbol{d}(\boldsymbol{k}) \cdot \boldsymbol{\sigma} = \lambda(\boldsymbol{\sigma} \times \boldsymbol{k})_z = -m_z \tag{1.72}$$

$$\boldsymbol{d}(\boldsymbol{k}) = (k_y, -k_x, m) \tag{1.73}$$

The first term of Eq. (1.72) represents the Rashba-type SOC, typical for the surface states of 3D TIs. The mass term m is inserted in the second term. As demonstrated in Fig. (1.6), the Hall conductivity can be described as

$$\sigma_{xy} = -\frac{e^2}{h} \int \frac{d^2k}{2\pi} \Omega_z(\boldsymbol{k}) \tag{1.74}$$

$$= \frac{m}{|m|} \frac{e^2}{2h} = \pm \frac{e^2}{2h} \tag{1.75}$$

The Hall conductivity is half quantized in the unit of e^2/h owing to the unit vector $\boldsymbol{d}(\boldsymbol{k})$ which covers only either north or south hemisphere of the unit sphere according to the sign of the mass m. As mentioned above, the half quantized Hall conductivity remains finite in the system even in the limit $m_i \to 0$, consequently breaking the TRS

(parity anomaly).

In addition to the half quantized Hall conductivity, an odd number of Dirac cones is a unique feature that can exist only on the surface of 3D TI. It is not allowed to emerge in the normal 2D system with 1D boundary due to charge conservation. Suppose we have a 2D system with 1D boundary and with only one Dirac cone. The following arguments apply for an odd number of Dirac cones as well. From the discussions in section (1.2.1) for the 2D QH state, there should be the 1D chiral edge state propagating along the boundary (1D edge) so that it makes up for the broken charge conservation in the 2D bulk. However, since now the 2D bulk has half quantized Hall conductivity, the equation of charge accumulation rates, combining bulk and edge contributions, becomes

$$\frac{\partial}{\partial t} Q_{bulk}^{2D} + \frac{\partial}{\partial t} Q_{edge}^{1D} = L \frac{e^2}{h} E_y \left(\frac{m}{2|m|} - \chi\right) \neq 0 \qquad (1.76)$$

where χ represents the chirality of the 1D edge states taking the value of either +1 or -1. Thus, a 2D system with 1D boundary consisting of only one Dirac cone cannot restore the charge conservation even after taking into account the contribution from the 1D chiral edge state. However, charge conservation should be always maintained for any system. Equation (1.75) indicates that the 2D system with boundary must have an even number of Dirac cones (Nielsen-Ninomiya theorem) [38]. For a system with an even number of Dirac cones, charge can be conserved by choosing $\chi = m/|m|$. Therefore, the Hall conductivity of the ordinary 2D systems is allowed to take only the multiples of e^2/h. Furthermore, for systems with TRS, there should exist an equal number of Dirac cones with positive $m > 0$ and negative $m < 0$ signs.

On the other hand, for the 2D surface of 3D TIs, the above constraints are absent because the 2D surface state on the 3D TIs is free from boundary, validating an odd number of Dirac cones with Hall conductivity half quantized in the unit of e^2/h. In

addition, the broken TR state of the 2D surface state is balanced by the TR broken bulk of the 3D TIs, so as a whole system composed of bulk and surface, the TRS is maintained.

1.2.3.3. Calculation of the topological invariant number ν for 3D TI

As demonstrated above, under TRS, the bulk state can be identified by the magneto-electric term $S_\theta \sim \theta \int dt\, d^3x \boldsymbol{E} \cdot \boldsymbol{B}$ with $\theta = 0$ for a trivial insulator and $\theta = \pi$ for a topological insulator, distinguishing the system into two classes (Z_2 classification). Owing to the bulk boundary correspondence, the odd number of Dirac cones is only allowed for the surface states of 3D TIs with $\theta = \pi$. This conclusion is general and valid for the systems with interactions as well [28].

There is a different approach discussed in Ref. [36], which makes easier the calculations of the topological invariant number. The main points are summarized in this section. Please consult the original paper for details. The topological number can be calculated similarly to the case of 2D TIs and are described as follows.

$$(-1)^{\nu_0} = \prod_{i=1}^{8} \delta_i \tag{1.77}$$

$$(-1)^{\nu_j} = \prod_{i=1(j=1,2,3)}^{4} \delta_i \tag{1.78}$$

where δ_i is defined exactly in the same way as in Eq. 1.63.

$$\delta_i = \prod_{m=1}^{N} \xi_{2m}(\boldsymbol{\Gamma_i}) \tag{1.79}$$

with ξ_{2m} $(m = 1 \sim N)$ the parity eigenvalues at TRIM Γ_i. In 3D, there exist eight TRIMS as illustrated in Fig. 1.7 such that

$$\boldsymbol{\Gamma_i} = \frac{(n_1\boldsymbol{G_1} + n_2\boldsymbol{G_2} + n_3\boldsymbol{G_3})}{2} \tag{1.80}$$

where $n_j = 0, 1$ and $\boldsymbol{G}_j$ is the reciprocal vector. Inversion symmetry is assumed in this section. In contrast to the 2D case, there are four topological invariant numbers $\nu_0, \nu_1, \nu_2, \nu_3$, which are normally expressed in the format of $\nu_0; (\nu_1, \nu_2, \nu_3)$. The

topological invariant number ν_0 is the most essential topological invariant number covering all eight TRIMs and determines whether the system is strong TIs ($\nu_0 = 1$) or not ($\nu_0 = 0$). The strong TIs have surface states consisting of odd numbers of Dirac cones in any crystal planes. This Z_2 classification of ν_0 $(= 0, 1)$ coincides with the Z_2 classification of θ $(= 0, \pi)$ in the magneto-electric term. If $\nu_0 = 0$ and other topological invariant numbers ν_1, ν_2, ν_3 which cover only four TRIMs on the plane perpendicular to n_j) are not zero, then the systems are called weak TIs. For example, $0; (1, 0, 0)$ is a weak TI. Weak TIs can be expressed as the stacking of 2D TIs along certain axis. In the case of $0; (1, 0, 0)$, it is stacked along *x*-axis and does not have surface states for some of the crystal planes as illustrated in Fig. 1.7. Weak TIs are not protected against such perturbations as non-magnetic impurities and can become gapped in the surface states due to perturbations. Therefore, they are comparable to trivial insulators.

1.2.4. Topological crystalline insulators

Another type of 3D topological materials is topological crystalline insulators (TCIs) [39]. In TCIs, the surface states are protected by crystal symmetries including mirror symmetry (MS) [40], rotational symmetry C_n [41], and rotational symmetry + time reversal symmetry [39]. In this section, we consider a system protected by MS. The Hamiltonian of the system with MS satisfies

$$H = M_z H M_z^{-1} \Leftrightarrow H(\boldsymbol{k}) = M_z H(\boldsymbol{k}) M_z^{-1} \tag{1.81}$$

where M_z represents the mirror operator that reflects the state with respect to $z = 0$ plane. The mirror operator can be expressed as $M_z = PC_2$, where C_2 and P represent the two-fold rotational operator along *z*-axis and the inversion operator, respectively. For spin 1/2 system, given that $C_2^2 = -1$, $M_z^2 = P^2 C_2^2 = -1$ is satisfied. Thus, the mirror

eigenvalues equal $\pm i$. Due to the M_z operator, the wave function $e^{i\boldsymbol{k}\cdot\boldsymbol{r}} = e^{i(k_x x+k_y y+k_z z)}$ transforms to $e^{i(k_x x+k_y y-k_z z)}$. This is different from TRS operator T and inversion symmetry operator P. Therefore, such equations as Eqs. 1.50 and 1.64 are not allowed as follows.

$$H = M_z H M_z^{-1} \nLeftrightarrow H(-\boldsymbol{k}) = M_z H(\boldsymbol{k}) M_z^{-1} \tag{1.82}$$

However, if $\boldsymbol{k}$ is constrained on the 2D mirror plane ($k_z = 0$ plane), then the following equation is allowed.

$$H = M_z H M_z^{-1} \Leftrightarrow H(\boldsymbol{k}^m) = M_z H(\boldsymbol{k}^m) M_z^{-1} \tag{1.83}$$

where $\boldsymbol{k}^m \equiv (k_x, k_y, 0)$ is fixed on the mirror plane $k_z = 0$. Thus, Eq. (1.83) suggests

$$H(\boldsymbol{k})|u(\boldsymbol{k})\rangle = E(\boldsymbol{k})|u(\boldsymbol{k})\rangle, \tag{1.84}$$

$$H(\boldsymbol{k})(M_z|u(\boldsymbol{k})\rangle) = E(\boldsymbol{k})(M_z|u(\boldsymbol{k})\rangle) \tag{1.85}$$

These results demonstrate that on the mirror plane $k_z = 0$, $|u(\boldsymbol{k}^m)\rangle$ is the simultaneous eigenfunction of both the Hamiltonian $H(\boldsymbol{k}^m)$ and the mirror operator M_z. Therefore, on the mirror plane, the Hamiltonian can be expressed as

$$H(\boldsymbol{k}^m) = \begin{bmatrix} H^{+i}(\boldsymbol{k}^m) & 0 \\ 0 & H^{-i}(\boldsymbol{k}^m) \end{bmatrix} \tag{1.86}$$

Eq. (1.86) implies that the system resembles the case of 2D QSH systems with S_z conserved. Since the degree of freedom for $k_z\ (=0)$ is removed on the mirror plane, the system is now two-dimension so that we can employ the similar arguments developed in 2D QSH systems. The Chern number $N_{ch}^{\pm i}$ can be assigned to each subset Hamiltonian $H^{\pm i}(\boldsymbol{k}^m)$. Under TRS, the total Chern number equals 0, $N_{ch}^{+i} + N_{ch}^{-i} = 0$, so the mirror Chern number $N_{ch}^{m} \equiv (N_{ch}^{+i} - N_{ch}^{-i})/2$ also takes integer. Since the N_{ch}^{+i} subset and N_{ch}^{-i} subset do not mix with each other due to mirror symmetry, there always exist N_{ch}^{+i} (N_{ch}^{-i}) numbers of "right" ("left") moving chiral edge states along the mirror line of projected mirror plane, as illustrated in Fig. 1.8. These chiral edge modes lose the

meaning once they deviate from the mirror plane. However, the crossing points (Dirac points) always exist in the mirror line, as depicted in Fig. 1.8, confirming the existence of Dirac cones on the surface of the system.

1.2.5. Weyl semimetals

The concept of topology is not restricted to "insulators" where the gaps in the bulk remain open. It can be found in gapless systems, which are defined as Weyl semimetals [42–44]. The Weyl semimetal is a semimetal where the bulk valence and conduction bands meet at discreet points, around which nondegenerate 3D Dirac cones composed of even numbers of Weyl nodes emerge. As discussed below, the Weyl nodes can be viewed as the magnetic monopoles and antimonopoles in $\boldsymbol{k}$-space. Therefore, they can be considered as topological materials despite the absence of gaps. In the next subsections, the theoretical backgrounds of Weyl semimetals are briefly summarized. The following discussions are mainly based on Ref. [45]. Please consult the original papers for details.

1.2.5.1. Bulk boundary correspondence

Bulk boundary correspondence also applies to Weyl semimetals. Weyl semimetals can be viewed as the 3D surface states of the hypothetical 4D QH system [46]. As demonstrated in section 1.2.1, charge is not conserved owing to chiral anomaly [30] (Adler-Bell-Jackiw anomaly [31,32]) on the edge of a 2D QH system if only the bulk is considered. The broken charge conservation on the edge is fixed by the chiral 1D edge state so that the whole system, combining 2D bulk and 1D edge, can recover the charge conservation. Similarly, the chiral 3D surface state (Weyl semimetal state) of a 4D QH

system breaks the charge conservation due to chiral anomaly. This anomaly makes up for the broken charge conservation in the 4D bulk, allowing the whole system to recover the charge conservation.

1.2.5.2. Chiral anomaly

Chiral anomaly is, in a nutshell, the broken charge conservation which is expressed by the rate of the charge accumulation on the 3D surface of the 4D QH system as follows [38].

$$\frac{\partial}{\partial t} Q_{surface}^{3D} = g \frac{\partial}{\partial t} Q_{edge}^{1D} = -\chi V \frac{e^3}{h^2} \boldsymbol{E} \cdot \boldsymbol{B} \tag{1.88}$$

where $g = BA/(\frac{h}{e})$ represents the degeneracy of each Landau level with the cross section A of the sample normal to the applied magnetic field B and V represents the volume of the sample. Eq. 1.88 suggests that the broken charge conservation of the 3D surface states is fundamentally equivalent to that of the 1D chiral edge states of the 2D QH systems. This similarity can be understood more clearly from the expressions of the Landau levels of the Weyl semimetals. The Hamiltonian of the Weyl semimetal can be represented as follows [45].

$$H_{Weyl}(\boldsymbol{k}) = \boldsymbol{k} \cdot \boldsymbol{v} \cdot \boldsymbol{\sigma} = \sum_{ij \in x,y,z} v_{ij} k_i \sigma_j \,,\ \chi = \mathrm{sgn}[\det \boldsymbol{v}] \tag{1.89}$$

The Landau levels are expressed as follows [45].

$$E_n = n v_F \sqrt{2|n|eB + (\boldsymbol{k} \cdot \boldsymbol{B})^2},\ n = \pm 1, \pm 2, \pm 3, \ldots \tag{1.90}$$

$$E_0 = -\chi v_F (\boldsymbol{k} \cdot \boldsymbol{B}) \tag{1.91}$$

where E_0 represents the quantum limit. As shown by Eq. (1.91) and Fig. 1.9, the lowest Landau level of Weyl semimetal is chiral in that it linearly disperses along the direction of the applied magnetic field $\boldsymbol{B}$, similar to the case of the 1D edge state with a clear

distinction that it is now degenerate with $g = BA/(\frac{h}{e})$ due to Landau quantization. Therefore, under the magnetic field which is so strong that the lowest Landau level E_0 is occupied, the Eq. 1.88 becomes valid [45]. Furthermore, Eq. 1.88 can be applied to the case of low magnetic field as demonstrated by Ref. [47] by employing semiclassical formulation in which the effects of Berry curvature $\boldsymbol{\Omega_k}$ are incorporated into the Boltzmann transport equation.

1.2.5.3. Weyl semimetals in real 3D bulk

In the previous section, the Weyl semimetal states were viewed as the 3D surface state of the hypothetical 4D QH bulk. However, in reality, there does not exist such materials as 4D bulk; instead, the Weyl semimetals emerge in normal 3D bulk. This leads to some modifications in the previous discussions. First, as an alternative to 4D bulk QH system, an even number of Weyl nodes with equal numbers of opposite chiralities are required to recover the broken charge conservation in the 3D bulk owing to Eq. 1.88 (Nielsen Ninomiya's theorem) [38]. Therefore, in the real 3D bulk system of Weyl semimetals, the total charge is always conserved as follows.

$$\frac{\partial}{\partial t} Q^{3D}_{total} = \frac{\partial}{\partial t} Q^{3D}_{\chi=+1} + \frac{\partial}{\partial t} Q^{3D}_{\chi=-1} = 0 \qquad (1.92)$$

where $\frac{\partial}{\partial t} Q^{3D}_{\chi=\pm 1}$ represents the chiral charge with chirality χ. On the other hand, this charge conservation implies that the chiral charge is not conserved [48] as follows.

$$\frac{\partial}{\partial t} Q^{3D}_{chiral} = \left(\frac{\partial}{\partial t} Q^{3D}_{\chi=+1} - \frac{\partial}{\partial t} Q^{3D}_{\chi=-1}\right)/2 = -V \frac{e^3}{h^2} \boldsymbol{E} \cdot \boldsymbol{B} \quad (1.93)$$

Eq. (1.93) is called "charge pumping effect" [48], which is schematically shown in Fig. 1.10. This effect can be detected as negative magnetoresistance in the real 3D Weyl semimetals.

1.2.6. Dirac semimetals

Weyl semimetals can be realized in materials where either inversion symmetry (IS) or time-reversal symmetry (TRS) is broken. In most of the real materials, however, both IS and TRS exist. Dirac semimetals are close counterparts of Weyl semimetals, possessing linear energy-momentum dispersions in 3D. We consider a system with effective four band model. For each Dirac node, the Hamiltonian can be expressed as follows.

$$H_{Dirac}(\boldsymbol{k}) = \begin{bmatrix} H^{+}_{Weyl}(\boldsymbol{k}) & 0 \\ 0 & H^{-}_{Weyl}(\boldsymbol{k}) \end{bmatrix} \tag{1.94}$$

Eq. (1.94) shows that the Dirac Hamiltonian H_{Dirac} consists of two Weyl nodes $H^{\pm}_{Weyl}(\boldsymbol{k})$ with opposite chirality (monopoles and antimonopoles).

1.2.6.1. Crystal symmetry protection

In the real material with both IS and TRS, however, under external perturbations, the two Weyl nodes mix with each other, leading to gap opening. Thus, Eq. (1.94) is not valid for systems with both IS and TRS. Subsequently, the Hamiltonian should be modified as follows.

$$H_{Dirac}(\boldsymbol{k}) = \begin{bmatrix} H^{+}_{Weyl}(\boldsymbol{k}) & M(\boldsymbol{k}) \\ M^{\dagger}(\boldsymbol{k}) & H^{-}_{Weyl}(\boldsymbol{k}) \end{bmatrix} \tag{1.95}$$

where $M(\boldsymbol{k})$ represents the mixing term. However, if the system possesses additional symmetry that effectively ensures $M(\boldsymbol{k}) = 0$ under perturbation, Eq. (1.94) can stay valid and the system remains ungapped. The general mathematical formulation for systems with rotational symmetry C_n are developed in Ref. [49], which is summarized in Fig. 1.11. For details, please consult the original paper to Ref. [49]. The phase diagram of

Dirac semimetals illustrated in Fig. 1.11 is the generalized version of that for Weyl semimetals demonstrated by Murakami *et al*. in Ref. [27,50–52]. As shown in Fig. 4.1, it can be categorized into three cases. Fig. 1.11(a) shows the case without C_n protection, where the gap can only stay closed at a critical point $m = m_c$ and requires the system to be fine tuned to the point. Thus, it is hardly feasible to achieve the Dirac semimetal phase in materials. Figs. 1.11(b) and (c) demonstrate the cases of stable Dirac semimetals free from such experimental burden. For the case (b), the Dirac nodes exist at TRIM points and are stable regardless of the values of the parameter *m*, exemplified by a hypothetical compound BiO_2 [53]. However, BiO_2 does not exist in reality, and so far, there is no experimental report for the case (b). Fig. 1.11(c) shows the relevant case for Na_3Bi [54] and Cd_3As_2 [55–57], the first two experimental realizations of stable Dirac semimetals. For the case (c), the Dirac semimetal phase is stable for a finite parameter range $m_{c1} < m < m_{c2}$ of the system, meaning that the gap in an insulating phase closes at a TRIM when $m = m_{c1}$ and yields two Dirac nodes along a line which satisfies $R_n\boldsymbol{k} = \boldsymbol{k}$ where R_n denotes the 3×3 matrix representing the $2\pi/n$ rotation. The two Dirac nodes propagate along the line and mix with each other at another TRIM point at $m = m_{c2}$ to open a gap, and the system goes into another insulating phase.

1.3. Objectives and outline of the present studies

Motivated by the theoretical and experimental advances in the studies of Dirac materials, there has been growing interest in the cubic antiperovskite family as potential source of such topological phases as 3D Z_2 topological insulators [58], 3D massive Dirac fermions [59–61], topological crystalline insulators [62,63], and topological superconductors [64]. In particular, recent band calculations on Ca_3PbO [59] predict that

there exists a 3D gapped Dirac fermion at a finite momentum along the Γ-X path in the 3D BZ, which stems from the band inversion of the Ca 3*d* and Pb 6*p* bands at the Γ point, as shown in Fig. 1.12. The primary feature is that the bands comprising the Dirac fermion are the only bands that appear near the E_F, thereby allowing for a simple and straightforward study on 3D Dirac fermions free from the influences of other bands with parabolic dispersions. In addition to the prediction of the 3D Dirac fermion system, another band calculation on Ca_3PbO [62] shows that it is also a candidate for the topological crystalline insulator. More recent band calculations on the surface states of Ca_3PbO [63] predict that there exist kinks and divergences in the surface density of states as signatures of van-Hove singularities. The presence of van Hove singularities in the surface density of states is an interesting feature, which has been confirmed as a key factor in the physics of the high-T_c superconductors, notably cuprates. Given that another antiperovskite oxide, $Sr_{3-x}SnO$, exhibits bulk superconductivity upon hole doping [64], it might be also possible to induce superconductivity on the surface of Ca_3PbO by accurate tuning of the Fermi level, consequently leading to topological superconductivity.

In this study, the following objectives were set to confirm the presence of 3D Dirac fermions in Ca_3PbO.

1. Synthesis of high-purity Ca_3PbO single crystals with low carrier density
2. Observation of the 3D Dirac-like band structure of Ca_3PbO using angle-resolved photoemission spectroscopy (ARPES) measurements
3. Evaluation of magneto-transport properties as signatures of Dirac fermions in Ca_3PbO using Shubnikov-de Haas (SdH) oscillations measurements

This thesis is summarized as follows.

Chapter 1 describes the general introduction and objectives of this study.

Chapter 2 describes the experimental techniques employed in this study.

Chapter 3 describes the flux growth and basic magneto-transport properties of Ca_3PbO single crystals

Chapter 4 describes the ARPES studies on the 3D band structure of Ca_3PbO and the effects of Bi doping on the band width and the Fermi level of Ca_3PbO.

Chapter 5 describes the studies of SdH oscillations in Bi-doped Ca_3PbO.

Chapter 6 summarizes this study.

Figures

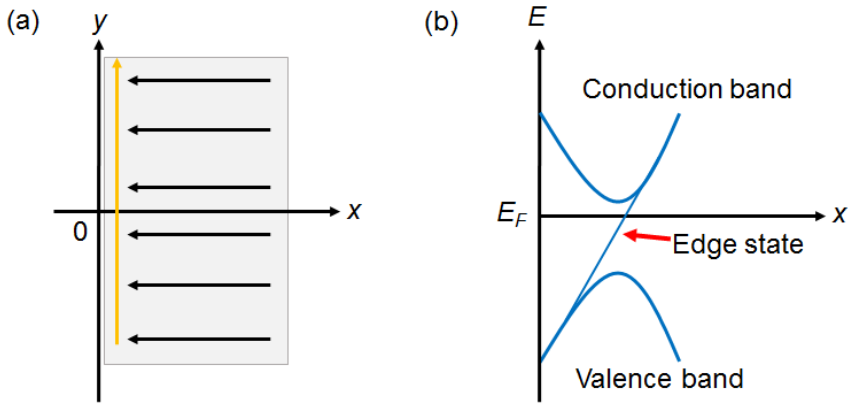

Figure 1.1: Schematics of the edge state in the quantum Hall (QH) system. (a) The semi-infinite QH system emerges in the region $x \geq 0$, whereas the region $x < 0$ is occupied by a vacuum. When the electric field E_y is applied, the Hall current is accumulated into the $x = 0$ edge, leading to the 1D chiral edge state that propagates in one direction along the y-axis. (b) The band dispersion of the edge state.

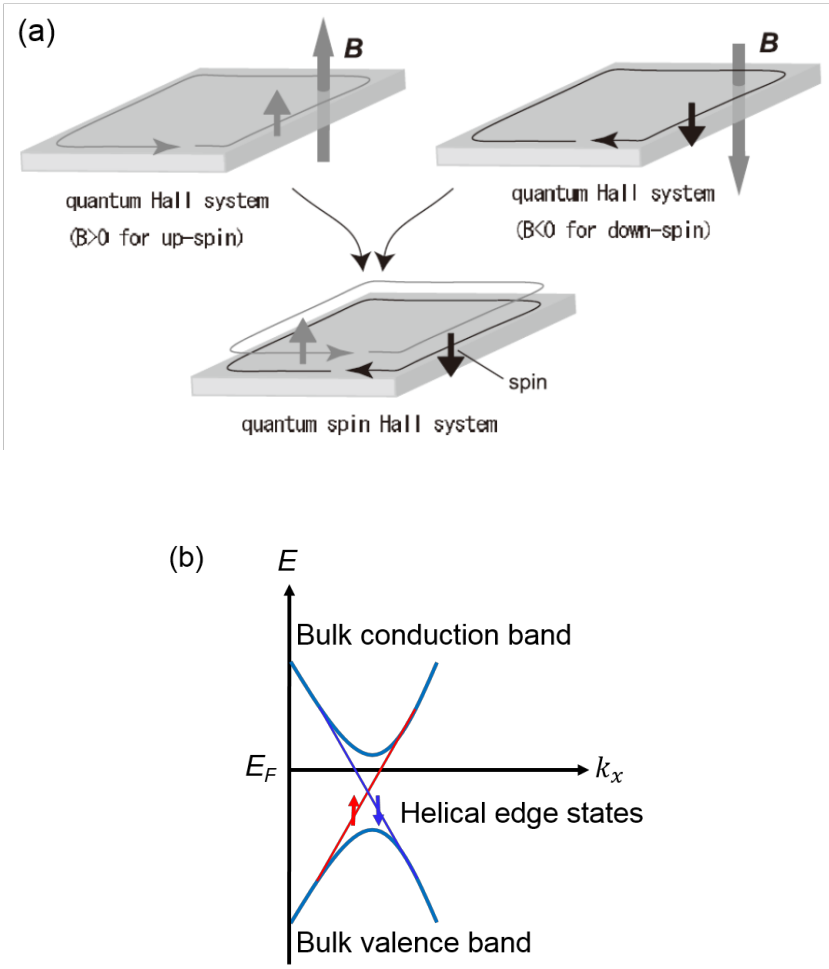

Figure 1.2: (a) Schematic pictures of the QSH system generated by overlapping two QH systems with opposite spins. This figure is adopted from Ref. [27]. (b) Helical edge states. Red and blue lines represent the spin-up and spin-down states, respectively.

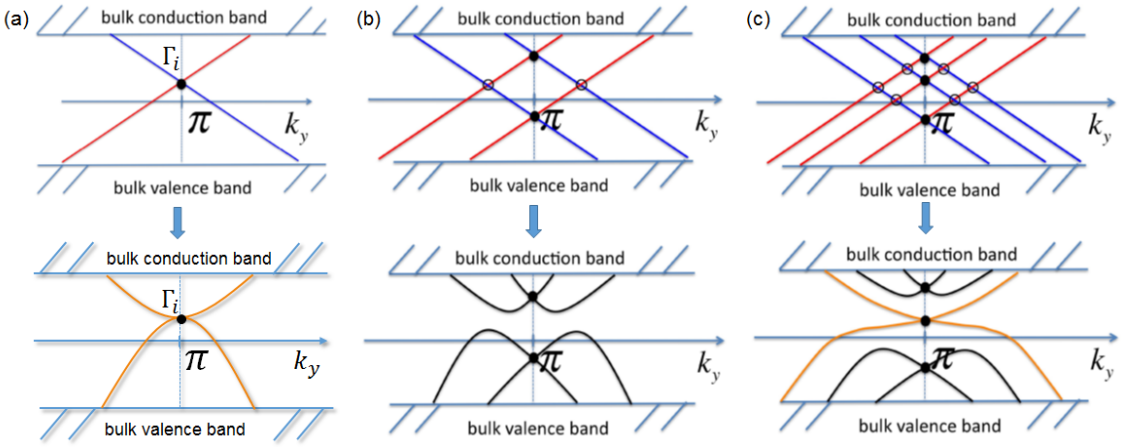

Figure 1.3: (a),(b),(c) Examples of the Z_2 classification for QSH systems with spin orbital coupling for $N_{\mathrm{Ch}}^{s} = 1, 2, 3$, respectively. Red and blue lines represent the spin-up and spin-down bands, respectively. The crossing points illustrated by the black solid and black open circles show Kramers degenerate states at TRIM and non-Kramers degenerate states, respectively. For $N_{\mathrm{Ch}}^{s} = 1, 3$, at least one Kramers pair remains ungapped, demonstrating that the edge states are protected. On the other hand, for $N_{\mathrm{Ch}}^{s} = 2$, The non-Kramers degenerate states become gapped because they are not protected by TRS, and the edge states are broken, resulting in normal insulators. Figures are adopted from Ref [29].

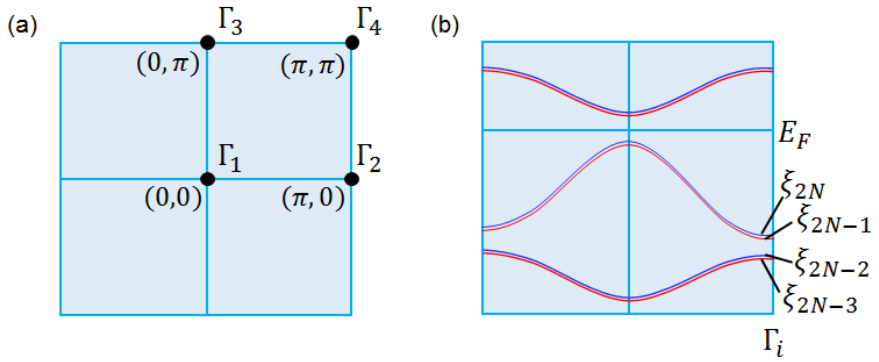

Figure 1.4: Schematics for Eq. 1.63. (a) the 2D BZ. There are four TRIM points$\boldsymbol{\Gamma_i} = (0,0), (0,\pi), (\pi,0), (\pi,\pi)$. (b) The schematic band dispersions. ξ_{2m} $(m = 1\sim N)$ shows the parity eigenvalues at each TRIM $\boldsymbol{\Gamma_i}$, where $2N$ is the number of bands below E_F.

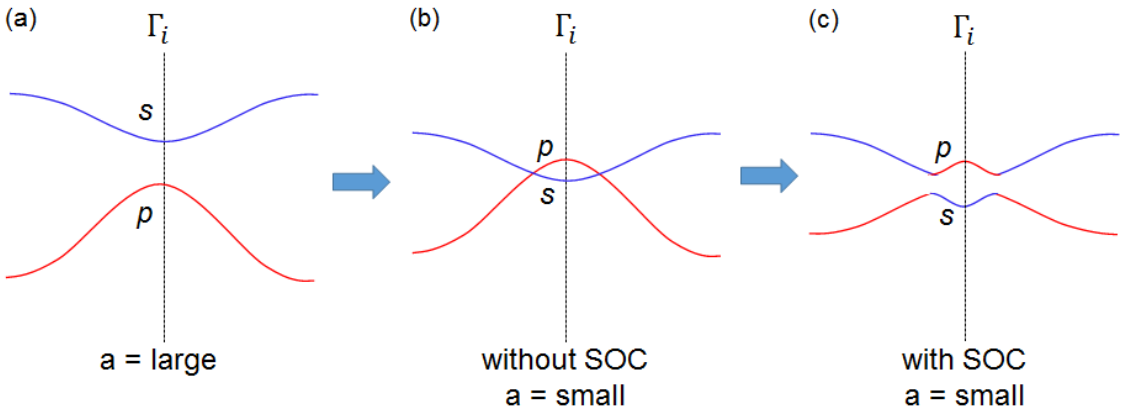

Figure 1.5: Schematic images of band inversion. (a) Band dispersion of a trivial insulator with a large lattice constant *a*. The conduction and valence bands at $\boldsymbol{\Gamma_i = 0}$ are *s*-orbital and *p*- orbital like. (b),(c) Band dispersion without and with spin orbital coupling (SOC) with a small *a*, respectively. Part of the figure is adopted from Ref. [65].

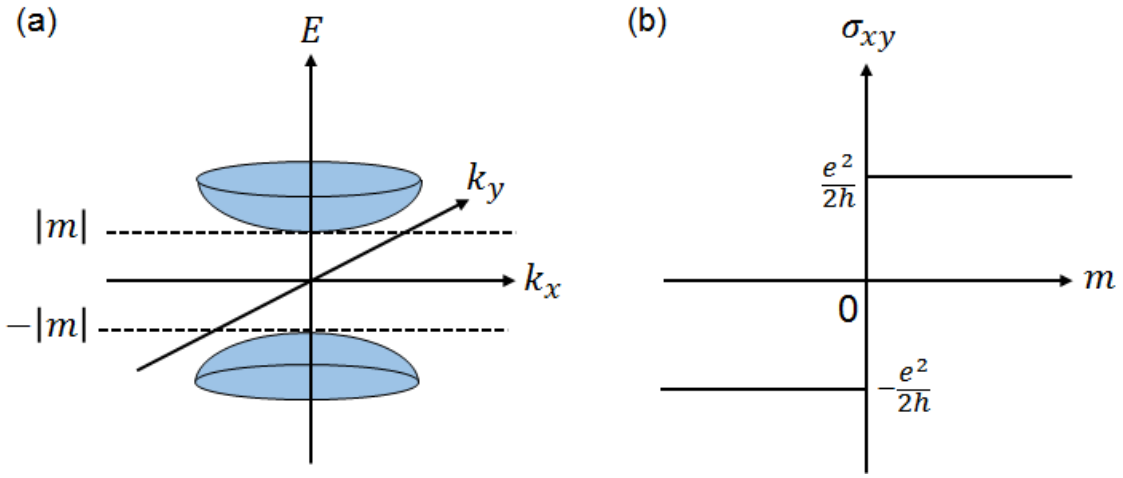

Figure 1.6: Schematic images of 2D massive Dirac dispersion. (a) Massive Dirac band dispersion with a gap of $2|m|$. (b) Half quantized Hall conductivity remains finite even in the limit $m_i \to 0$, consequently breaking the TRS (parity anomaly).

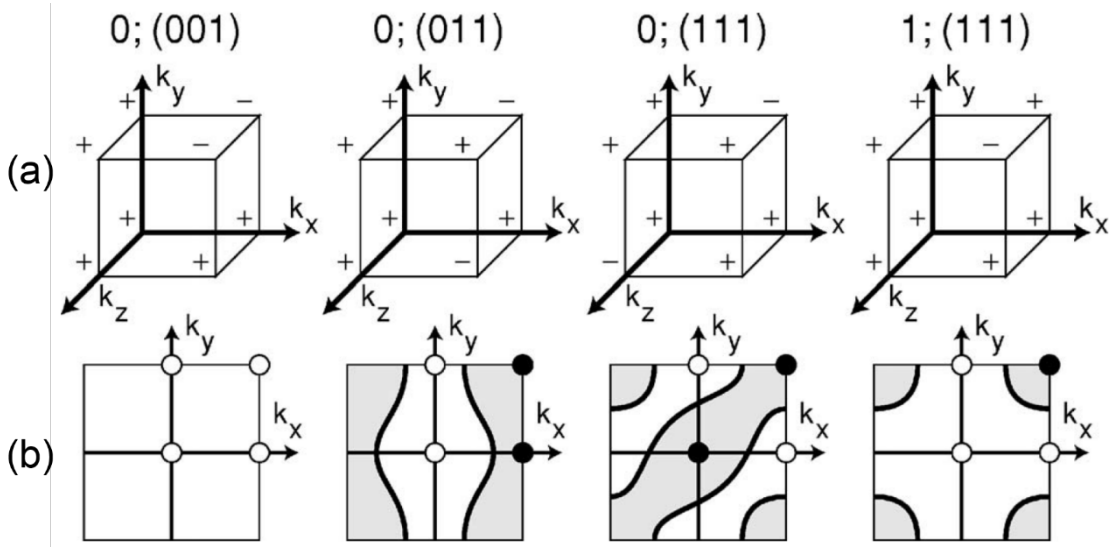

Figure 1.7: Examples illustrating several phases corresponding to $\nu_0; (\nu_1, \nu_2, \nu_3)$. (a) The signs of δ_i at the $\boldsymbol{\Gamma_i}$ points on the vertices of a cube. (b) The Fermi surface on a (001) plane for each phase. The produce of δ_i on the projected planes with open (solid) circles illustrating $\prod_{i=1}^{4} \delta_i = +1(-1)$. Between the open and solid circles, there exist odd numbers of Fermi surfaces. On the other hand, even numbers of Fermi surfaces including 0 between open-open or solid-solid circles. In the right most panel, the odd numbers of Dirac cones exit in any crystal planes. In contrast, the surface states do not appear in the left three panels for some crystal planes. These three panels represent WTIs, where the 2D TIs are aligned along [001], [01-1], [11-1] axis respectively and do not have surface states on the planes normal to these axes. The figures are adopted from Ref. [36].

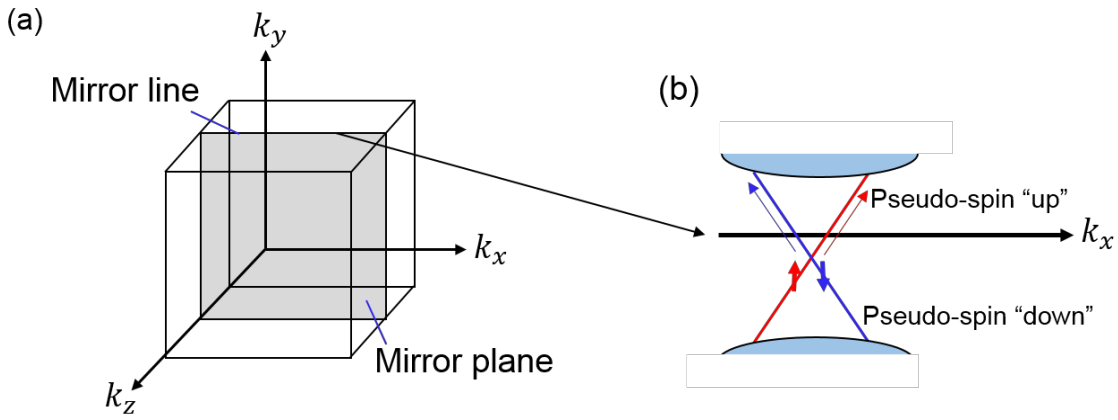

Figure 1.8: Schematic images of (a) the mirror plane at $k_z = 0$ and (b) the surface states composed of the pseudo-spins representing the two mirror eigenvalues $\pm i$ in TCIs. If the crystal is cut along the plane perpendicular to k_y axis, they then the chiral edge modes emerge along the mirror line (k_x axis) on which the mirror plane is projected. Although these chiral edge modes lose the meaning when the $k_{surface}$ deviates from the mirror plane, the crossing points (Dirac points) always emerge because the two chiral edge modes at the mirror line do not mix with each other owing to the protection by mirror symmetry.

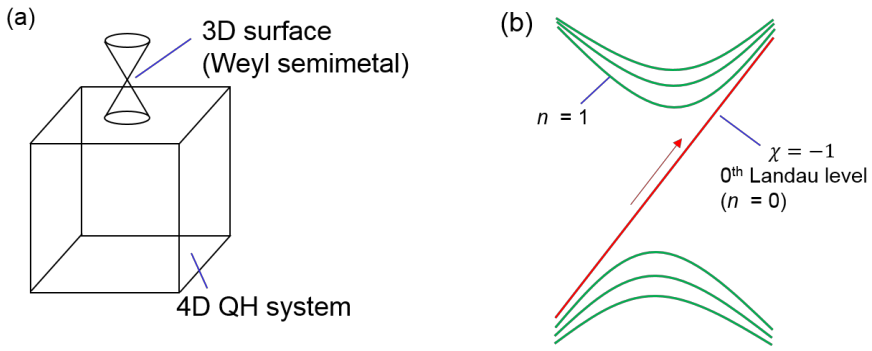

Figure 1.9: Schematic images of Weyl semimetal state. (a) Weyl semimetal state represented by the 3D surface state of the 4D QH state. (b) Landau level spectrum of Weyl semimetal states under magnetic field. The 0th Landau level becomes chiral with chirality χ, accumulating the charge at a rate of $\frac{\partial}{\partial t} Q^{3D}_{surface} = -\chi V \frac{e^3}{h^2} \boldsymbol{E} \cdot \boldsymbol{B}$ (chiral anomaly) which cancels out the broken charge conservation in the 4D bulk so that the charge conservation as a whole system can be recovered.

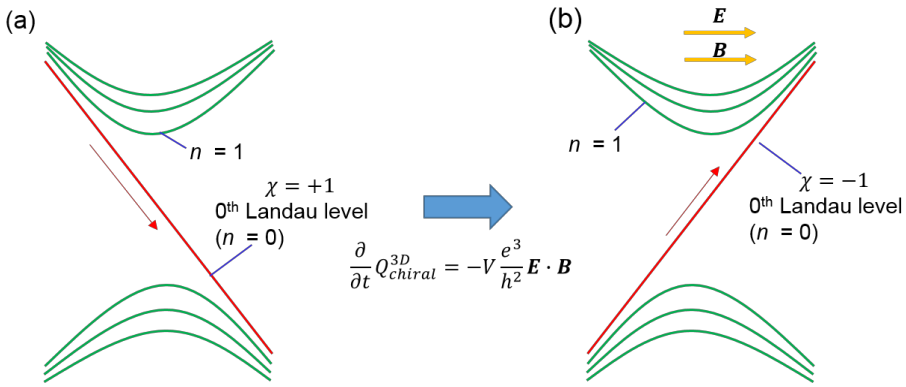

Figure 1.10: Schematic images of chiral anomaly. The charge pumping occurs between (a) the left branch of Weyl node ($\chi = +1$) and (b) the right branch of Weyl node ($\chi = -1$). Under magnetic field $\boldsymbol{B}$, the lowest Landau level is chiral, traveling along the direction of $\boldsymbol{B}$. If the electrical field $\boldsymbol{E}$ is applied parallel to $\boldsymbol{B}$, charge pumping happens.

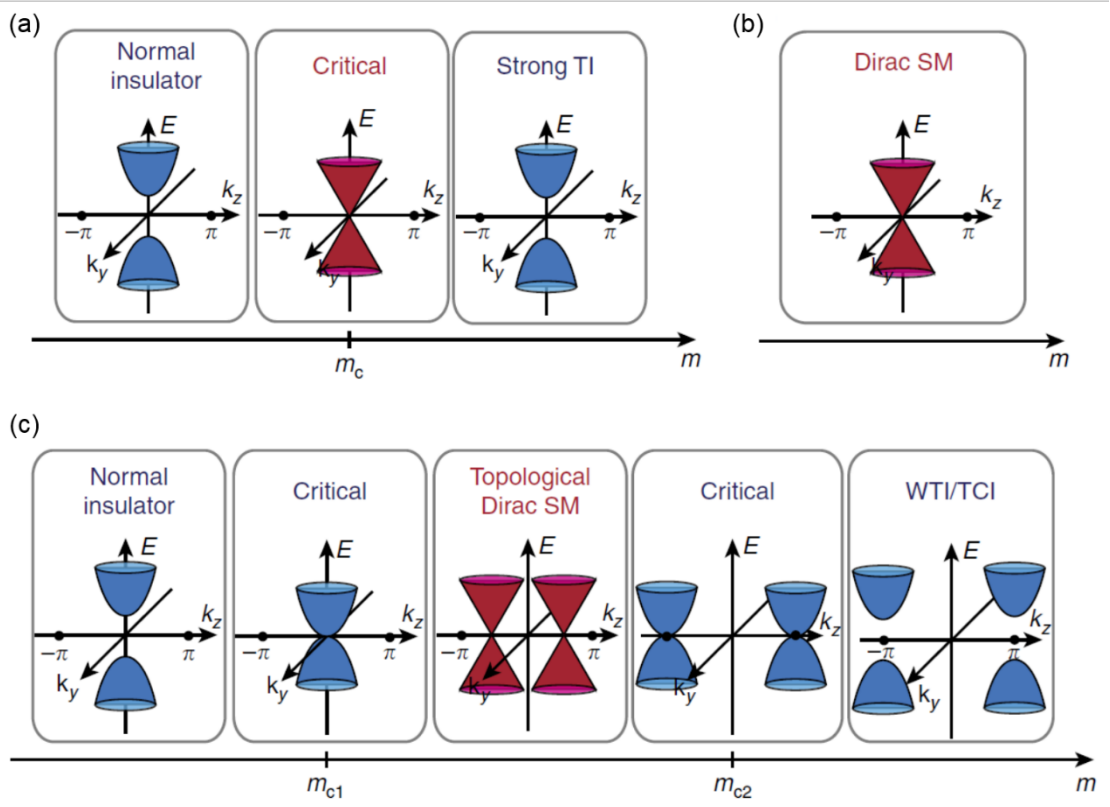

Figure 1.11: Schematic images of Dirac semimetal phases at various cases. (a) The case without crystal symmetry protection, requiring fine tuning of the parameter m. (b) The case where the Dirac nodes exist at the TRIM and remain ungapped due to the rotational symmetry regardless of the value of the parameter m. (c) The case where the Dirac nodes emerge at points other than TRIMs. The figures are adopted from Ref. [49].

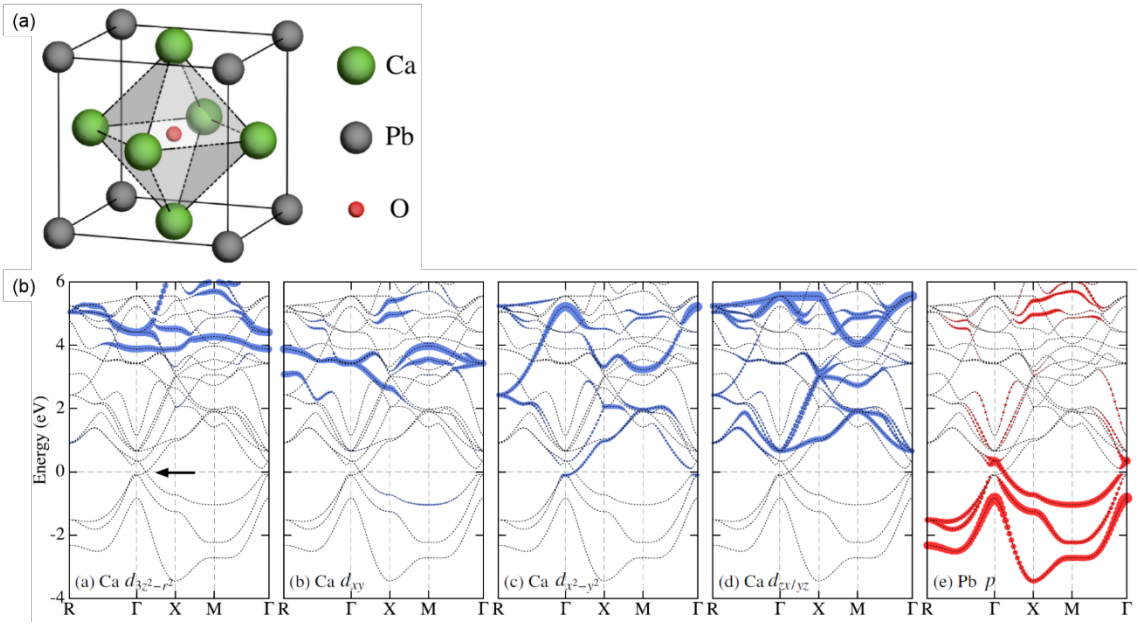

Figure 1.12: (a) Crystal structure and (b) band structure calculations of Ca_3PbO with the distributions of the Ca $d_{3z^2-r^2}$, Ca d_{xy}, Ca $d_{x^2-y^2}$, Ca $d_{zx/yz}$, and Pb p orbital weights. The orbital weights are represented as the width of the bands. The figures are adopted from Ref. [59].

Chapter 2 Experimental Techniques

In this section, we briefly introduce the basic principles of the experimental techniques used in this study.

2.1. Angle-resolved photoemission spectroscopy

Angle-resolved photoemission spectroscopy (ARPES) is one of the most direct experimental techniques to study the electronic structure of solids [66,67]. The phenomenon of photoemission was first observed by Hertz (1887). This was later demonstrated as a manifestation of the quantum nature of light by Einstein (1905), who perceived that when photons of energy $h\nu$ (where ν is the photon frequency) strike a sample surface, an electron can absorb a photon and escape from the material with a maximum kinetic energy $h\nu - \phi$, where ϕ, the material work function, is a measure of the potential barrier at the surface that prevents the electrons of the valence bands from escaping into vacuum. A good approximation of the photoemission process can be expressed by the three-step model, as shown in Fig. 2.1(a).

1. An electron in the valence band of the bulk is first excited by the photon.
2. The excited electron travels to the surface.
3. The photoelectron escapes from the sample into the vacuum.

After a photoelectron escapes into the vacuum, it is being collected with an electron energy analyzer as a function of its kinetic energy E_{kin} for a given emission angle θ. This way, we can determine the photoelectron momentum $\boldsymbol{p}$ from its kinetic energy by

$$E_{\mathrm{kin}} = \frac{\boldsymbol{p}^2}{2m} \tag{2.1}$$

$$\boldsymbol{p} = \sqrt{2mE_{\mathrm{kin}}} \tag{2.2}$$

The direction of $\boldsymbol{p}/\hbar$ is obtained from θ and φ which are the the polar and azimuthal emission angles under which the electrons escape from the surface (Fig. 2.1(b)).

Within the non-interacting electron picture, and by applying total energy and momentum conservation laws, we can relate the kinetic energy and in-plane momentum (k_{x} and k_{y}) of the photoelectron to the binding energy E_{B} in the solid as follows.

$$E_{\mathrm{kin}} = h\nu - \phi - |E_{\mathrm{B}}| \tag{2.3}$$

$$k_{\mathrm{x}} = \frac{1}{\hbar}\sqrt{2mE_{\mathrm{kin}}}\sin\theta\cos\varphi \tag{2.4}$$

$$k_{\mathrm{y}} = \frac{1}{\hbar}\sqrt{2mE_{\mathrm{kin}}}\sin\theta\sin\varphi \tag{2.5}$$

On the other hand, owing to the existence of the surface potential experienced by the escaping electron, the component of the momentum perpendicular to the sample surface $k_{\perp}$ (k_{z}) is not conserved. To evaluate the effect of the surface potential, we assume that the energy of the "real" finite state E_{f} (irrespective of the influence of the surface potential) has an energy offset of V_0 with respect to the kinetic energy E_{kin} measured by the analyzer as follows.

$$E_{\mathrm{f}} = E_{\mathrm{kin}} + V_0 \tag{2.6}$$

where V_0 is usually regarded as the inner potential.

Under the in-plane momentum conservation, we know that $\hbar k_{\parallel} = \sqrt{2mE_{\mathrm{kin}}}\sin\theta$. In addition, we know that $E_{\mathrm{f}} = \frac{(\hbar k_{\parallel})^2}{2m} + \frac{(\hbar k_{\perp})^2}{2m}$. From these equations, we obtain:

$$k_{\perp} = \frac{1}{\hbar}\sqrt{2m(E_{\mathrm{kin}}\cos^2\theta + V_0)} \tag{2.7}$$

The value of can be determined experimentally by measuring the periodicity of the energy dispersion along the out-of-plane momentum $k_\perp$ direction at the normal emission angle. However, for samples where the dispersion perpendicular to the sample surface is small, such a measurement would be difficult.

2.2. Quantum oscillations

In this subsection, we briefly review the formulas of quantum oscillations (QO) in the contexts of Dirac materials. The discussions are derived from Ref. [18,68]. Please consult the original papers for details.

Under an external magnetic field, the Landau level (LL) quantization of the energy states occurs in crystalline solids. As the field is tilted, the density of states at E_F undergoes quantum oscillations, leading to the variation of physical quantities as a function of $1/B$. In particular, the oscillations emerging in conductivity or resistivity are called Shubnikov-de Haas (SdH) oscillations, whereas the oscillations emerging in magnetic susceptibility are called de Haas-van Alphen (dHvA) oscillations.

The condition for LL formation is extracted from a generalized Lifshiftz-Onsager quantization expression

$$S_F \frac{\hbar}{eB} = 2\pi(n + \frac{1}{2} + \beta + \delta) \tag{2.8}$$

where S_F is the cross-sectional area of the Fermi surface normal to the field and n is the LL index that depends on $1/B$. δ is an additional phase shift stemming from three-dimensional curvature of the Fermi surface that is 0 for a 2D cylindrical FS and $\pm\frac{1}{8}$ and for a 3D FS [69,70].

The additional phase shift β equals 0 in conventional parabolic bands. However,

it was shown by Roth, 1966 that for arbitrary dispersions, β can take other values. Mikitik and Sharlai, 1999 demonstrated that the expressions of Roth, 1966 could be converted to a form in which β is shown to be equivalent to the Berry phase experienced by an electron as it goes around a closed loop in momentum space [19]. One of the fundamental features of Dirac fermions is this nontrivial Berry phase, which can be experimentally determined by QO measurements.

Such SdH oscillation experiments have been intensively studied in such 2D Dirac materials as graphene and topological insulator surface states and more recently in 3D materials, where it is generally harder to determine the Landau indices without a detailed analysis. First, in general, carrier density is so high that it is experimentally challenging to access low LL indices. Second, most of the candidate materials for Weyl and Dirac semimetals have complex band structures near the E_F, limiting the range of LL indices that can be clearly identified.

Despite these difficulties, SdH oscillations have been measured in various Weyl and Dirac semimetals, revealing evidence for nontrivial Berry phase shift. Representative data for SdH oscillations in a Dirac semimetal can be found in Fig. 2.2 for Cd_3As_2. The linear fit to the LL index plot intercepts the n axis at the values of 0.56 and 0.58, indicating evidence for a Berry phase offset of order π [71]. In a more recent study on the phase shift of SdH oscillations in 3D topological semimetals [72], it is suggested that the values of 0.56 and 0.58 should be modified to 0.06 and 0.08 by subtracting the extra 1/2, which results from assigning integer indices to the valleys in ΔR_{xx} instead of the peaks in ΔR_{xx}. To precisely extract the nontrivial Berry phase, it is suggested that the expression of the additional phase in the general form of the SdH oscillations should be summarized as follows.

$$\Delta R_{xx} \propto \cos[2\pi(F/B + \phi)] \tag{2.9}$$

where F is the oscillation frequency and ΔR_{xx} is the oscillatory component in the resistance R_{xx}. ϕ stands for the total additional shift, which can be directly obtained from the linear fit of the LL index plot using $n = F/B + \phi$ to the peaks in ΔR_{xx}. Using Eq. (1.104), it is demonstrated that the phase shift ϕ in Dirac or Weyl semimetals takes the values of either $\pm\frac{1}{8}$ or $\pm\frac{5}{8}$ [72].

Figures

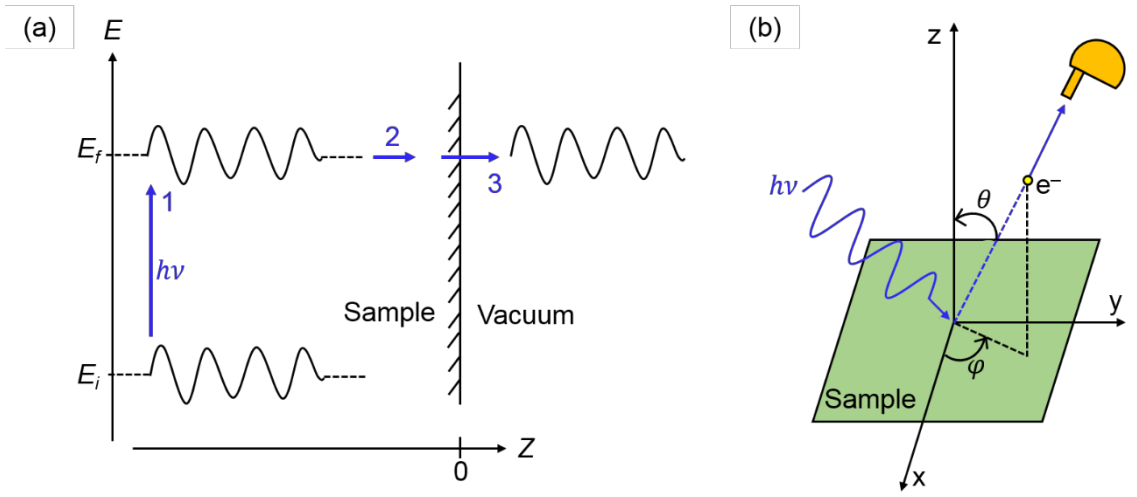

Figure 2.1: Schematic images of the photoemission process and ARPES experiments. a) Three-step model for the photoemission process inside the sample. 1. Excitation of an electron represented by a wave packet into the bulk final state. 2. Travel to the surface. 3. Escape into vacuum. (b) Geometry of an ARPES experiment. The momentum of the electron inside the sample can be obtained from the measured values of E_{kin}, θ, and φ.

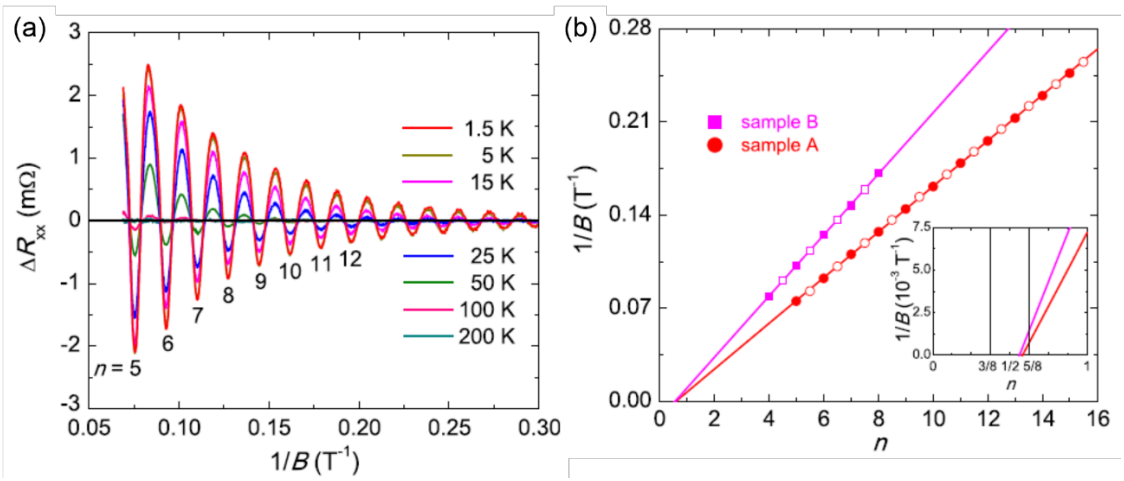

Figure 2.2: (a) Ocillatory component of the resistance R_{xx} of Cd_3As_2 as a function of $1/B$ after subtracting a smooth background. (b) LL index n vs. $1/B$. The solid and open circles represent the integer (R_{xx} valley) and half integer (R_{xx} peak) indices, respectively. Figures are adopted from Ref. [71].

Chapter 3 Flux Growth and Magneto-transport Properties of Ca_3PbO Single Crystals

3.1. Introduction

The synthesis of Dirac fermion systems and studies of their remarkable electronic properties, such as high charge carrier mobility, have recently become active areas of research [17,28,73,74]. The surface states and/or bulk states, which display linear energy dispersion in the surface or bulk, are expected to be stable against non-magnetic disorder and protected by time-reversal symmetry. In particular, the observation of quantum oscillations known as Shubnikov-de Haas (SdH) oscillations has played a pivotal role in detecting Dirac fermions in materials. Observation of these features allows a study of the Fermi surfaces and electron effective masses of the bulk and surface states [18].

To perform such magneto-transport experiments, the synthesis of single crystals with high purity and high homogeneity is needed. Chemical vapor transport (CVT) is a crystal growth technique widely used in the growth of single crystals of such Dirac materials as three-dimensional (3D) topological insulators, including Bi_2Se_3 [75], Bi_2Te_3 [76,77], and $(Pb_{1-x}Sn_x)Se$ [78,79]. This technique cannot be applied to oxide materials that do not easily sublime at low temperatures. Thus, antiperovskite oxide Ca_3PbO, a material recently predicted to be a 3D Dirac fermion system [59], requires alternative growth techniques. In recent crystallographic studies of antiperovskite oxides [80], it has been reported that single crystals of various antiperovskite compounds could be grown with the use of an alkaline earth as flux, which were one of the constituents of desired compounds. The maximum size of the Ca-related crystals obtained to date is ~140 μm,

which has limited the experimental feasibility of transport measurements. To reduce the experimental effort involved in transport measurements, it would be desirable to grow single crystals large enough for practical property measurements.

In addition to the size of the crystals, control of carrier density is another important factor in studies of Dirac materials, particularly for Bi_2Se_3, which is always electron doped owing to Se vacancies [81–83]. It is not possible to investigate the transport properties of a Dirac fermion system where the Fermi level is separated from the Dirac point. Antiperovskite oxides are no exception. In thermoelectric studies of Ca-related antiperovskite oxides, it has been reported that polycrystalline samples are heavily hole-doped [84]. Thus, for characterization of Dirac fermions, it is essential to suppress unintentional hole doping induced by the growth process.

Taking these factors into consideration, we optimized the growth parameters to obtain large single crystals of Ca_3PbO with a low carrier density. For the flux, we selected Ca rather than Pb, which is frequently used as a flux owing to its low melting point. The advantage of Ca flux over Pb flux can be understood from the Ca-Pb phase diagram [85], as shown in Fig. 3.1. Since Ca_3PbO is synthesized by reaction of CaO and Ca_2Pb which is the most Ca-rich compound in the Ca-Pb binary system [85], the formation of other Ca-Pb phases due to the decomposition of Ca_3PbO by Ca flux does not occur. On the other hand, such an unwanted phase can be formed in Pb flux because there exist several Pb-rich binary compounds: $2Ca_3PbO + Pb \rightarrow 2Ca_5Pb_3 + CaO$. Thus, we selected a Ca flux expecting to realize growth conditions where Ca_3PbO is a single phase accompanying the molten Ca flux during its single growth process. In this paper, we report that single crystals, ~1 mm in size with a carrier density of 4.0×10^{19} cm^{-3}, could be successfully obtained from molten Ca flux methods. The crucible material and sealing

method were found to be critical factors for achieving large crystals with low carrier density. To demonstrate the high purity and homogeneity of our crystals, we measured SdH oscillations on a crystal grown under the optimum synthesis conditions.

3.2. Experimental

3.2.1. Synthesis

Ca_3PbO crystals are reported to be sensitive to air and moisture [80,86,87], so all procedures were performed in an Ar-filled glove box. First, we prepared polycrystalline samples as seed materials for the synthesis of Ca_3PbO single crystals. Starting materials were Ca_2Pb and CaO. Ca_2Pb was prepared by reaction of Ca and Pb metals in a molar ratio of 2.2:1. A mixture of Ca (Sigma-Aldrich, 99.99%) and Pb (Sigma-Aldrich, 99.99%) was placed in an iron crucible (Fe 99.5%), sealed in a stainless steel capsule (18% Cr-8% Ni), heated to 850°C at a rate of 50°C/h, and held at that temperature for 12 h. Excess Ca was added to compensate for the evaporation loss of Ca that could yield the formation of other binary compounds such as Ca_5Pb_3. CaO was prepared by heating $CaCO_3$ (Sigma-Aldrich, 99.99%) at 1200°C for 1 h in an ambient atmosphere and subsequently allowed to cool in a vacuum. Next, the resulting Ca_2Pb and CaO powders were weighed in the stoichiometric antiperovskite ratio, thoroughly mixed in a silica glass mortar, and pressed into pellets. The pellets were sealed in a stainless steel capsule and heated at 950°C for 24 h. To promote homogeneity, the resulting sintered samples were ground again, pressed into pellets, and heated at 950°C for 12 h. Ref. [86] reported that the starting materials of Ca and PbO with a 10% excess of Ca were heated at 850°C for 6 h. We also grew polycrystalline samples by following this process but found it difficult to maintain a stoichiometric composition. To minimize the deviation from the stoichiometric

composition, we instead started from binary compounds, which allowed us to efficiently prepare a relatively large amount of homogeneous seed materials (~2.3 g), necessary for the growth of single crystals larger than 500 μm. To investigate the thermal stability and determine the temperature conditions for the flux growth of Ca_3PbO single crystals, polycrystalline samples were heated at various temperatures between 850 and 1200°C for 6 h.

Next, the synthesized materials were combined with Ca metal as a flux in a molar ratio of 1:10 in various types of crucibles (stainless steel, Mo, and Fe crucibles). The different types of crucibles were then sealed in a stainless steel capsule to determine the material that is least likely to react with the Ca flux and alter the amount of Ca flux during the growth process. In addition to the crucible material, the stainless steel capsule was set up in two ways: one with a large empty space inside the capsule and the other with two short stainless steel rods placed at the top and bottom of the crucible to fill the inner space, as depicted in Figs. 3.4(e) and (f), respectively. The capsules were heated up to 1000°C at a rate of 66.6°C/h and held at that temperature for 6 h. Subsequently, the temperature was slowly decreased at a rate of 0.5°C/h to 800°C, and maintained at that temperature for 20 h. To grow larger crystals, we added a slow cooling step to the growth process. Finally, the crucible was removed from the capsule and the residual Ca flux was removed by evaporation at 800°C under vacuum.

3.2.2. Characterization

Polycrystalline samples were ground and sealed in a plastic capsule filled with Ar gas and characterized by powder X-ray diffraction (PXRD), using a Bruker D8 Advance diffractometer with Cu Kα radiation source (Bruker, Corp., USA) at room temperature.

The diffraction patterns were recorded in the 2θ angular range of 15°–90°. Peak indexing was carried out by Rietveld refinement performed with the TOPAS package [88]. Single-crystal X-ray diffraction (SXRD) was performed on a 0.1 mm × 0.1 mm × 0.1 mm crystal using a Rigaku R-AXIS RAPID II diffractometer with Mo Kα radiation source (Rigaku, Corp., Japan) at room temperature. The crystals were mounted on a glass capillary. To avoid exposure to air, they were immersed in liquid paraffin before being transferred to the SXRD apparatus. Unit cell refinement was performed with the CrystalClear software (version 1.3.6 SP3 Rigaku Corporation, Tokyo, Japan, 2007.). The rocking curve of 001 diffraction was measured using a SmartLab diffractometer system with Cu Kα radiation source (Rigaku, Cop., Japan) at room temperature. Full widths at half maximum (FWHMs) of the rocking curves were employed as the measure of crystallinity of the samples. The chemical composition was determined by electron-probe microanalysis (EPMA) using a field emission electron microprobe JEOL JXA-8530F (JEOL, Ltd., Japan). The analysis of the oxygen content is highly sensitive to the tilting of the sample surface, while those of Ca and Pb are considerably less sensitive to the tilting; thus, the atomic ratios of Ca to Pb were used to evaluate the chemical composition.

3.2.3. Transport measurements

Resistivity ρ_{xx} and Hall resistivity ρ_{xy} were measured by the four-probe method using a Physical Property Measurement System (PPMS) (Quantum Design, Inc., USA) where magnetic fields ($\mu_0 H$) up to 9 T were applied normal to the (001) sample surface. The geometry of electrodes is illustrated in Fig. 3.4(d). Crystals were fixed on sapphire substrates by applying Stycast 2850 epoxy and heated at 80°C to cure the epoxy. The sample surfaces were then gradually scrapped with sandpaper to a thickness less than 0.1

mm, contacted by silver epoxy, and heated in the glove box at 150°C to dry the epoxy. To prevent the sample from reacting with ambient atmosphere during the measurements, the samples were covered with Paratone-N oil before being transferred to the measurement chamber of the PPMS. The electric current I = 5 mA flowed along the a axis on the ab plane. The Hall resistivity along the b axis was extracted from the difference of the transverse resistance measured at positive and negative fields such that $\rho_{xy}(\boldsymbol{B}) = [\rho(\boldsymbol{B}) + \rho(-\boldsymbol{B})]/2$, where $\boldsymbol{B}$ represents the magnetic flux density. Using this method, we removed the longitudinal resistivity component stemming from voltage probe misalignment. The magnetization of the sample is neglected in the following sections ($B = \mu_0 H$).

3.3. Results and discussion

3.3.1. Characterization

Figure 3.2(a) shows the PXRD patterns of polycrystalline samples measured after the first and second heat treatments at 950 °C, which fitted well to the crystal structure reported in the literature [80,86]. The XRD patterns demonstrated that the sample was already a single-phase of Ca_3PbO after the first treatment and remained unchanged after the second heat treatment. Figures 3.2(b) and (c) show the PXRD patterns of polycrystalline samples heated at temperatures between 850 and 1200°C. In particular, the change in the thermal stability of Ca_3PbO could be clearly observed in the peak at ~ 32° corresponding to the (111) reflection, the strongest one in the XRD patterns, which remained unchanged up to 1050°C and began to deviate at 1150°C. The deviation of the (111) reflection at 1150°C could be quantitatively explained by the increase in the lattice parameters, which we estimated to deviate by 2% from that of the samples heated at

850°C. The change in the lattice parameters could be understood by taking into account the formation of Ca deficiencies. More of these defects formed as temperature was increased, subsequently inducing the precipitation of Ca-deficient compounds as impurities, and eventually leading to decomposition of Ca_3PbO into Pb and CaO. These observations indicated that Ca_3PbO cannot remain thermally stable at temperatures higher than 1050°C. Hence, we determined the initial temperature for the growth of single crystals to be 1000°C.

Figures 3.3(a)-(d) show microscope images of the samples grown in stainless steel, Mo, and Fe crucibles. Square-like facets were observed in all samples, whereas the size of the crystals reached up to ~1 mm in samples grown in the Fe crucibles, making it easier to prepare samples for transport measurements. Figures 3.3(e) and (f) show backscattered electron (BSE) images of the crystals grown in a Fe crucible with filled space. The major part of the square-like facet represented by gray color corresponds to the Ca_3PbO phase. Black spots, pointed by red and pink arrows, are confirmed to be CaO and Fe particles, respectively. Light gray spots, pointed by orange arrows, show the Pb-rich regions of the Ca_3PbO phase. To suppress the effect of compositional deviation, the crystal surface was mechanically polished with sandpaper before performing the Hall effect and SdH oscillation measurements. The BSE images in Figs. 3.3(e) and (f) show the composition of the crystals before and after the mechanical treatment with sandpaper, depicting that Fe particles and Pb-rich regions of the Ca_3PbO phase were reduced after the treatment. The chemical composition of the samples grown in various crucibles are summarized in Table 1. The atomic ratios of Ca to Pb, regardless of the crucible material, show a Ca deficiency proportion of 2-3%.

Figures 3.3(g)-(i) show the XRD patterns of a crystal grown in an Fe crucible with

filled space. The θ-2θ scan in Fig. 3.3(g) solely consists of the peaks corresponding to the (00l) reflections, confirming that the square facets correspond to the (00l) planes and that the sample was single phase. Figure 3.3(h) represents the XRC for the 001 diffraction (Δω). The FWHM is 0.06°, indicating the high quality of the grown single crystals. The 2θ-fixed ϕ-scan of the (111) diffraction in Fig. 3.3(i) revealed a fourfold in-plane symmetry, indicating that the samples were single domain.

3.3.2. Transport properties

To successfully observe the SdH oscillations in Ca_3PbO, control of the carrier density *N* is crucial in that the oscillation frequency depends on *N* and determines the magnitude of the magnetic field needed to clearly detect the oscillations. A lower value of *N* requires a field of lower magnitude. In addition, mobility is the second crucible parameter because it affects the amplitude of the oscillations. Figures 3.4(a) and (b) show the temperature dependence of the resistivity ρ_{xx}, carrier density *N*, and transport mobility μ_{tr} and the field dependence of the Hall resistivity ρ_{xy} for samples grown in various crucibles, respectively. The ρ_{xx}–*T* curve for the sample grown in the stainless steel crucible (18% Cr-8% Ni) shows a semiconductor-like upturn at low temperatures, while *N* is comparatively high. This behavior can be attributed to magnetic impurities such as Ni and Cr included in the crucible, suggesting that the samples reacted with these magnetic elements during the crystal growth.

Except for the crystals grown in stainless steel crucibles, the transport measurements revealed metallic conduction with *p*-type carriers in each sample, which could stem from Ca deficiencies detected in all the samples, as summarized in Table I where the atomic ratios of Ca to Pb (Ca/Pb) for crystals grown in various crucibles are

listed together with the residual resistivity ratio (RRR), N (2 K), N (2 K) per Ca atom in unit cell, and μ_{tr} (2 K). Table I shows that all the samples potentially contain Ca deficiencies of ~ 3% at maximum. However, the deviation from the stoichiometric composition is comparable to the standard deviation so that it is difficult to distinguish Ca deficiencies of each sample. In contrast, the numbers of carriers per Ca atom in unit cell, which can be estimated from hole densities, considerably vary from 0.1 % to 7 %. These comparisons demonstrate that the relationship between Ca deficiencies and hole densities cannot be clearly explained in the present study.

Despite the problem with the origins of high hole densities, the comparison of transport properties in Table I reveals that the highest RRR of 2.675(7), the lowest N of 4.011(2) × 10^{19} cm^{-3}, and the highest μ_{tr} of 3893(2) cm^2 V^{-1} s^{-1} are obtained in the samples grown in Fe crucibles with filled space, indicating that the Fe crucibles with filled space are best-suited to the synthesis of Ca_3PbO single crystals with a Ca flux. Also, these comparisons indicate that confinement of Ca flux in the crucible during the growth process is effective in reducing N and increasing μ. Consequently, magnetoresistance (MR) was largest for the samples grown in Fe crucibles with filled space, as shown in Fig. 3(c). Due to the linear dispersion around valence band maximum, the effective mass m^* of hole in Ca_3PbO drastically decreases with the reduction of residual hole density N. In addition, EPMA results show that hole carriers stem from Ca vacancies; thus, the difference in MR ratio, which depends on m^*, results from a slight variation in Ca deficiencies. Since the tight fitting crucible lid is effective for the suppression of N, the different MR ratio is likely to be caused by degree of Ca melt leakage. If the crucible material has high wettability for Ca melt, the melt can easily spill out along the crucible wall. Therefore, Fe is considered to be less wettable than other crucible materials.

3.3.3. Shubnikov-de Haas oscillations and band parameters

Through the use of Ca_3PbO single crystals grown in Fe crucibles with filled space, we succeeded in detecting SdH oscillations in the Hall resistance R_{xy}. In contrast, the oscillations in MR were hardly discernible. In general, the amplitude of oscillations of the longitudinal resistance R_{xx} is greater than that of R_{xy}. However, as shown in the geometry of electrodes [Fig. 3.4(d)], the distance between the electrodes for Hall voltage is approximately two times as long as that for longitudinal voltage, leading to a factor of R_{xy} (9 T)/R_{xx} (9 T) = 14.1 mΩ / 5.8 mΩ ~ 2.4 at 2 K. Due to the difference in the magnitude of voltage, the SdH oscillations were only detected in R_{xy}. Figure 3.5(a) shows the field dependence of the Hall resistance R_{xy} and its derivative dR_{xy}/dB at 2 K. These results show that the oscillations were amplified as the field increased. By subtracting a polynomial background of R_{xy} at temperatures between 2 and 40 K, the SdH oscillations periodic in 1/B are observed [Fig. 3.5(b)]. The fast Fourier transform (FFT) spectrum of the SdH oscillations at 2 K, as illustrated in Fig. 3.5(c), shows a single oscillation frequency F = 65 T, which corresponds with a periodicity $\Delta(1/B) = 0.015\ T^{-1}$. We used the Onsager relation, $F = (\hbar/2\pi e)S_F$, where $\hbar$ is Planck's constant and S_F is a cross-sectional area of the Fermi surface normal to the field, to obtain $S_F = 6.2 \times 10^{-3}$ Å^{-2} which amounts to only 0.3% of the cross-sectional area of the first Brillouin zone (BZ). By assuming a circular cross section, we extracted a very small Fermi wave vector of $k_F = 0.044$ Å^{-1}. The DFT calculation in Ref. [59] predicts that there exist three pairs of hole pockets with uniaxial anisotropic shapes on Γ-X path in the bulk Brillouin zone of hole-doped Ca_3PbO. Despite this theoretical prediction, experimental studies on the Fermi surface of Ca_3PbO have been lacking. To study the anisotropic Fermi surface, it is essential to observe the SdH

oscillations in a wide range of the magnetic field. Our results demonstrate that it is feasible to detect the SdH oscillations in DC fields, thereby suggesting the studies on the Fermi surface of Ca_3PbO using high-field measurements.

We further analyzed the SdH oscillation amplitude to derive the band parameters of Ca_3PbO. Using the standard Lifshitz–Kosevich (LK) formula [70], the temperature-dependent amplitude ΔR_{xy} is expressed as $\Delta R_{xy}(T)/\Delta R_{xy}(0) = \lambda(T)/\sinh(\lambda(T))$, and the thermal factor is described by $\lambda = 2\pi^2 k_B T m^*/(\hbar e B)$, where k_B and m^* represent the Boltzmann constant and the effective cyclotron mass, respectively. Figure 3.5(d) shows the temperature dependence of the relative oscillatory component $\Delta R_{xy}(T)/\Delta R_{xy}(2\ \mathrm{K})$ for the peak at $1/B = 0.120\ \mathrm{T}^{-1}$. The fit yields $m^* = 0.064\ m_0$ with m_0 the bare electron mass. The Fermi velocity $v_F = \hbar k_F/m^*$ was calculated to be $v_F = 8.07 \times 10^5$ m/s. The Dingle temperature $T_D = 41$ K can be derived from a Dingle plot, as shown in Fig. 3.5(e). Accordingly, a long mean free path of $l_q = 24$ nm was estimated. The values of these band parameters are comparable to those of well-studied 3D Dirac fermion systems such as Cd_3As_2 [71,89]. Conversely, there was a clear difference in the ratio of quantum mobility to transport mobility. The quantum mobility μ_q of Ca_3PbO calculated by $\mu_q = e\tau_q/m^*$ was 823 $\mathrm{cm^2\ V^{-1}\ s^{-1}}$, which is 21% of the transport mobility μ_{tr} of 3860 $\mathrm{cm^2\ V^{-1}\ s^{-1}}$. This ratio was three orders of magnitude smaller than that in Cd_3As_2 [90] although the carrier density of the Cd_3As_2 crystal exhibiting the highest μ_{tr} is 7.4×10^{18} $\mathrm{cm^{-3}}$ [90], this was only an order of magnitude smaller than that of the Ca_3PbO crystals. The discrepancy in the ratio of μ_q to μ_{tr} mainly stems from the considerable difference of μ_{tr} between these two materials. The μ_{tr} of Cd_3As_2 can reach 9×10^6 $\mathrm{cm^2\ V^{-1}\ s^{-1}}$ [90], which is three orders of magnitude higher than that of Ca_3PbO. The difference of μ_{tr} could be attributed to the energy difference between the upper and lower Dirac cones of Ca_3PbO, which is

approximately three times as large as that of Cd_3As_2, suggesting that the separation between the Fermi level and the Dirac point in Cd_3As_2 would be much smaller than that in Ca_3PbO. To obtain higher mobility in Ca_3PbO, it is thus necessary to further decrease the carrier density.

3.3.4. Conclusions

We investigated the optimum conditions for the synthesis of Ca_3PbO single crystals by a Ca flux method to increase the size of crystals and reduce hole carrier density. The crucible material and sealing method were critical factors for confining Ca melt during growth process. Using crystals grown in Fe crucibles sealed in stainless steel capsules where empty space was completely filled, we succeeded in growing single crystals, 1 mm in size, with a carrier density of 4.0×10^{19} cm^{-3}. SdH oscillations were clearly observed in a crystal grown under the optimum synthesis conditions. Various band parameters of Ca_3PbO were measured and found to be consistent with those expected for Dirac fermion systems.

Figures

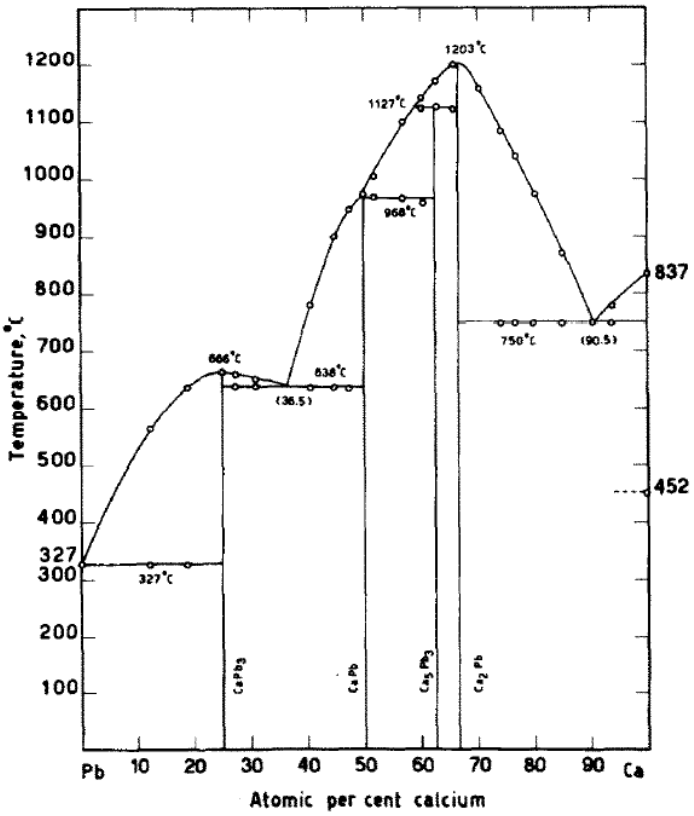

Figure 3.1: The calcium-lead phase diagram adopted from Ref. [85].

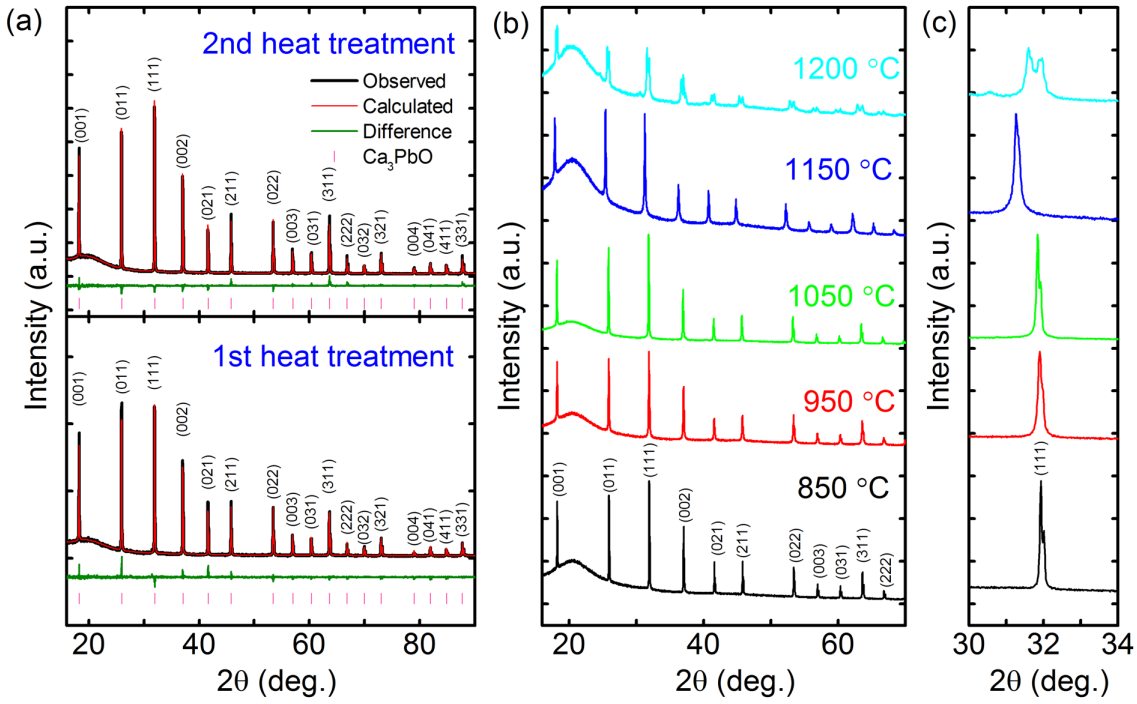

Figure 3.2: (a) Powder X-ray diffraction (PXRD) patterns and Rietveld refinements of polycrystalline samples measured after the first and second heat treatments with the Miller indices shown in parenthesis for respective crystal planes. Plot shows the observed (black line) and calculated (red line) PXRD patterns with a difference curve (green line). Vertical tick marks represent Bragg reflections in the $Pm\bar{3}m$ space group. The broad peak observed at ~20° stems from diffraction of the plastic capsule. (b),(c) Comparison of PXRD patterns of polycrystalline samples heated at various temperatures. The (111) peak at each temperature is shown in (c).

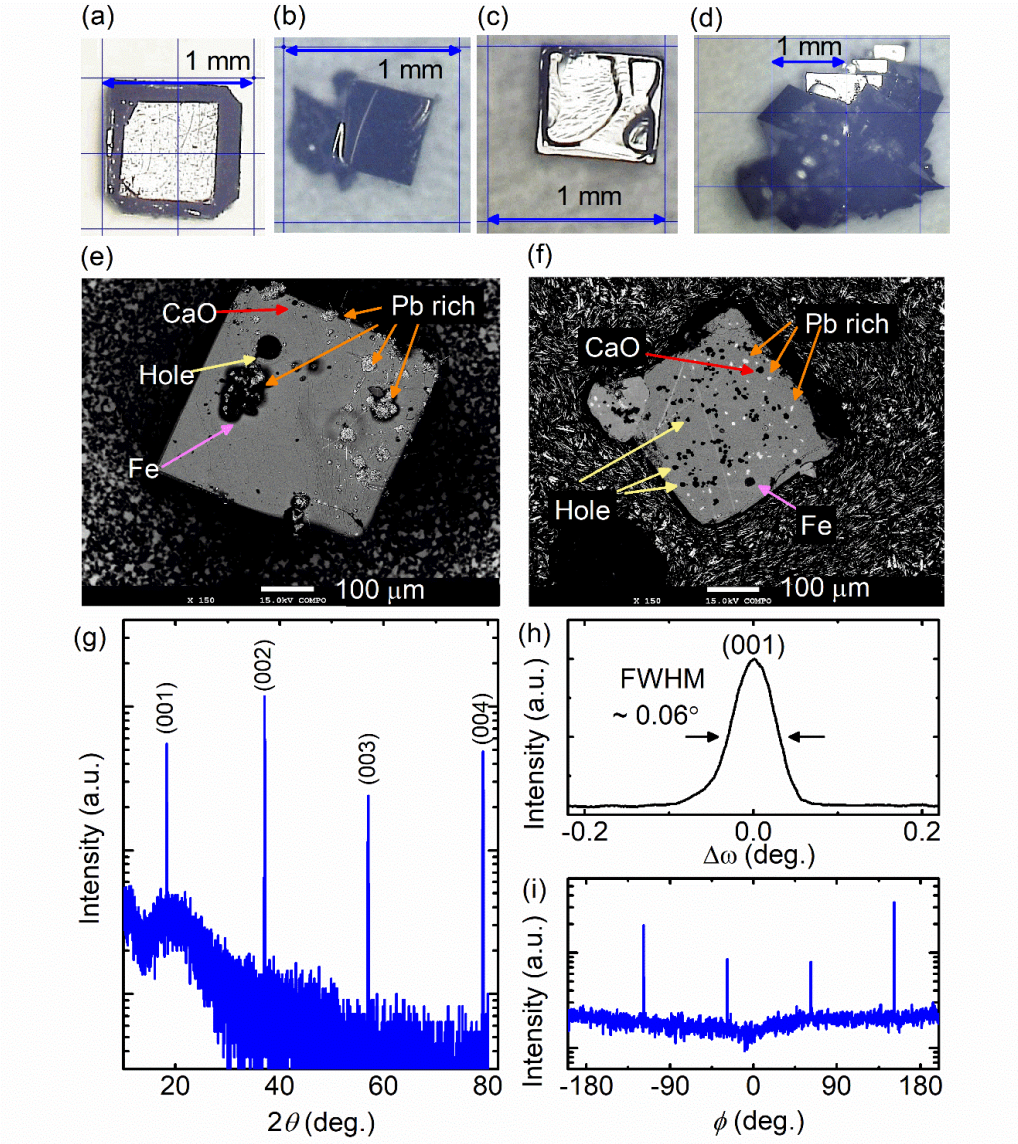

Figure 3.3: Characterization of the samples grown in different crucibles. (a)-(d) Microscope images of crystals grown in stainless steel (a), Mo (b), and Fe crucibles (c, d), respectively. (e),(f) Compositional images of the crystals grown in an Fe crucible with filled space before and after the mechanical treatment with sandpaper, obtained by EPMA. Black spots (pointed by red arrows) indicate CaO particles, whereas white spots (pointed by orange arrows) represent surface Pb-rich regions of the Ca_3PbO phase. Black spots pointed by pink and yellow arrows show Fe particles and holes, respectively. (g-i) X-ray diffraction (XRD) patterns of a crystal grown in an Fe crucible with filled space. (g) XRD pattern of θ-2θ scan. The observed peaks correspond to the (00l) reflections of Ca_3PbO, which confirm that the grown crystal was single phase. (h) Normalized rocking curve for the (001) reflection. (i) XRD pattern of ϕ scan for the (111) reflection.

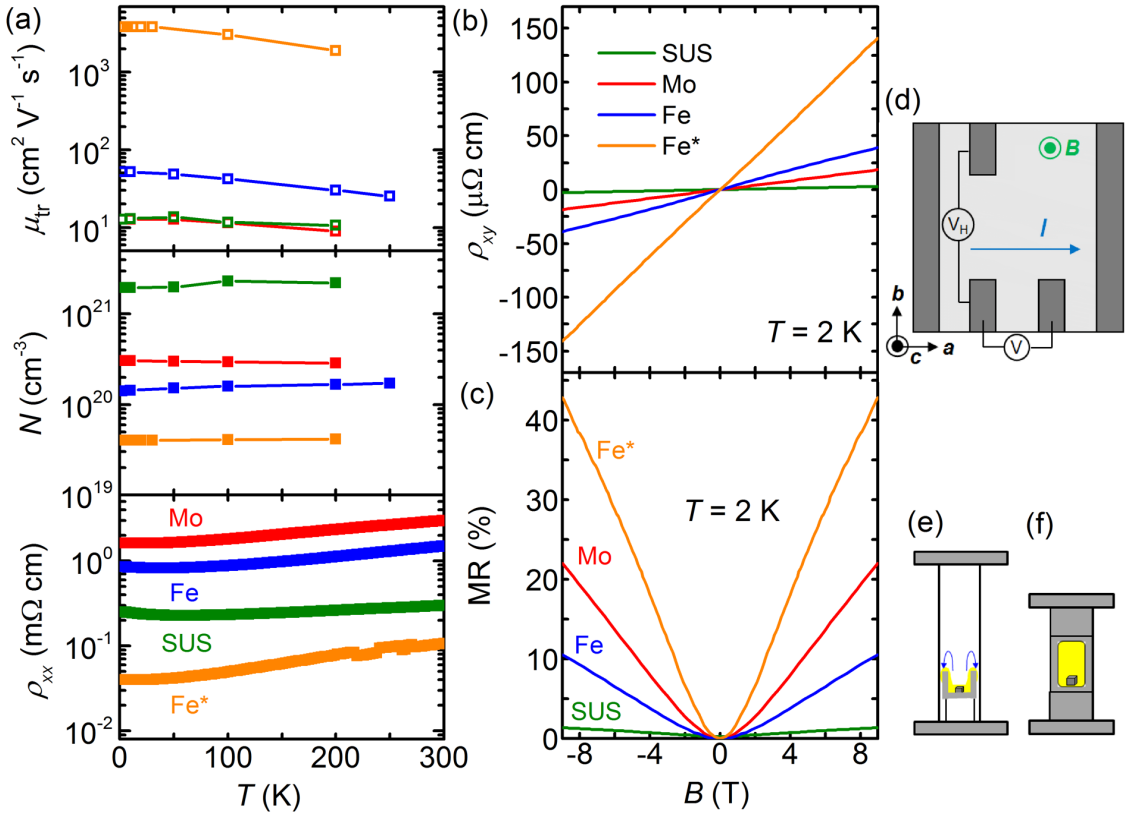

Figure 3.4: Transport properties of crystals grown in stainless steel, Mo, and Fe crucibles. In particular, the data of the crystals grown in Fe crucibles with and without empty space in the stainless steel capsules are illustrated by blue and orange symbols, respectively. (a) Temperature dependence of resistivity ρ_{xx}, carrier density N, and transport mobility μ_{tr}. (b),(c) Field dependence of Hall resistivity ρ_{xy} and magnetoresistance (MR) at 2 K. (d) Schematic of the four-probe configuration for the transport measurements in which the current flows along the *a* axis on the *ab* plane with the magnetic field applied along the *c* axis. (e),(f) Schematic images of stainless steel capsules with and without empty space, respectively. Yellow parts and gray cubes represent Ca melt and Ca_3PbO crystals formed during the growth process.

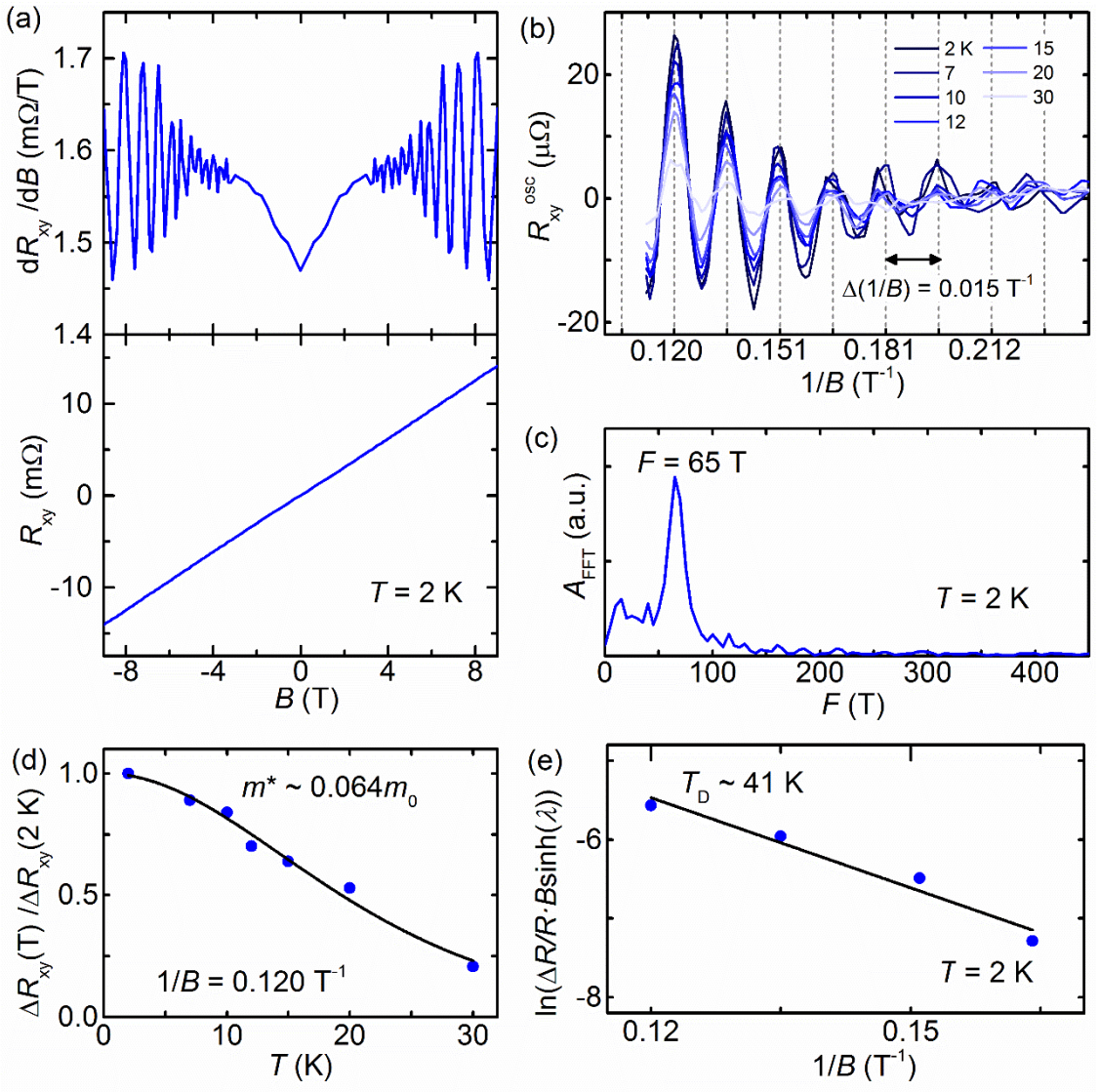

Figure 3.5: SdH oscillations in crystals grown in Fe crucibles with filled space. (a) Hall resistance R_{xy} and the derivative of the R_{xy} with respect to B at 2 K. (b) Oscillatory component of R_{xy} vs. $1/B$ scaled by the periodicity $\Delta(1/B) = 0.015$ T^{-1} at various temperatures. (c) FFT spectrum of the SdH oscillations at 2 K. (d) Temperature dependence of the oscillation amplitudes $\Delta R_{xy}(T)/\Delta R_{xy}$ (2 K) for the peak at $1/B = 0.120$ T^{-1}. (e) Dingle plot at 2 K for the SdH oscillations with the oscillation frequency $F = 65$ T.

Crucible	Ca:Pb	RRR	N (10^{19} cm^{-3})	μ_{tr} (cm^2 $V^{-1}s^{-1}$)
SUS	2.94(9):1	1.198(4)	196.2(2)	12.67(1)
Mo	2.7(5):1	1.845(2)	30.47(3)	12.61(1)
Fe	2.92(3):1	1.768(2)	14.11(3)	51.9(1)
Fe*	2.9(1):1	2.675(7)	4.011(2)	3893(2)

Table 1: Parameters of the samples grown in different crucibles. Fe and Fe* crucibles represent those with and without empty space in the stainless steel capsules. Ca:Pb is the atomic ratio of Ca to Pb determined by EPMA. RRR is the ratio ρ_{xx}(300 K)/ρ_{xx}(5 K). N and μ_{tr} are carrier density and transport mobility at 2 K, respectively.

Chapter 4 ARPES Studies of Ca_3PbO

4.1. Introduction

Three-dimensional (3D) Dirac fermion systems have emerged as one of the most prominent topics in condensed matter physics. They comprise a class of topological materials in which bulk conduction and valence bands with linear energy-momentum dispersion relations meet at finite points or along curves in *k* space. These phenomena have been theoretically predicted and experimentally verified to occur at the phase transition point between a trivial insulator and a topological insulator [27,91–93], or in topological semimetals including those of the 3D Weyl [42,94–110], 3D Dirac [54–57,111–113], and topological nodal line semimetal (TNLS) [94,114–128] types.

Recently, there has been a growing interest in the cubic antiperovskite family as potential source of such novel topological phases of matter as 3D Z_2 invariant topological insulators [58], 3D massive Dirac fermions [59,84,130], topological crystalline insulators [62,63], TNLSs [118,119], and topological superconductors [64]. In particular, recent theoretical calculations on Ca_3PbO [59] (Fig. 1(a)), made of Ca^{2+}, Pb^{4-} and O^{2-} ions, predict the presence of a 3D gapped Dirac-like cone at finite momentum along the Γ-X direction, which results from a band inversion of the Ca 3*d* and Pb 6*p* bands at the Γ point. Of paramount interest is the possibility that Ca_3PbO hosts 3D Dirac fermions with cubic symmetry as an intrinsic part of its electronic structure, since 3D Dirac fermions in other materials are sometimes only realized under such extreme conditions as low temperature or high pressure [131–133]. Like normal cubic perovskite materials, notably $SrVO_3$ [134], Ca_3PbO exhibits easy cleavage along (001) planes, which preserve

a C_4 symmetry element in the bulk structure, a prerequisite for the protection of its bulk massive Dirac states and surface massless Dirac states. It is thus feasible to conduct experiments with a magnetic field applied along the C_4 rotation axis, as proposed previously [30]. Furthermore, the states near the Fermi level (E_F) are predicted to be derived entirely from Dirac-like bands with linear dispersion allowing for fundamental and direct studies of 3D Dirac fermions [59].

In order to verify the presence of 3D Dirac fermions experimentally, it is necessary to identify a Dirac point in 3D momentum space and investigate the electronic structure associated with the particular point not only along the surface-parallel directions (k_x or k_y) but also along the surface-perpendicular direction (k_z). These requirements call for an experimental probe with a good definition of k_z. Soft x-ray angle-resolved photoemission spectroscopy (SX-ARPES) is the most powerful method for directly studying the 3D electronic band structures of bulk materials, and has been demonstrated to provide a high-k_z resolution [135]. Thus, SX-ARPES using the tunable excitation energy of synchrotron radiation is eminently suited for the navigation of the 3D electronic structure of Ca_3PbO. In this paper we employ SX-ARPES to experimentally observe the Dirac-like band dispersion along the Γ–X direction in the 3D Brillouin zone (BZ) of bulk Ca_3PbO. By comparing these results with those for Bi-doped Ca_3PbO, we also show that electron doping leads to the shifts of the band structure downward, thereby demonstrating that aliovalent doping is effective in tuning the E_F of Ca_3PbO without fundamentally changing its Dirac-like band structure.

4.2. Experimental

4.2.1. Synthesis

The details on the synthesis of Ca_3PbO single crystals are provided in the chapter 3. The single crystals used in ARPES experiments were grown in an iron crucible sealed in a stainless steel capsule where its inside space remained empty. In fact, the ARPES experiments were performed before the optimum synthesis conditions were obtained. The results of ARPES experiments motivated us to further improve the synthesis conditions to reduce the hole carrier density. For APRES experiments, we used the crystals with black color and square-like facets [Fig. 4.1(b)]

The size of the grown crystals reaches ~ 1 mm, which is large enough to obtain well-cleaved sample surfaces for ARPES measurements. We also grew the electron-doped samples with a chemical formula $Ca_3(Pb_{1-x}Bi_x)O$ (x = 0.07). Synthesis of the Bi-doped single crystals followed the same procedure as that for the non-doped crystals, except that Ca_5Bi_3 was added as a Bi source to the Ca_2Pb and CaO starting materials, with the molar ratios being of the form $Ca_2Pb:Ca_5Bi_3:CaO = 1-x : 2x/5 : 1$.

4.2.2. Characterization

Ca_3PbO crystallizes in a cubic inverse perovskite type structure [Fig. 4.1(a)] with a = 0.484 nm and space group $Pm\bar{3}m$ [86]. The O atoms are located at the centers of the unit cell, surrounded by corner-sharing, regular Ca_6 octahedra. Single-crystal X-ray diffraction (SXRD) was performed on a 0.1 mm × 0.1 mm × 0.1 mm crystal using a R-AXIS RAPID II diffractometer and Mo K-alpha radiation, at room temperature. The crystals were mounted on a glass capillary. Afterwards, to avoid exposure to air, they were immersed in liquid paraffin before transferring them from an Ar-filled glove box to the

SXRD apparatus. Unit cell refinement was performed with the CrystalClear software (version 1.3.6 SP3 Rigaku Corporation, Tokyo, Japan, 2007.). The samples were confirmed to have a cubic crystal structure with lattice parameter a = 0.485(2) nm, matching that of polycrystalline Ca_3PbO.

The compositional formula of the non-doped single crystal used in the ARPES measurements was determined to be $Ca_{2.94(4)}Pb_{1.00(1)}O_{1.00(4)}$ by electron-probe microanalysis (EPMA) using a field emission electron microprobe JEOL JXA-8530F, indicating that the crystals contain vacancies on 2% of the Ca sites. As for the Bi-doped samples, EPMA confirmed that the Bi content is almost comparable to the nominal value ~ 0.07 and that the samples are also slightly Ca-deficient.

4.2.3. Transport measurements

Resistivity, Hall resistivity, and specific heat measurements were performed in the temperature range of 1.8–300 K and the magnetic field (B) range of –9 to 9 T using a Physical Property Measurement System (Quantum Design). Cu wire contacts in the four-probe configuration were mounted to the sample with silver epoxy inside the Ar-filled glove box. The samples were heated in the glove box to 150°C to cure the epoxy. Samples were immersed in Paratone-N oil to prevent them from reacting with ambient air during the measurement. The electric current flowed in the ab plane while the applied B was parallel to the c axis. Fig. 4.2 shows the field dependence of Hall resistivity at various temperatures. It is confirmed that both non-doped and Bi-doped samples were p-type at all temperature ranges. Fig. 4.3 shows specific heat divided by the temperature of the Ca_3PbO single crystals, $C(T)/T$, as a function of T^2 in the low temperature region between 1.8 K and 3.7 K. The data was fitted to the expression $C(T)/T = \gamma + \beta T^2$. The derived

Sommerfeld coefficient (γ) is 1.16(2) mJ mol^{-1} K^{-2}. The theoretical γ calculated from the free-electron model is 2.29 mJ mol^{-1} K^{-2}. The ratio of the measured γ to the calculated γ yields the thermal effective mass, m_{th}, of ~ 0.51 m_0.

4.2.4. Ultraviolet photoemission spectroscopy (UPS)

UPS measurements were performed with Scienta Omicron DA30 electron analyzer under the base pressure lower than 2×10^{-8} Pa at room temperature. UV light was generated using a monochromatized microwave-driven He discharge lamp (MBS L-1). To excite photoelectrons, we used the He IIα resonance line ($h\nu = 40.8$ eV). Samples were cleaved *in situ* along the (001) surface at the measurement temperature. Fig. 4.4 shows the secondary electron emission measured at an applied voltage of 7 V. The work function ϕ of Ca_3PbO was determined to be 3.5 eV ± 0.1 eV. By using the value of $\phi \sim$ 3.5 eV determined by UPS, the inner potential V_0 was estimated to be ~ 8.5 eV.

4.2.5. Soft X-ray angle-resolved photoemission spectroscopy

In order to experimentally identify the 3D massive Dirac fermions, we performed bulk-sensitive SX-ARPES measurements at the beamline BL–2A MUSASHI at the Photon Factory, KEK. The tunable excitation energy of the synchrotron radiation source enabled us to trace the electronic structures in all three dimensions of momentum space. Samples were cleaved *in situ* at the measurement temperature of ~ 20 K under an ultrahigh vacuum of 1×10^{-10} Torr, and the experimental data were collected using a Scienta SES-2002 electron energy analyzer with light linearly polarized along the horizontal direction. The energy and angular resolutions were set to approximately 170 meV and 0.3°, respectively.

4.2.6. DFT calculations

To provide a theoretical reference with which to compare our ARPES results, we performed DFT band structure calculations with the Perdew-Burke-Ernzerhof (PBE) generalized-gradient approximation [136] using the VASP code [137], while the effective mass and hole carrier concentration were calculated using SKEAF code [138]. In agreement with the pioneering theoretical work on this compound [59], a Dirac electron is found to be located along the Γ–X direction in the BZ [Figs. 4.5(a) and (b)].

4.3. Results and discussion

4.3.1. Transport properties

Fig. 4.1(c) shows the temperature dependence of the mobility, carrier density, and resistivity of the non-doped and the Bi-substituted Ca_3PbO samples. These measurements reveal metallic conduction with *p*-type carriers [Figs. 4.1(c) and 4.2]. Upon partially substituting Pb with Bi, the carrier density N slightly decreased from 1.4×10^{20} cm^{-3} to 6.9×10^{19} cm^{-3} at $T = 2$ K, but the Hall mobility μ significantly increased from 50 cm^2 V^{-1} s^{-1} to 370 cm^2 V^{-1} s^{-1} at this temperature [Fig. 4.1(c)]. The high hole carrier concentration is consistent with the EPMA result indicating that both the non-doped and the Bi-substituted samples contain a Ca deficiency of 2% which is likely to generate holes: $\mathrm{Ca}_{\mathrm{Ca}}^{\times} \rightarrow \mathrm{V}_{\mathrm{Ca}}'' + 2h^{\bullet} + \mathrm{Ca(g)}$.

Fig. 4.1(d) shows the magnetic-field (B) dependence of the magnetoresistance (MR) ratio for both non-doped and Bi-doped Ca_3PbO at $T = 2$ K, where the MR ratio (%) is defined as $[\rho(B) - \rho(0\ \mathrm{T})]/\rho(0\ \mathrm{T}) \times 100$. The linear dependence of the MR ratio on the magnetic flux density B, one of the distinguishing magnetotransport properties of Dirac

fermions [64], is clearly observed when the first-order derivative dMR/dB curve is investigated, as illustrated in Fig. 4.1(e). dMR/dB is semiclassically proportional to B^2 at low B, but it soon saturates at a critical field $|B|$ of ~ 1.6 T, which is defined as the point of intersection between the extrapolated slope at low B and the saturation level at high B (dotted lines). The linear B-dependence observed at moderately low B values in both non-doped and Bi-doped Ca_3PbO are characteristic features of Dirac fermions.

4.3.2. 3D nature of the band structure

The ARPES intensity image in Fig. 4.5(c) shows the band structure along the X–Γ–X path of the k_z axis, generated from ARPES scans at photon energies from 256 eV to 371 eV with the inner potential of 8.5 eV [Fig. 4.4]. The intensities in the binding energy range less than 1 eV are not sufficient to describe the band structure of Ca_3PbO near E_F. To better visualize the band structure, the second-derivative ARPES spectrum is illustrated in Fig. 4.5(d). The bands marked as B1 and B2 are still not so easy to distinguish for the k_z direction, showing that the Δk_z broadening (~ 0.25 $Å^{-1}$) is too large to resolve these two bands that are also approximately 0.25 $Å^{-1}$ apart from each other. In addition, the suppression of the intensity can be ascribed to matrix element effects. Despite the limit of resolution, it becomes possible to confirm the emergence of B1/B2 bands in the lower binding energy range and determine the photon energy of 311 eV corresponding to Γ in the 3D BZ. Through comparison with the PBE calculations, the band near the E_F is assigned to the Pb-6$p_{3/2}$ derived bands, while the band whose top reaches 1.0 eV is attributed to the Pb-6$p_{1/2}$ derived one. The Pb-6p band structure is consistent with the results of PBE calculations, though the E_F is shifted downward from the Dirac points.

Next, in order to see the band dispersion in more detail, we investigated the band structure of Ca_3PbO along the k_x direction, which provides equivalent information to that of Figs. 4.5(c) and (d) but with much higher momentum resolution. Fig. 4.5(e) presents the resulting valence band structure along the X–Γ–X path of the k_x axis with $k_y = 0$ Å^{-1}, together with the plots of the peak positions of the momentum distribution curves (MDCs) and energy distribution curves (EDCs). The two Pb $6p_{3/2}$ bands marked as B1 and B2 cross the E_F and consequently form hole pockets around the Γ point. The presence of these hole pockets is in accord with the results of transport measurements which revealed *p*-type conductivity.

4.3.3. Estimation of the Dirac point position and bandwidth

To elucidate the measured dispersions in detail, we compared the observed band dispersion near the E_F with that of the PBE calculations for the B1 band, which directly passes through the theoretical Dirac points [Fig. 4.7(a)]. To enable a quantitative discussion, the band dispersion of B1 determined by extracting the peak positions of the MDCs and EDCs along the Γ-X line is reproduced with a linear least squares fit to the following phenomenological equation

$$E_{obs}(k_x) = E_{shift} + \alpha * E_{cal}(k_x). \quad (1)$$

where E_{cal}, E_{shift} and α represent the calculated band dispersion, the energy shift, and the correction factor of the band mass m^*, respectively. Only E_{shift} and α are adjustable parameters during the fit to the observed band dispersion. The best fit is obtained with $\alpha \sim 1.43(2)$ and $E_{shift} \sim 0.46(1)$ eV, showing that the bandwidth of the calculated B1 is expanded by 43 % in our Ca_3PbO sample. By reducing the bandwidth of the experimental B1 by 1.43, the Dirac points originating from the B1 are estimated to reside 0.32(1) eV

above the E_F. By assuming that the shape of actual band structure is similar to the calculated one, the hole concentration is estimated from the volume of Fermi surface obtained by calculated band structure with E_F shift of E_{shift} /α. The estimated concentration, 2.33×10^{20} cm^{-3} (B1: 2.07×10^{20} cm^{-3}, B2: 2.59×10^{19} cm^{-3}), almost agrees with the value ~ 1.4×10^{20} cm^{-3} obtained from the Hall measurements. In addition, Fig. 4.5(e) shows that all the three Pb-6*p* bands are well reproduced by Eq. (1) with the same parameters, although there are some discrepancies at the energy positions near stationary points such as Γ. The agreement between the modified calculated bands and the APRES spectra is further confirmed by the matching between the second-derivative ARPES spectra and the modified PBE calculations in Fig. 4.5(f).

4.3.4. Bi-substitution effect on band structure

Next, in order to examine the effects of Bi substitution on the electronic structure of Ca_3PbO, we performed ARPES measurements on Bi-doped Ca_3PbO. Before the ARPES measurement, we measured the core-level spectra of the Bi-doped samples to check for a shift of the E_F due to Bi substitution (electron doping), as shown in Fig. 4.6(a). In comparing the peak positions of the Pb 4*f* between the non-doped and the Bi-doped Ca_3PbO samples, it becomes clear that Bi-doping has induced a peak shift of ~ 0.12 eV toward higher binding energy, delineating the connection between Bi substitution and electron doping in Ca_3PbO.

Fig. 4.6(c) illustrates the ARPES intensity plots for a Bi-doped crystal along the X–Γ–X path of the k_x direction at $k_y = 0$ Å^{-1} [cut A in Fig. 4.6(b)], overlaid with the plots of the peak positions of the MDCs and EDCs. The B1 band is similarly reproduced with a fit to Eq. (1) [Fig. 4.7(b)]. The best fit is obtained with $\alpha \sim 1.06(1)$ and $E_{shift} \sim 0.188(6)$

eV. By reducing the bandwidth of the experimental B1 by 1.06, the Dirac points are estimated to be located 0.176(6) eV above the E_F. Then, hole concentration is estimated to be 8.72×10^{19} cm^{-3} (B1: 8.21×10^{19} cm^{-3}, B2: 5.06×10^{18} cm^{-3}), relatively consistent with the value ~ 6.9×10^{19} cm^{-3}obtained from Hall measurements. This result illustrates that the decrease in hole carrier concentration by Bi doping led to the decrease in the expansion of the bandwidth of the B1 from 43 % to 6 %. Although it is uncertain how the change in the bandwidth affects the massive Dirac states predicted in Ca_3PbO, it is evident that Bi doping contributes to the reformation of the bandwidth of the B1 to the theoretical one. The second-derivative ARPES spectra in Fig. 4.6(d) confirms the agreement between the experimental bands and modified calculated bands.

For a massive Dirac fermion, cone-like band dispersions show finite curvature at the Dirac points. In Ca_3PbO, the Dirac fermion is predicted to be massive so that the corresponding band dispersions do not directly pass the Dirac point; therefore, their shape should become parabolic as the bands approach the Dirac point, as verified in other massive Dirac fermion systems such as magnetically doped Bi_2Se_3 [140]. Fig. 4.6(e) displays the ARPES intensity plots for measurements along cut B, which runs through a single Dirac point in Fig. 4.6(b), together with the results of the PBE calculations along cut B modified by using the parameters obtained in the fit of the B1 band along cut A to Eq. (1). The second-derivative ARPES spectra in Fig. 4.6(f) show some intensity above the E_F due to thermal excitation energy of $2k_BT$ (~3 meV). However, the intensity at ~ 0.01 eV above the E_F is attributed to some noise produced by taking the second derivative. In accord with the form of the calculated band structure, which becomes parabolic at the Dirac point as shown in Figs. 4.6(e) and (f), that of the experimental band structure is also relatively parabolic, consistent with the feature of the massive Dirac states.

4.4. Conclusions

We performed ARPES measurements on Ca_3PbO to examine whether or not it possesses 3D Dirac fermions. Our observations of the bulk Dirac-like band dispersions near E_F via SX-ARPES were consistent with the results of electronic structure calculations. This good agreement between calculated and experimental dispersion strongly supports that Ca_3PbO is host to native 3D Dirac fermions. In addition, we showed that the substitution of Bi for Pb in Ca_3PbO led to the reduction of the excess hole carrier concentration, the shift of the Dirac point relative to the E_F, and the reformation of the expanded bandwidth of the band comprising the Dirac point. Furthermore, we confirmed that Ca_3PbO can be cleaved along the (001) plane, which preserves the C_4 symmetry. These findings encourage further electron doping in Ca_3PbO to directly investigate the possibility of a finite mass gap in the Dirac-like band dispersions and the more extensive exploration of the inverse perovskite family as a promising venue for 3D Dirac fermion systems.

Figures

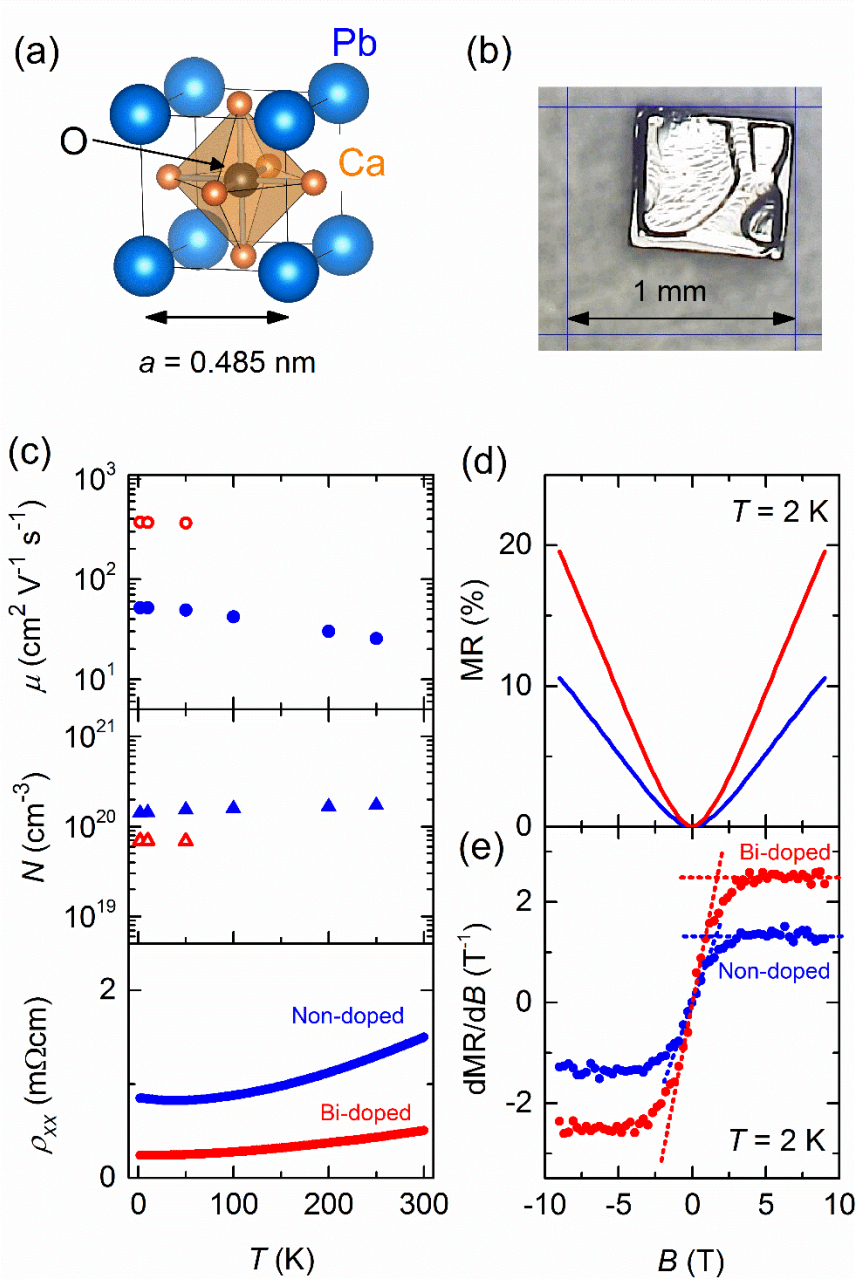

Figure 4.1: The sample and the electron transport properties of Ca_3PbO. (a) The crystal structure of Ca_3PbO. (b) Photograph of a Ca_3PbO single crystal with clear square-like facets. (c) Mobility, carrier density, and resistivity vs. temperature curves measured for Ca_3PbO and $Ca_3Pb_{0.92}Bi_{0.08}O$. (d),(e) Magnetoresistance (MR) and the first-order derivative of the MR with respect to magnetic field (B), dMR/dB, vs. B for Ca_3PbO and $Ca_3Pb_{0.92}Bi_{0.08}O$ at $T = 2$ K.

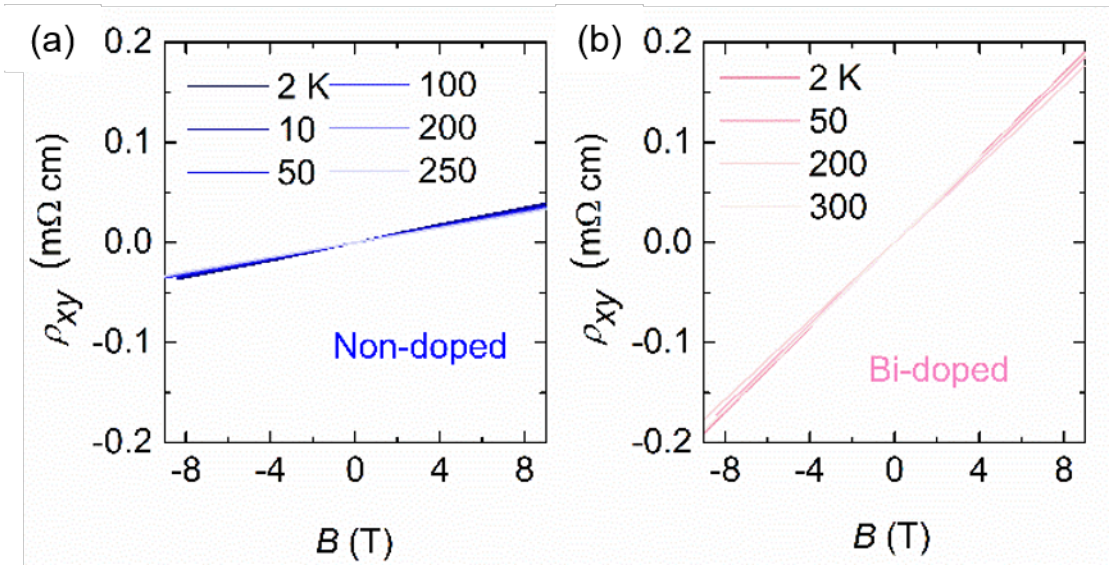

Figure 4.2: (a),(b) Magnetic field dependence of the Hall resistivity of Ca_3PbO (blue solid lines) and $Ca_3Pb_{0.93}Bi_{0.07}O$ (pink lines) at various temperatures, respectively.

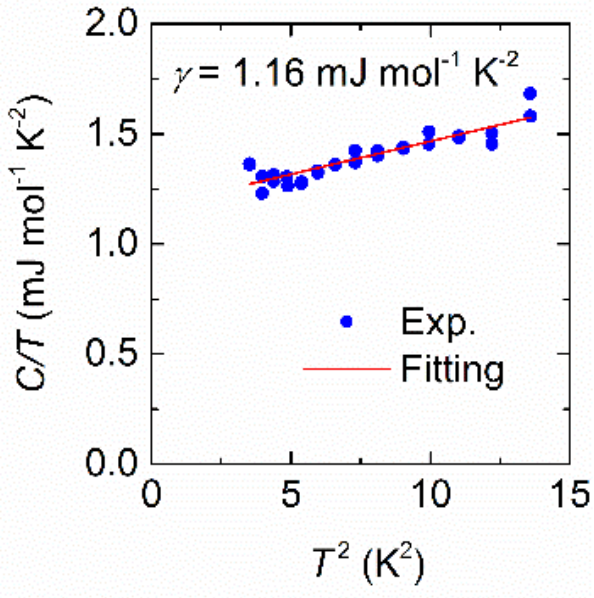

Figure 4.3: Specific heat divided by temperature, $C(T)/T$, as a function of T^2 in the low temperature region between 1.8 K and 3.7 K., shown as blue circles. The solid line represents the best-fit curve using the expression $C(T)/T = \gamma + \beta T^2$.

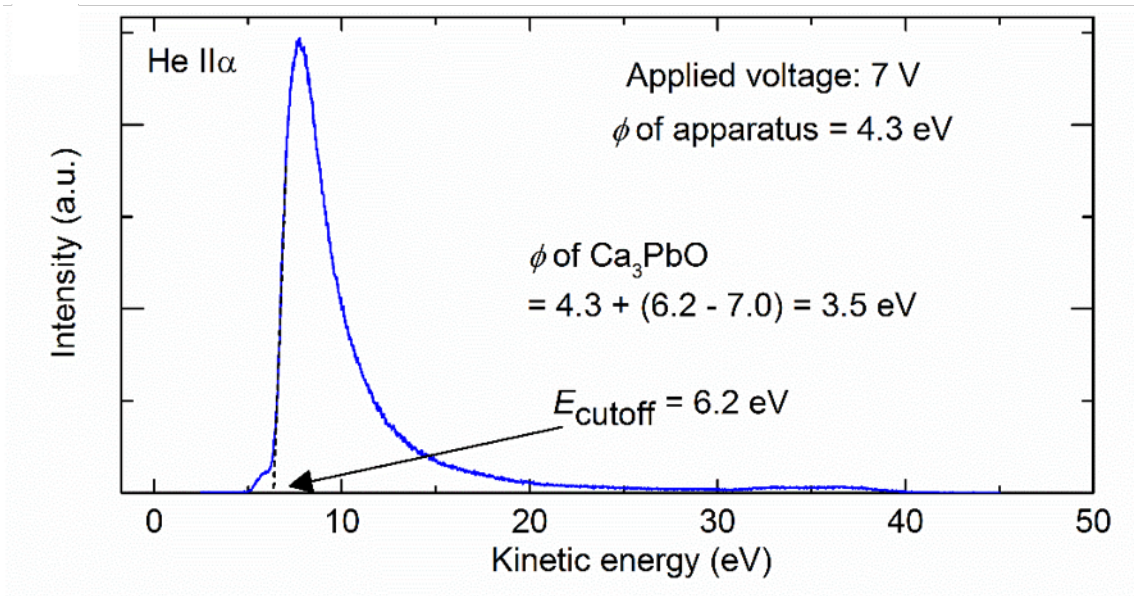

Figure. 4.4: (a) Secondary electron emission of the (001) surface of Ca_3PbO single crystals measured at an applied voltage of 7 V.

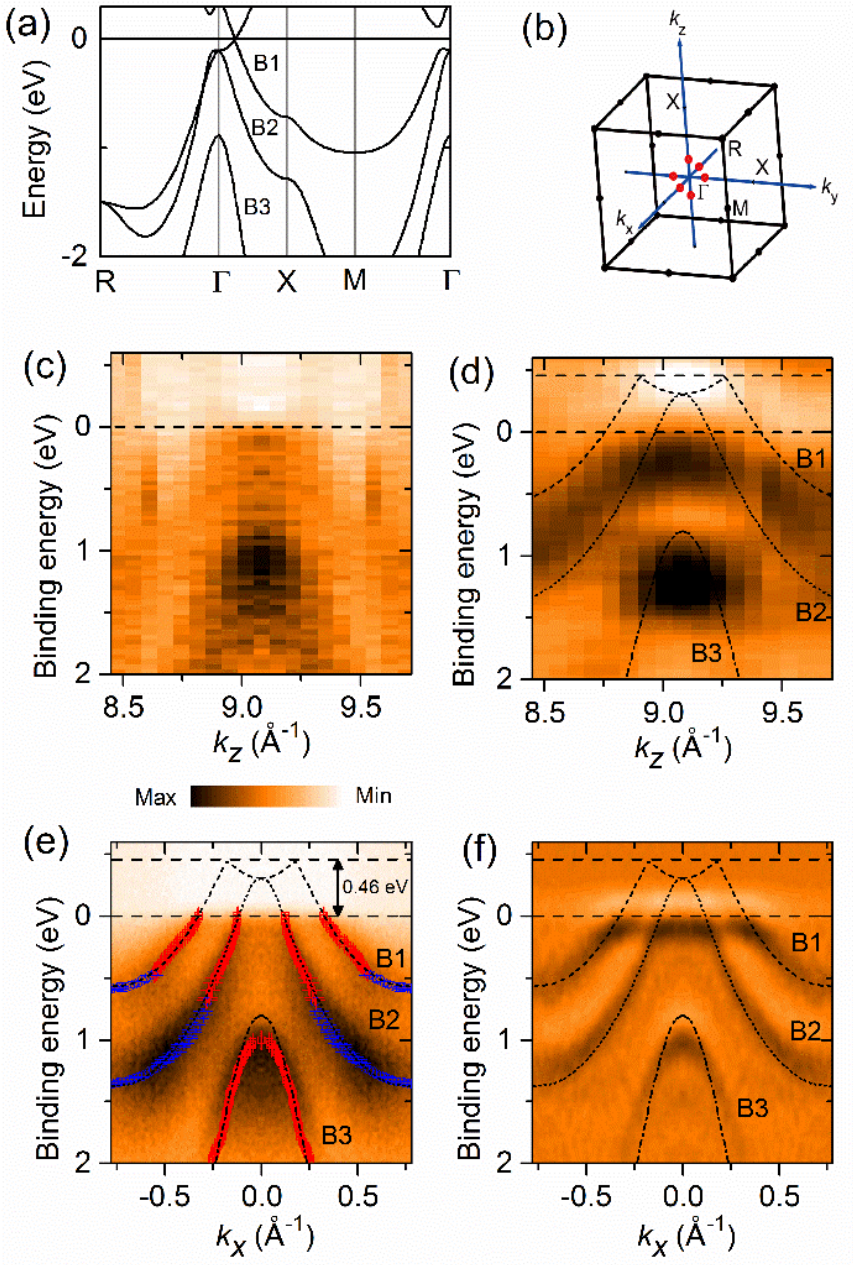

Figure 4.5: Comparison of the measured and theoretically calculated band structures of Ca_3PbO. (a),(b) The PBE-DFT band structure of Ca_3PbO and its bulk BZ. Red dots highlight the six 3D Dirac point positions. (c),(e) ARPES intensity plots along the Γ-X lines of the k_z and k_x directions, respectively. The peak positions of the MDCs and EDCs are plotted by the red open squares and blue open circles, respectively. The intensity plots are symmetrized with respect to the center lines and averaged (see Fig. 4.8). Black dashed lines represent the results of band structure calculations. (d),(f), Second-derivative ARPES spectra along the Γ-X lines of the k_z and k_x directions, respectively.

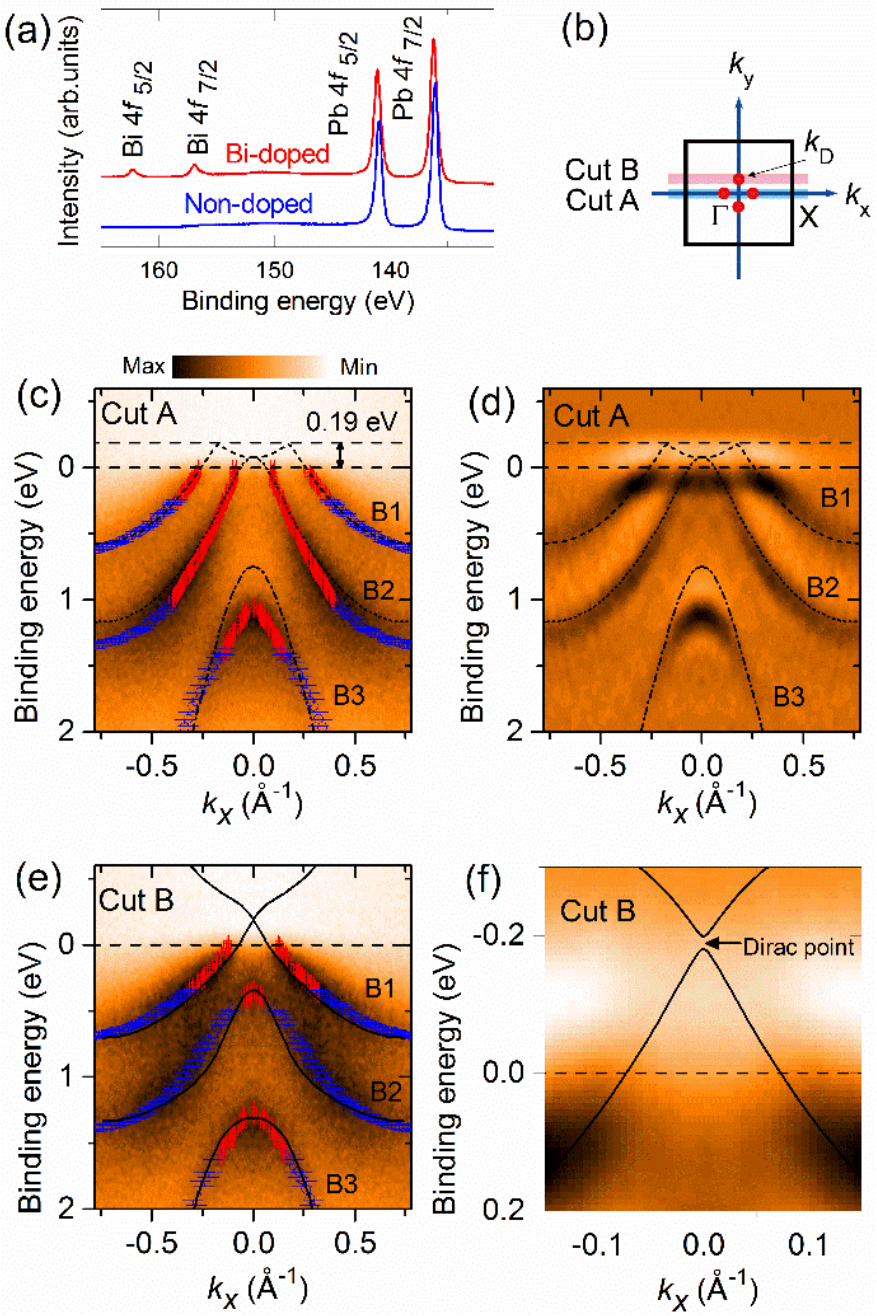

Figure 4.6: (a) Core-level photoemission spectra of Ca_3PbO and $Ca_3Pb_{0.92}Bi_{0.08}O$. (b) 2D cross-section of the BZ of Ca_3PbO. Red dots represent the four 3D Dirac points in the plane, denoted as k_D. (c),(e) ARPES intensity plots along cuts A and B, respectively, measured for a Bi-doped crystal. The peak positions of the MDCs and EDCs are plotted by the red open squares and blue open circles, respectively. (d),(f) Second-derivative ARPES spectra along cuts A and B, respectively. Black dashed and solid lines illustrate the results of band structure calculations for cut A and B, respectively.

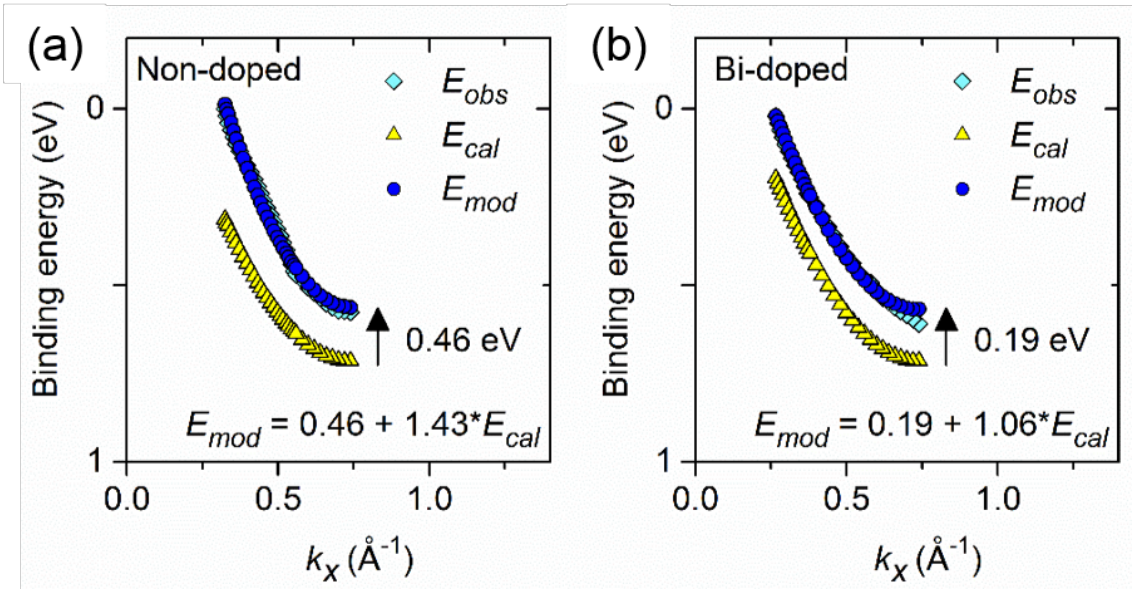

Figure 4.7: (a),(b) Comparisons between the observed binding energy E_{obs} of band B1 in Figs. 4.3(e) and 4.4(c) and the modified binding energy E_{mod} of the calculated B1 band, respectively. The E_{mod} is obtained by shifting the calculated binding energy E_{cal} toward lower binding energies by 0.46 eV for the non-doped Ca_3PbO crystal and 0.19 eV for the Bi-doped crystal. Light blue solid squares, yellow solid triangles, and blue solid circles show the E_{obs}, E_{cal}, and E_{mod} values, respectively.

To analyze the energy of the predicted Dirac points, we fit the peak positions of the momentum distribution curves (MDCs) and energy distribution curves (EDCs) of the B1 band along the Γ-X line in Figs. 4.3(e) and 4.4(c) to the linear equation $E_{obs} = E_{shift} + \alpha * E_{cal}$. E_{obs}, E_{cal}, E_{shift} and α represent the observed binding energy of B1 in the MDCs and EDCs, the calculated binding energy of B1, the energy shift between E_{obs} and E_{cal}, and the correction factor of the band mass m^*, respectively. Figs. 4.5(a) and (b) compare the E_{obs} and the modified binding energy of the calculated B1, which is represented by E_{mod}. It is clear that the E_{obs} values are well-reproduced by the E_{mod} ones in both the non-doped and Bi-doped cases. Based on the calculated Fermi surface for the non-doped and Bi-doped samples, the effective masses, m^*, of the band B1 are estimated to be ~ 0.69 m_0 and 0.52 m_0, respectively. These values are almost comparable to the thermal effective mass of the non-doped sample, m_{th}, obtained from our specific heat measurements of ~ 0.5 m_0 [Fig. 4.3].

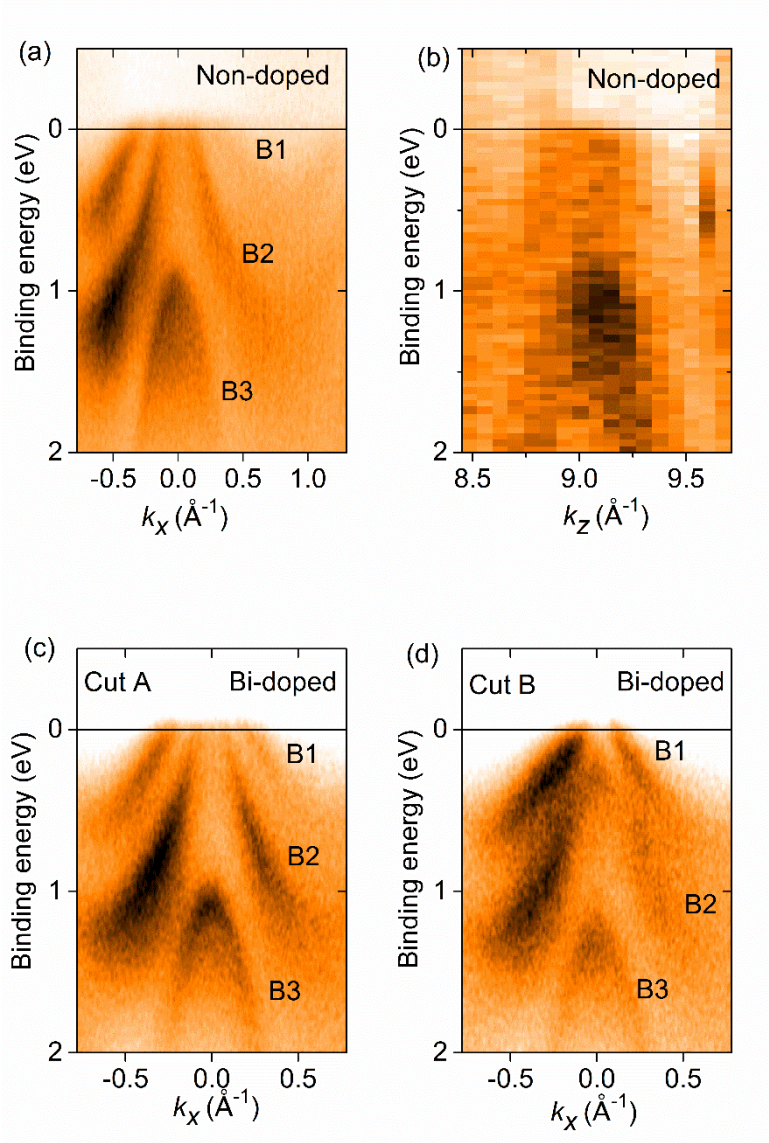

Figure 4.8:.(a)-(d) ARPES intensity plots for non-doped and Bi-doped Ca_3PbO crystals.

Chapter 5 Shubnikov-de Haas Oscillations in Ca_3PbO

5.1. Introduction

Three-dimensional (3D) Dirac fermion systems comprise a new class of topological materials where bulk conduction and valence bands with linear dispersion cross at discrete points or along curves in *k* space. These phenomena have been experimentally confirmed in topological semimetals incorporating those of the 3D Dirac [55–57,90,71,54,112], 3D Weyl [100–103,141–143], and topological nodal line semimetals [127,128]. Motivated by the growing interest for new Dirac materials, recent theoretical calculations on antiperovskite Ca_3PbO have predicted that there exists a 3D gapped Dirac-like cone along the Γ-X line [59], which stems from a band inversion of the Ca 3*d* and Pb 6*p* bands at the Γ point.

Following the prediction, we performed the angle-resolved photoemission spectroscopy (ARPES) experiments on Bi-doped Ca_3PbO single crystals to investigate the 3D electronic structure [144]. The ARPES and transport measurements revealed that the Bi-free samples were unintentionally heavily hole-doped so that the Fermi level (E_F) crosses not only the Dirac-like dispersion band but also the parabolic band. Thus, electron doping is necessary to assess the pure Dirac fermion system. Although the samples still remained *p*-type even after Bi doping to Pb site, it was shown that electron doping by Bi led to the Fermi level upward shifts to Dirac point without alternation of Dirac-like band structure [144].

In this study, we report the magnetotransport property of Bi-doped Ca_3PbO with Shubnikov-de Haas (SdH) oscillation demonstrating the emergence of Dirac fermion

system. Magnetotransport measurement is a straightforward method for detecting Dirac fermions as well as ARPES. The linear dispersion of energy band gives rise to linear quantum magnetoresistance (MR) at the quantum limit, where only the lowest Landau level crosses the E_F [139]. Another distinctive feature is the nontrivial π Berry phase shift [19], a phase generated from the cyclotron motion of electrons along a Dirac point. These characteristics have been widely confirmed in such Dirac materials as graphene [24,145], topological insulators [146–148], and topological semimetals [71,90,149–154].

For Bi-doped Ca_3PbO, we observed a linear MR at temperatures up to 40 K. The SdH oscillations are clearly discerned at low temperatures and reveal a non-trivial π Berry phase shift, complementary to previous ARPES measurements. Owing to the low effective mass and the existence of two SdH frequencies, one being twice the other, the Landau level splitting was observed at temperatures as high as 43 K. The field-angular-dependence of SdH frequencies in high magnetic field shows at least three branches corresponding to three pairs of uniaxial FS pockets on Γ-X path reflecting the cubic symmetry of bulk crystal.

5.2. Experimental

5.2.1. Synthesis

The details on the synthesis of $Ca_3(Pb_{1-x}Bi_x)O$ single crystals are provided in the chapter 3. The single crystals used in the SdH oscillation measurements were the ones obtained from the optimum synthesis conditions, i.e. they were grown in an iron crucible sealed in a stainless steel capsule in which two short stainless steel rods were placed at top and bottom sides of crucible to reduce open space. Due to the suppression of Ca

deficiency, the hole carrier density N in the grown crystal was decreased down to ~ 2.0 × 10^{19} cm^{-3} at 2 K which is about 1/3 of that in the ARPES study. The compositional formula of Bi-doped Ca_3PbO single crystals was determined to be $Ca_{2.92(9)}Pb_{0.98(3)}$ $Bi_{0.015(2)}O_{1.3(4)}$ by electron-probe microanalysis (EPMA), showing that the crystals still contain vacancies on approximately 2% of the Ca sites.

5.2.2. Magneto-transport measurements

Magnetotransport measurements were performed in the standard Hall and resistivity configuration using a Quantum Design 9T–Physical Property Measurement System (PPMS). Crystals were fixed on sapphire substrates by applying Stycast 2850 epoxy and contacted using silver epoxy in an argon glovebox to avoid exposure to an ambient atmosphere, and were then immersed in Paratone-N oil before transferring the sample to the measurement chamber in PPMS. Quantum oscillations measurements with a tunnel diode oscillator technique (TDO) [152] were also conducted by attaching the samples to a copper coil of ~8 turns that comprises part of a TDO circuit, resonating at ~82 MHz. The sample with coil was rotated *in situ*, θ being the angle between the magnetic flux density $\boldsymbol{B}$ and the [001] direction. Magnetic fields ($\mu_0 H$) of up to 55 T were applied by the nondestructive pulse magnet at the ISSP. The magnetization of sample is neglected in the following sections ($B = \mu_0 H$). To provide a theoretical reference with which to compare our magnetotransport results, we performed DFT band structure calculations with the Perdew-Burke-Ernzerhof (PBE) generalized-gradient approximation [136] using the VASP code [137], while the effective mass and hole carrier concentration were calculated using SKEAF code [138].

5.3. Results and discussion

5.3.1. SdH oscillations under low fields

Fig. 5.1(a) shows the magnetoresistance (MR) ratio (%) [ρ(B) – ρ(0)]/ ρ(0) × 100 as a function of B up to 9 T at temperatures between 2 and 40 K with a field applied along the c axis (i.e., $\boldsymbol{B}\perp ab$ plane). The linear B-dependence of the MR ratio is confirmed by the derivative of the longitudinal resistance dR_{xx}/dB curve [inset in Fig. 1(a)], consistent with the previous report [144]. SdH oscillations can be resolved from as low as B = 5 T in both MR and Hall resistance R_{xy} with the help of the derivatives dR_{xx}/dB and dR_{xy}/dB, as shown in Figs. 5.1(a) and (b), respectively.

By subtracting a polynomial background of R_{xx} at 2 K < T < 40 K, SdH oscillations periodic in 1/B are observed [Fig. 5.1(c)]. The fast Fourier transform (FFT) spectrum of the SdH oscillations as a function of B at 2 K [the inset in Fig. 5.1(c)] reveals a single oscillation frequency F = 41.5 T, which corresponds to the periodicity Δ(1/B) = 0.024 T^{-1}. According to the Onsager relation, $F = (\hbar/2\pi e)S_F$, where $\hbar$ is Planck's constant and S_F is a cross-sectional area of FS normal to the field, we obtain $S_F = 3.9 \times 10^{-3}$ Å^{-2}, a tiny area corresponding to only 0.2 % of the cross-sectional area of the first Brillouin zone (BZ). By assuming a circular cross section, a very small Fermi wave vector of k_F = 0.035 Å^{-1} is estimated.

Quantum oscillation of resistance ΔR_{xx} can be described by Lifshitz-Kosevich (LK) formula [69,70]:

$$\frac{\Delta R_{xx}}{\Delta R_{xx}(0)} = C\sum_{p=1}^{\infty} R_T R_D R_s \frac{1}{\sqrt{p}} \cos\left[2\pi p\left(\frac{F}{B} - \frac{1}{2} + \phi_D + \phi_B\right)\right] \quad (1)$$

where $\Delta R_{xx}(0)$ is the background resistivity, C is a positive coefficient, and p represents the pth harmonic oscillation. The temperature and the Dingle factors are

expressed as $R_T = \lambda(T)/\sinh(\lambda(T))$ and $R_D = e^{-\lambda_D}$ with $\lambda_{(D)} = 2\pi^2 p k_B T_{(D)} m^*/(\hbar e B)$, where k_B and m^* represent the Boltzmann constant and the effective cyclotron mass. The spin damping factor is given by $R_S = \cos\left(p\pi \frac{g}{2}\mu^*\right)$, where $\mu^* = m^*/m_0$ with m_0 being the bare electron mass, and g represents the spin g factor. The phase factor ϕ_D is determined by the dimensionality of the FS, and the value varies from 0 for 2D FS to + or – 1/8 for a minimum or maximum cross section of 3D FS, respectively [69,70]. Another phase factor ϕ_B is the Berry phase, which is 0 for normal electrons but 1/2 for Dirac fermions [69]. Due to the maximum cross section of the FS, the total phase shift ϕ for Ca_3PbO is predicted to be 3/8.

Figure 5.1(d) shows the temperature dependence of the relative oscillatory component $\Delta R_{xx}(T)/\Delta R_{xx}(2\text{ K})$ for the peak at $1/B = 0.135\ \text{T}^{-1}$. For simplicity, we have neglected harmonics here. The fit yields $m^* \sim 0.046\ m_0$ with m_0 the bare electron mass. Subsequently, the Fermi velocity $v_F = \hbar k_F/m^*$ is calculated to be $v_F = 8.77 \times 10^5$ m/s. A long mean free path of $l_q = 26$ nm can be extracted from the Dingle plot [the inset in Fig. 5.1(d)]. The quantum mobility μ_q calculated by $\mu_q = e\tau_q/m^*$ is 1132 $\text{cm}^2\ \text{V}^{-1}\ \text{s}^{-1}$. The values of these band parameters are comparable to those of well-studied 3D Dirac fermion systems such as Cd_3As_2 [71,89].

5.3.2. Lande *g* factor and Berry phase

Next, we consider the spin reduction factor R_S and oscillation phases. For the analysis of the g factor, the spin-zero method has been widely used in quantum oscillation studies on two-dimensional (2D) or quasi-2D materials such as organic metals [153], high-T_c cuprates [154,155], and iron-based superconductors [156]. The cross-sectional area of FS in a quasi-2D metal increases as a function of $1/\cos\theta$ while

tilting the field, leading to an increase in cyclotron mass, $\mu^*(\theta) = \mu^*(0)/\cos\theta$. Substitution of this θ-dependence in the equation of R_S results in a periodic disappearance of R_S with the spin-zero condition for the fundamental harmonic, $g\mu^*(\theta) = 2n + 1$, where n is an integer [153]. Thus, to determine the values of the two unknowns, $g\mu^*(\theta)$ and n, at least two successive spin-zero angles need to be detected.

Figure 5.2 shows the oscillatory components of the resistance as a function of $1/(B\cos\theta)$ at various angles of the magnetic field with respect to the normal of the sample surface, measured for another sample with $m^*(0) \sim 0.074\ m_0$. The curves at θ = 0° and 5° show a maximum near F/B = 11, while that at θ = 25° shows a minimum, suggesting that the first spin-zero exists between θ = 0° and 25°. Likewise, the second spin-zero can be identified between θ = 25° and 45° near F/B = 13.5. Furthermore, by looking at the curves near F/B = 14.5, we can see that the waveform at θ = 45° almost remains the same until θ = 50°, whereas it is hard to distinguish the curve at θ = 55°.

Under an assumption that the first spin-zero is at θ = 15±5° with μ^*= 0.076, we can obtain a g-factor, $g = 13.12(2n + 1)$. If we take n = 2 ($g = 66(1)$), the second spin-zero emerges at θ = 46.4°, which is consistent with the experimental observations. No other values for n can explain the positions and number of spin-zeros detected in the experiment; that is, n < 2 does not account for the second spin-zero while n > 2 yields extra spin-zeros. With $g = 66(1)$ and $\mu^* = 0.046$ at θ = 0°, the phase of R_S for the oscillations shown in Fig. 1(c), $\pi\frac{g}{2}\mu^*$, is estimated to be 1.52π and hence R_S > 0. This considerably large g factor suggests the existence of strong spin-orbit coupling in Ca_3PbO, which is predicted to account for the band inversion at Γ leading to the emergence of 3D Dirac fermions in Ca_3PbO.

We now evaluate the phase shift ϕ for Ca_3PbO. The nontrivial π Berry phase has

been recognized as a hallmark of various Dirac materials [24,71,146,156], and ϕ can be determined either directly from the fit to the LK formula or the Landau level (LL) index plot. Figure 5.3(a) shows the oscillatory component of magnetoconductivity $\sigma_{xx}(\mathrm{B})$ of the sample (characterized by Fig. 5.1) as a function of 1/B at 2 K, obtained by using the formula $\sigma_{xx}(\mathrm{B}) = \rho_{xx}/(\rho_{xx}^2 + \rho_{xy}^2)$, where ρ_{xx} and ρ_{xy} are the longitudinal and Hall resistivities, respectively. The LK fit of $\Delta\sigma_{xx}$ yields the total phase shift of ϕ = 0.376(3), which is closely equivalent to the value predicted for Ca_3PbO. In addition, to perform the LL index plot, we assign LL integer indices n to minima in $\Delta\sigma_{xx}$ and half indices to maxima in $\Delta\sigma_{xx}$ [157], shown in Fig. 3(b). In case of $R_S > 0$, the nth minimum in $\Delta\sigma_{xx}$ satisfies the following relation [158]

$$2\pi\left(\frac{F}{B} - \frac{1}{2} + \phi\right) = (2n-1)\pi \qquad (2)$$

Thus, the plot of n vs 1/B makes a straight line with F and ϕ corresponding to the slope and the intercept on the n axis, respectively. The best-fit straight line in Fig. 5.3(b) intercepts the n axis at the value ϕ = 0.36(5), consistent with the value derived from the LK fit. However, in a recent theoretical work, it is argued that the phase shift ϕ in the fundamental oscillation should not be interpreted as direct evidence for 3D Dirac fermions, emphasizing that it represents a phase defined by spin-orbit coupling constant λ, further accounting for the Zeeman contribution [159]. With this new definition, further theoretical studies are required to evaluate the phase shift expected for Ca_3PbO.

5.3.3. Zeeman splitting

To investigate the quantum limit of the SdH oscillations at high fields, we performed TDO measurements instead of using the standard four-probe configuration method, which was unfeasible for our samples due to the difficulty of making stable contacts for the

measurements in pulse magnetic fields. Figure 5.4(a) shows the field dependence of the resonant frequency up to 55 T at temperatures between 4 and 78 K with the field applied normal to the (001) plane. The frequency variation Δf_{TDO} represents the change in the conductance of the sample following the relation, $\Delta f_{TDO} \propto 1/\rho_{xx}$, where ρ_{xx} is longitudinal resistivity.

To conduct background subtraction, we use the linear interpolation of the raw data at 78 K. The FFT spectrum [inset in Fig. 5.4(a)] at low fields (5 T < B < 11 T) reveals a single oscillation frequency F = 41.5 T, consistent with the results of the four-probe configuration measurements in DC magnetic fields. In contrast, the oscillatory component Δf_{TDO}^{OSC} at 4 K [blue line in Fig. 5.4(a)] in the high-field range (5 T < B < 55 T) shows oscillations with multiple frequencies, which appear as additional peaks other than the peak at F = 41.5 T in the FFT spectrum [Fig. 5.4(b)]. Regarding the origins of these extra peaks, we consider two candidates: other extremal orbits due to anisotropy of the Fermi surfaces and harmonics generation by Zeeman splitting.

Our DFT calculation predicts that bulk Fermi surface of slightly hole-doped Ca_3PbO forms three pairs of nearly ellipsoidal hole pockets on Γ-X lines, α_x, α_y, and α_z, which can be transferred to each other by cubic crystal symmetry [59]. The inset in Fig. 5.4(b) depicts the schematic image of α_x, α_y, and α_z in the 3D BZ of Ca_3PbO. Actually, our previous ARPES measurement demonstrated the existence of hole pockets on Γ-X lines and the distinct Fermi velocities along the two cuts crossing either a single or double Dirac points [144]. In particular, the DFT calculation shows that the cross-sectional area of α_z is approximately twice as large as that of α_x when the field applied along the k_x axis [$\theta = 90°$ in the inset shown in Fig. 5.4(b)]. In this case, as the angle between the field and the [001] direction increases, the oscillation with F = 41.5 T (α_z) would increase and

gradually approach that with F = 83 T, whereas the oscillation with F = 83 T (α_x) would decrease and gradually approach that with F = 41.5 T. As for the Zeeman splitting, the peaks in the FFT spectra would always appear twice as large as α_x and α_z.

5.3.4. Angular dependence of SdH oscillations under high fields

To verify the ellipsoidal FS model and clarify the origins of oscillation with high frequencies, we performed the angle-dependent TDO measurements by tiling the magnetic field from the [001] direction (θ = 0°) to the [00-1] direction (θ = 180°), which passes through the [100] (θ = 90°) direction [see Fig. 5.4(f)]. Figure 5.5(a) shows the oscillatory components $\Delta f_{\mathrm{TDO}}^{\mathrm{OSC}}$ at various angles in the field range from 5 T to 55 T, where the split spacing markedly changes with θ, which can be simply attributed to the angular-dependent effective mass.

Figure 5.5(b) shows the FFT peak positions plotted as a function of θ. The solid and open dots represent the peaks with high and low amplitudes, respectively. To confirm the dimensionality of the SdH oscillations, we use the ellipsoidal FS model parameterized by α_x, α_y, and α_z, each of them representing the oscillation frequency corresponding to the cross-sectional area of the ellipsoidal FS along the Γ-X path of the k_x, k_y, or k_z axis, respectively. As shown in the inset depicted in Fig. 5.4(b), while tilting the field from the [001] to the [100] direction, α_y would remain constant. On the other hand, α_x and α_z would vary with the field angle by following the equation (with a $\pi/2$ shift for α_x) [138]:

$$F(\theta) = \alpha_{x(\theta=0^\circ)}\alpha_{z(\theta=0^\circ)}\sqrt{(\cot^2\theta + 1)/\left(\alpha_{x(\theta=0^\circ)}^2\cot^2\theta + \alpha_{z(\theta=0^\circ)}^2\right)} \qquad (1)$$

where $F(\theta)$, $\alpha_{x(\theta=0^\circ)}$, and $\alpha_{z(\theta=0^\circ)}$ represent the oscillation frequencies as a function of θ and the two primary frequencies α_x = 41.5 T and α_z = 83 T. The ellipsoidal FS model can describe the angular dependence of the oscillation frequencies well up to the second-

order harmonics of α_x, α_y and α_z. Most of the peaks with low amplitudes [open dots in Fig. 5.5(b)] can be attributed to combination frequencies of α_x, α_y and α_z [dashed lines in Fig. 5.5(b)]. Some peaks with low amplitudes at $\theta = 6°$, 175°, and 185° may originate from the difference between the two frequencies of $F \sim 100$ T and 40 T.

As shown in Fig. 5.5(b), the angular dependence of SdH oscillations agrees well with simulated results for the ellipsoidal Fermi surface model, demonstrating the existence of multiple extremal orbits due to the anisotropic Fermi surfaces, α_x and α_z, as well as their harmonics due to Zeeman splitting, $2\alpha_x$ and $2\alpha_z$. The next question is which oscillatory amplitude is more predominant than that of the other at such angles as $\theta = 45°$ where contributions from these two origins, $\alpha_x + \alpha_z$ and $2\alpha_x$ (or $2\alpha_z$), exactly cross each other. This can be solved by looking at the adjacent angles where the oscillatory amplitude of $2\alpha_x$ (or $2\alpha_z$) is higher than that of $\alpha_x + \alpha_z$. Thus, we conclude that the high-frequency components observed at $\theta = 90°$ are dominated by harmonics of α_x and α_z oscillations. As a whole, the angular dependence of the 3D SdH oscillations provides evidence for the presence of three pairs of 3D Fermi pockets with uniaxial anisotropy along the Γ-X path in bulk Ca_3PbO, as predicted by the DFT calculation in Ref. [59].

5.4. Conclusions

By observing the SdH oscillations, we have resolved the bulk FS of Bi-doped Ca_3PbO with distinctive features of Dirac fermions including linear magnetoresistance, light effective mass, and a nontrivial π Berry phase shift. Owing to the carriers with low effective mass and the two primary SdH frequencies, one being twice the other, the Landau level splitting was clearly observed at temperatures as high as 43 K. The field-angular-dependence of the oscillation frequencies with three branches reveals that the FS

is composed of three pairs of hole pockets with uniaxial anisotropy on the Γ-X path as predicted for bulk Ca_3PbO crystal by DFT calculation.

Figures

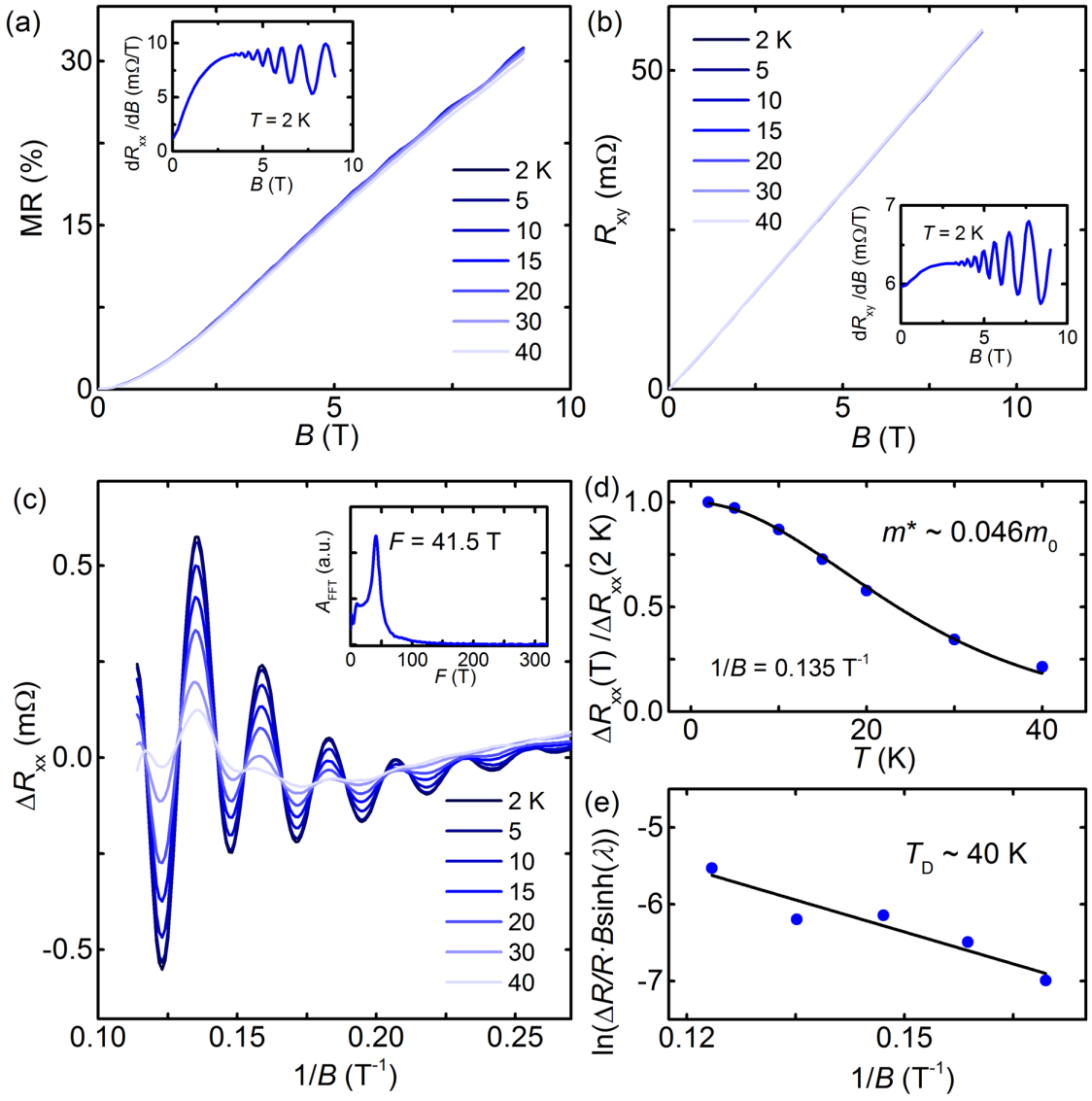

FIG. 5.1. SdH oscillations under DC fields and Fermi surface parameters. (a),(b) MR and R_{xy} vs. B for Bi-doped Ca_3PbO up to 9 T at temperatures between 2 K and 40 K. The insets show the derivatives dR_{xx}/dB and dR_{xy}/dB vs. B at 2 K, respectively. (c) Oscillatory component of longitudinal resistivity ΔR_{xx} vs. $1/B$ at various temperatures. The inset shows the FFT spectrum of the SdH oscillations at 2 K. (d) Oscillation amplitudes $\Delta R_{xx}(T)/\Delta R_{xx}$ (2 K) vs. T for the peak at $1/B = 0.135$ T^{-1}. (e) Dingle plot of the SdH oscillations with the oscillation frequency $F = 41.5$ T.

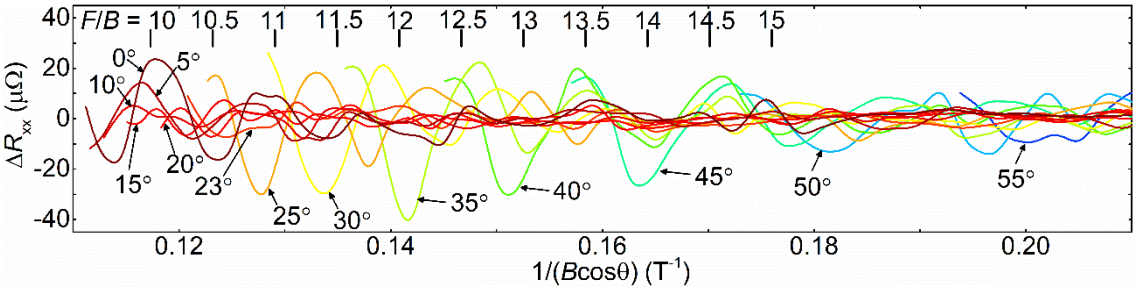

FIG. 5.2. Oscillatory components of the resistance as a function of $1/(B\cos\theta)$ at various angles, measured for another sample with $m^*(0) \sim 0.074\ m_0$.

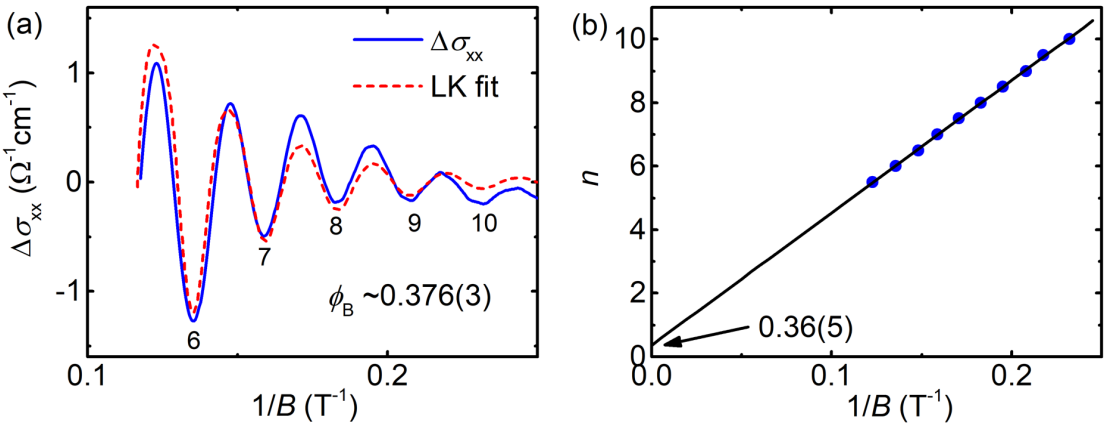

FIG. 5.3. (a) Oscillatory component of magnetoconductivity of the Bi-doped Ca_3PbO single crystal, characterized by transport properties shown in Fig. 1, $\Delta\sigma_{xx}$ vs. $1/B$ fitted to the Lifshitz-Kosevich formula. The minima positions are assigned as integer Landau level indices. (b) Landau level index plot.

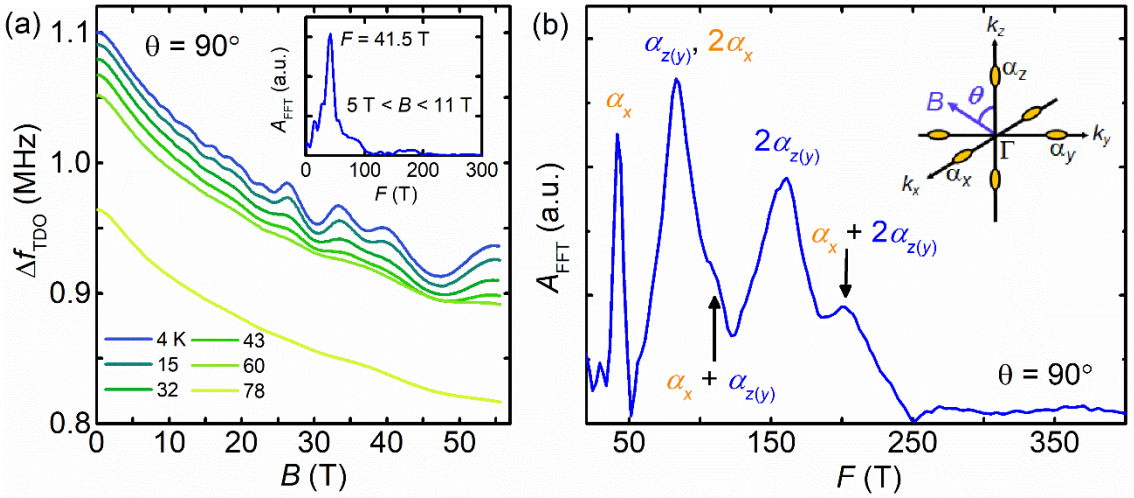

FIG. 5.4. High magnetic field data obtained from TDO measurements. (a) Resonant frequency, Δf_{TDO}, vs. B up to 55 T at temperatures between 4 and 78 K with the field applied normal to the (001) plane. The inset shows the FFT spectrum of the SdH oscillations at 4 K for fields between 5 T and 11 T. (b) FFT spectra of oscillatory component Δf_{TDO}^{OSC} at 4 K. The peaks are assigned as α_x and α_z with their second harmonics and their combinations. The inset shows the schematic image of the ellipsoidal FS in the 3D BZ of Ca_3PbO.

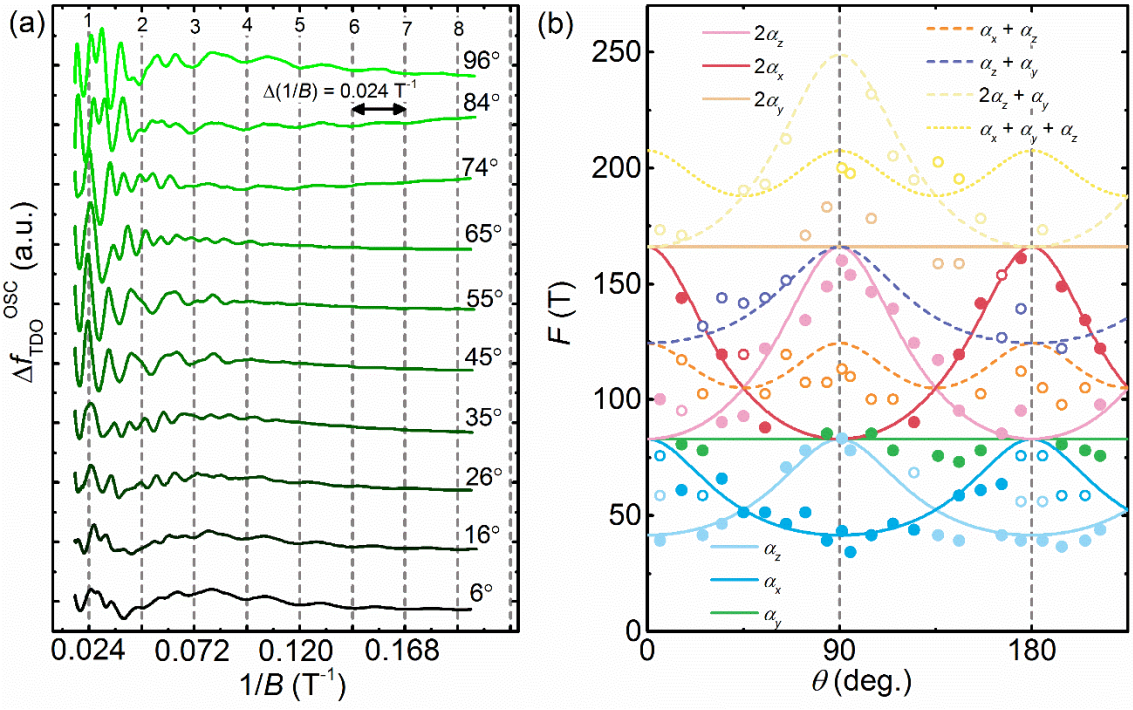

FIG. 5.5. Angular dependence of SdH oscillations under high magnetic fields. (a) Oscillatory component $\Delta f_{\mathrm{TDO}}{}^{\mathrm{OSC}}$ at various angles. (b) Angular dependence of the FFT peak positions. The solid and dashed lines show the simulated results for the 3D ellipsoidal model using harmonics and combinations, respectively. The solid and open dots represent the FFT peaks with high and low amplitudes.

Chapter 6 General Conclusion

To observe three-dimensional Dirac fermions in Ca_3PbO, we synthesized the single crystals of Ca_3PbO. By employing angle-resolved photoemission spectroscopy, we observed the Dirac-like energy dispersion along the $\Gamma - X$ direction in the Brillouin zone of bulk Ca_3PbO. In addition, we performed magnetotransport measurements to detect Dirac fermions. Analysis of the prominent Shubnikov-de Haas oscillations in Bi-doped Ca_3PbO demonstrates clear evidence for the bulk 3D Fermi surface with a nontrivial Berry phase shift and very light effective masses. TDO measurements under high fields reveal the existence of two primary SdH frequencies, one being twice the other. Together with the low effective mass, the oscillations of these two frequencies account for the emergence of the Landau level splitting which persists up to 43 K. The field-angular-dependence of the oscillation frequencies with three branches reveals that the FS is composed of three pairs of hole pockets with uniaxial anisotropy on the Γ-X path as predicted for bulk Ca_3PbO crystal by DFT calculation.

In chapter 1, the relevant theoretical backgrounds of the studies of 3D Dirac fermions are briefly introduced. Based on the backgrounds, the objectives and the contents of the present studies are described.

In chapter 2, the basic principles of the two main experimental techniques in this study, angle-resolved photoemission spectroscopy and quantum oscillations, are briefly introduced. For quantum oscillations, the experimental background on the verification of the non-trivial Berry phase shift is described in detail.

In chapter 3, the single crystal growth of Ca_3PbO by a Ca-self-flux method is discussed. Cubic crystals, 1 mm in size, were successfully obtained through the use of iron crucibles sealed in stainless steel capsules. The crucible material and sealing method were found to be critical factors for achieving large crystals with low carrier density. The crystals were subsequently characterized by powder and single-crystal x-ray diffraction experiments, electron-probe microanalysis, and Hall effect measurements. Through the use of short stainless steel rods as tight caps for the crucible and fillers to occupy extra space in the capsule, the Ca evaporation loss of the flux, which contributes to Ca vacancy formation, was effectively reduced. Hence, the hole carrier density in the single crystal was reduced to 4.0×10^{19} cm^{-3}. The crystal synthesized under optimized growth conditions showed clear Shubnikov-de Haas oscillations, indicating its high purity and homogeneity.

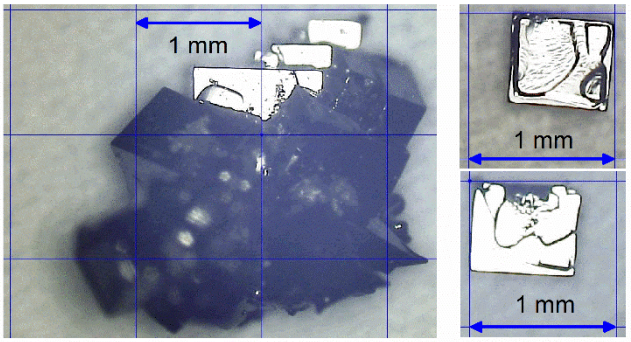

In chapter 4, the band structure of Ca_3PbO is investigated through soft x-ray angle-resolved photoemission spectroscopy. Cone-like band dispersions were observed for Ca_3PbO, in close agreement with the predictions of electronic structure calculations. The analysis on the band width of the cone-like dispersion and the shift in the Fermi level demonstrate that chemical substitution of Bi for Pb is effective in tuning the Fermi level of Ca_3PbO while leaving

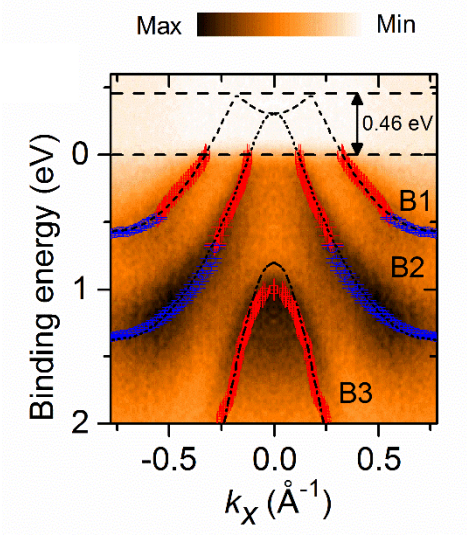

its electronic structure intact. It is confirmed that the inverse perovskite family provides a promising platform for the exploration of 3D Dirac fermion systems.

In chapter 5, magnetotransport and tunnel diode oscillation measurements were performed on Bi-doped Ca_3PbO in magnetic fields up to 55 T and temperatures between 2 K and 78 K. The observations of the SdH oscillations reveal the bulk 3D Fermi surface (FS) with distinctive features of Dirac fermions including linear magnetoresistance, light effective mass, and a nontrivial π Berry phase shift. Owing to the carriers with low effective mass and the two primary SdH frequencies, one being twice the other, the Landau level splitting was clearly observed at temperatures as high as 43 K. The field-angular-dependence of the oscillation frequencies with three branches reveals that the FS is composed of three pairs of hole pockets with uniaxial anisotropy on the Γ-X path as predicted for bulk Ca_3PbO crystal by DFT calculation.

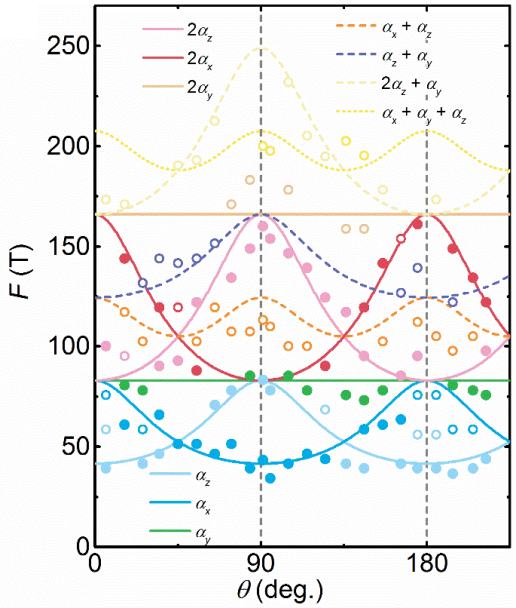

References

[1] M. V. Berry, Proc. R. Soc. Lond. Math. Phys. Sci. **392**, 45 (1984).

[2] D. Xiao, M.-C. Chang, and Q. Niu, Rev. Mod. Phys. **82**, 1959 (2010).

[3] R. Resta, Rev. Mod. Phys. **66**, 899 (1994).

[4] R. D. King-Smith and D. Vanderbilt, Phys. Rev. B **47**, 1651 (1993).

[5] T. Thonhauser, D. Ceresoli, D. Vanderbilt, and R. Resta, Phys. Rev. Lett. **95**, 137205 (2005).

[6] D. Xiao, J. Shi, and Q. Niu, Phys. Rev. Lett. **95**, 137204 (2005).

[7] J. Shi, G. Vignale, D. Xiao, and Q. Niu, Phys. Rev. Lett. **99**, 197202 (2007).

[8] K. v. Klitzing, G. Dorda, and M. Pepper, Phys. Rev. Lett. **45**, 494 (1980).

[9] D. J. Thouless, M. Kohmoto, M. P. Nightingale, and M. den Nijs, Phys. Rev. Lett. **49**, 405 (1982).

[10] M. Kohmoto, Ann. Phys. **160**, 343 (1985).

[11] T. Jungwirth, Q. Niu, and A. H. MacDonald, Phys. Rev. Lett. **88**, 207208 (2002).

[12] N. Nagaosa, J. Sinova, S. Onoda, A. H. MacDonald, and N. P. Ong, Rev. Mod. Phys. **82**, 1539 (2010).

[13] S. Murakami, N. Nagaosa, and S.-C. Zhang, Science **301**, 1348 (2003).

[14] Y. K. Kato, R. C. Myers, A. C. Gossard, and D. D. Awschalom, Science **306**, 1910 (2004).

[15] V. Sih, R. C. Myers, Y. K. Kato, W. H. Lau, A. C. Gossard, and D. D. Awschalom, Nat. Phys. **1**, 31 (2005).

[16] J. Wunderlich, B. Kaestner, J. Sinova, and T. Jungwirth, Phys. Rev. Lett. **94**, 047204 (2005).

[17] M. Z. Hasan and C. L. Kane, Rev. Mod. Phys. **82**, 3045 (2010).

[18] Y. Ando, J. Phys. Soc. Jpn. **82**, 102001 (2013).

[19] G. P. Mikitik and Y. V. Sharlai, Phys. Rev. Lett. **82**, 2147 (1999).

[20] G. P. Mikitik and Y. V. Sharlai, Phys. Rev. Lett. **93**, 106403 (2004).

[21] G. P. Mikitik and Y. V. Sharlai, Low Temp. Phys. **33**, 439 (2007).

[22] R. G. Goodrich, D. L. Maslov, A. F. Hebard, J. L. Sarrao, D. Hall, and Z. Fisk, Phys. Rev. Lett. **89**, 026401 (2002).

[23] K. S. Novoselov, A. K. Geim, S. V. Morozov, D. Jiang, Y. Zhang, S. V. Dubonos, I. V. Grigorieva, and A. A. Firsov, Science **306**, 666 (2004).

[24] K. S. Novoselov, A. K. Geim, S. V. Morozov, D. Jiang, M. I. Katsnelson, I. V. Grigorieva, S. V. Dubonos, and A. A. Firsov, Nature **438**, 197 (2005).

[25] Y. Zhang, Y.-W. Tan, H. L. Stormer, and P. Kim, Nature **438**, 201 (2005).

[26] P. a. M. Dirac and F. R. S, Proc R Soc Lond A **133**, 60 (1931).

[27] S. Murakami, New J. Phys. **9**, 356 (2007).

[28] X.-L. Qi and S.-C. Zhang, Rev. Mod. Phys. **83**, 1057 (2011).

[29] J. Goryo, Lecture notes on the theory of topological insulators (in Japanese). Bussei Kenkyu **96**,

187 (2011).
[30] H. B. Nielsen and M. Ninomiya, Phys. Lett. B **130**, 389 (1983).
[31] S. L. Adler, Phys. Rev. **177**, 2426 (1969).
[32] J. S. Bell and R. Jackiw, Il Nuovo Cimento 1965-1970 **60**, 47 (1969).
[33] C. L. Kane and E. J. Mele, Phys. Rev. Lett. **95**, 226801 (2005).
[34] G. W. Semenoff, Phys. Rev. Lett. **53**, 2449 (1984).
[35] L. Fu and C. L. Kane, Phys. Rev. B **74**, 195312 (2006).
[36] L. Fu and C. L. Kane, Phys. Rev. B **76**, 045302 (2007).
[37] A. N. Redlich, Phys. Rev. D **29**, 2366 (1984).
[38] H. B. Nielsen and M. Ninomiya, Phys. Lett. B **105**, 219 (1981).
[39] L. Fu, Phys. Rev. Lett. **106**, 106802 (2011).
[40] T. H. Hsieh, H. Lin, J. Liu, W. Duan, A. Bansil, and L. Fu, Nat. Commun. **3**, 982 (2012).
[41] A. Alexandradinata, C. Fang, M. J. Gilbert, and B. A. Bernevig, Phys. Rev. Lett. **113**, 116403 (2014).
[42] X. Wan, A. M. Turner, A. Vishwanath, and S. Y. Savrasov, Phys. Rev. B **83**, 205101 (2011).
[43] K.-Y. Yang, Y.-M. Lu, and Y. Ran, Phys. Rev. B **84**, 075129 (2011).
[44] W. Witczak-Krempa and Y. B. Kim, Phys. Rev. B **85**, 045124 (2012).
[45] P. Hosur and X. Qi, Comptes Rendus Phys. **14**, 857 (2013).
[46] S.-C. Zhang and J. Hu, Science **294**, 823 (2001).
[47] D. T. Son and B. Z. Spivak, Phys. Rev. B **88**, 104412 (2013).
[48] P. Hosur and X.-L. Qi, Phys. Rev. B **91**, 081106 (2015).
[49] B.-J. Yang and N. Nagaosa, Nat. Commun. **5**, 4898 (2014).
[50] S. Murakami and S. Kuga, Phys. Rev. B **78**, 165313 (2008).
[51] S. Murakami, Phys. E Low-Dimens. Syst. Nanostructures **43**, 748 (2011).
[52] R. Okugawa and S. Murakami, Phys. Rev. B **89**, 235315 (2014).
[53] S. M. Young, S. Zaheer, J. C. Y. Teo, C. L. Kane, E. J. Mele, and A. M. Rappe, Phys. Rev. Lett. **108**, 140405 (2012).
[54] Z. K. Liu, B. Zhou, Y. Zhang, Z. J. Wang, H. M. Weng, D. Prabhakaran, S.-K. Mo, Z. X. Shen, Z. Fang, X. Dai, Z. Hussain, and Y. L. Chen, Science **343**, 864 (2014).
[55] Z. K. Liu, J. Jiang, B. Zhou, Z. J. Wang, Y. Zhang, H. M. Weng, D. Prabhakaran, S.-K. Mo, H. Peng, P. Dudin, T. Kim, M. Hoesch, Z. Fang, X. Dai, Z. X. Shen, D. L. Feng, Z. Hussain, and Y. L. Chen, Nat. Mater. **13**, 677 (2014).
[56] M. Neupane, S.-Y. Xu, R. Sankar, N. Alidoust, G. Bian, C. Liu, I. Belopolski, T.-R. Chang, H.-T. Jeng, H. Lin, A. Bansil, F. Chou, and M. Z. Hasan, Nat. Commun. **5**, 3786 (2014).
[57] S. Borisenko, Q. Gibson, D. Evtushinsky, V. Zabolotnyy, B. Büchner, and R. J. Cava, Phys. Rev. Lett. **113**, 027603 (2014).

[58] Y. Sun, X.-Q. Chen, S. Yunoki, D. Li, and Y. Li, Phys. Rev. Lett. **105**, 216406 (2010).

[59] T. Kariyado and M. Ogata, J. Phys. Soc. Jpn. **81**, 064701 (2012).

[60] T. Kariyado, J. Phys. Conf. Ser. **603**, 012008 (2015).

[61] T. Kariyado and M. Ogata, Phys. Rev. Mater. **1**, 061201 (2017).

[62] T. H. Hsieh, J. Liu, and L. Fu, Phys. Rev. B **90**, 081112 (2014).

[63] C.-K. Chiu, Y.-H. Chan, X. Li, Y. Nohara, and A. P. Schnyder, Phys. Rev. B **95**, 035151 (2017).

[64] M. Oudah, A. Ikeda, J. N. Hausmann, S. Yonezawa, T. Fukumoto, S. Kobayashi, M. Sato, and Y. Maeno, Nat. Commun. **7**, 13617 (2016).

[65] C.-X. Liu, S.-C. Zhang, and X.-L. Qi, Annu. Rev. Condens. Matter Phys. **7**, 301 (2016).

[66] S. Hüfner, *Photoelectron Spectroscopy: Principles and Applications* (Springer, Berlin, Germany, 2003).

[67] A. Damascelli, Z. Hussain, and Z.-X. Shen, Rev. Mod. Phys. **75**, 473 (2003).

[68] N. P. Armitage, E. J. Mele, and A. Vishwanath, arXiv:1705.01111 (2017).

[69] H. Murakawa, M. S. Bahramy, M. Tokunaga, Y. Kohama, C. Bell, Y. Kaneko, N. Nagaosa, H. Y. Hwang, and Y. Tokura, Science **342**, 1490 (2013).

[70] D. Shoenberg, *Magnetic Oscillations in Metals* (Cambridge University Press, Cambridge, England, 1984).

[71] L. P. He, X. C. Hong, J. K. Dong, J. Pan, Z. Zhang, J. Zhang, and S. Y. Li, Phys. Rev. Lett. **113**, 246402 (2014).

[72] C. M. Wang, H.-Z. Lu, and S.-Q. Shen, Phys. Rev. Lett. **117**, 077201 (2016).

[73] M. Z. Hasan, S.-Y. Xu, and G. Bian, Phys. Scr. **2015**, 014001 (2015).

[74] A. Bansil, H. Lin, and T. Das, Rev. Mod. Phys. **88**, 021004 (2016).

[75] C. Nowka, L. Veyrat, S. Gorantla, U. Steiner, B. Eichler, O. G. Schmidt, H. Funke, J. Dufouleur, B. Büchner, R. Giraud, and S. Hampel, Cryst. Growth Des. **15**, 4272 (2015).

[76] R. Venkatasubramanian, T. Colpitts, E. Watko, M. Lamvik, and N. El-Masry, J. Cryst. Growth **170**, 817 (1997).

[77] H. Cao, R. Venkatasubramanian, C. Liu, J. Pierce, H. Yang, M. Zahid Hasan, Y. Wu, and Y. P. Chen, Appl. Phys. Lett. **101**, 162104 (2012).

[78] A. Szczerbakow and H. Berger, J. Cryst. Growth **139**, 172 (1994).

[79] A. Szczerbakow and K. Durose, Prog. Cryst. Growth Charact. Mater. **51**, 81 (2005).

[80] J. Nuss, C. Mühle, K. Hayama, V. Abdolazimi, and H. Takagi, Acta Crystallogr. Sect. B Struct. Sci. Cryst. Eng. Mater. **71**, 300 (2015).

[81] K. Eto, Z. Ren, A. A. Taskin, K. Segawa, and Y. Ando, Phys. Rev. B **81**, 195309 (2010).

[82] J. G. Analytis, J.-H. Chu, Y. Chen, F. Corredor, R. D. McDonald, Z. X. Shen, and I. R. Fisher, Phys. Rev. B **81**, 205407 (2010).

[83] N. P. Butch, K. Kirshenbaum, P. Syers, A. B. Sushkov, G. S. Jenkins, H. D. Drew, and J. Paglione,

Phys. Rev. B **81**, 241301 (2010).

[84] Y. Okamoto, A. Sakamaki, and K. Takenaka, J. Appl. Phys. **119**, 205106 (2016).

[85] G. Bruzzone and F. Merlo, J. Common Met. **48**, 103 (1976).

[86] A. Widera and H. Schäfer, Mater. Res. Bull. **15**, 1805 (1980).

[87] A. Velden and M. Jansen, Z. Für Anorg. Allg. Chem. **630**, 234 (2004).

[88] TOPAS, version 4.2 Bruker AXS, Karlsruhe, Germany, 2009.

[89] J. Cao, S. Liang, C. Zhang, Y. Liu, J. Huang, Z. Jin, Z.-G. Chen, Z. Wang, Q. Wang, J. Zhao, S. Li, X. Dai, J. Zou, Z. Xia, L. Li, and F. Xiu, Nat. Commun. **6**, 7779 (2015).

[90] T. Liang, Q. Gibson, M. N. Ali, M. Liu, R. J. Cava, and N. P. Ong, Nat. Mater. **14**, 280 (2015).

[91] S.-Y. Xu, Y. Xia, L. A. Wray, S. Jia, F. Meier, J. H. Dil, J. Osterwalder, B. Slomski, A. Bansil, H. Lin, R. J. Cava, and M. Z. Hasan, Science **332**, 560 (2011).

[92] T. Sato, K. Segawa, K. Kosaka, S. Souma, K. Nakayama, K. Eto, T. Minami, Y. Ando, and T. Takahashi, Nat. Phys. **7**, 840 (2011).

[93] J. Liu and D. Vanderbilt, Phys. Rev. B **90**, 155316 (2014).

[94] G. Xu, H. Weng, Z. Wang, X. Dai, and Z. Fang, Phys. Rev. Lett. **107**, 186806 (2011).

[95] M. Hirayama, R. Okugawa, S. Ishibashi, S. Murakami, and T. Miyake, Phys. Rev. Lett. **114**, 206401 (2015).

[96] Y. Sun, S.-C. Wu, M. N. Ali, C. Felser, and B. Yan, Phys. Rev. B **92**, 161107 (2015).

[97] A. A. Soluyanov, D. Gresch, Z. Wang, Q. Wu, M. Troyer, X. Dai, and B. A. Bernevig, Nature **527**, 495 (2015).

[98] S.-M. Huang, S.-Y. Xu, I. Belopolski, C.-C. Lee, G. Chang, T.-R. Chang, B. Wang, N. Alidoust, G. Bian, M. Neupane, D. Sanchez, H. Zheng, H.-T. Jeng, A. Bansil, T. Neupert, H. Lin, and M. Z. Hasan, Proc. Natl. Acad. Sci. **113**, 1180 (2016).

[99] B. Q. Lv, H. M. Weng, B. B. Fu, X. P. Wang, H. Miao, J. Ma, P. Richard, X. C. Huang, L. X. Zhao, G. F. Chen, Z. Fang, X. Dai, T. Qian, and H. Ding, Phys. Rev. X **5**, 031013 (2015).

[100] S.-Y. Xu, I. Belopolski, N. Alidoust, M. Neupane, G. Bian, C. Zhang, R. Sankar, G. Chang, Z. Yuan, C.-C. Lee, S.-M. Huang, H. Zheng, J. Ma, D. S. Sanchez, B. Wang, A. Bansil, F. Chou, P. P. Shibayev, H. Lin, S. Jia, and M. Z. Hasan, Science **349**, 613 (2015).

[101] B. Q. Lv, N. Xu, H. M. Weng, J. Z. Ma, P. Richard, X. C. Huang, L. X. Zhao, G. F. Chen, C. E. Matt, F. Bisti, V. N. Strocov, J. Mesot, Z. Fang, X. Dai, T. Qian, M. Shi, and H. Ding, Nat. Phys. **11**, 724 (2015).

[102] L. X. Yang, Z. K. Liu, Y. Sun, H. Peng, H. F. Yang, T. Zhang, B. Zhou, Y. Zhang, Y. F. Guo, M. Rahn, D. Prabhakaran, Z. Hussain, S.-K. Mo, C. Felser, B. Yan, and Y. L. Chen, Nat. Phys. **11**, 728 (2015).

[103] S.-Y. Xu, N. Alidoust, I. Belopolski, Z. Yuan, G. Bian, T.-R. Chang, H. Zheng, V. N. Strocov, D. S. Sanchez, G. Chang, C. Zhang, D. Mou, Y. Wu, L. Huang, C.-C. Lee, S.-M. Huang, B. Wang,

A. Bansil, H.-T. Jeng, T. Neupert, A. Kaminski, H. Lin, S. Jia, and M. Zahid Hasan, Nat. Phys. **11**, 748 (2015).

[104] L. Huang, T. M. McCormick, M. Ochi, Z. Zhao, M.-T. Suzuki, R. Arita, Y. Wu, D. Mou, H. Cao, J. Yan, N. Trivedi, and A. Kaminski, Nat. Mater. **15**, 1155 (2016).

[105] K. Deng, G. Wan, P. Deng, K. Zhang, S. Ding, E. Wang, M. Yan, H. Huang, H. Zhang, Z. Xu, J. Denlinger, A. Fedorov, H. Yang, W. Duan, H. Yao, Y. Wu, S. Fan, H. Zhang, X. Chen, and S. Zhou, Nat. Phys. **12**, 1105 (2016).

[106] A. Tamai, Q. S. Wu, I. Cucchi, F. Y. Bruno, S. Riccò, T. K. Kim, M. Hoesch, C. Barreteau, E. Giannini, C. Besnard, A. A. Soluyanov, and F. Baumberger, Phys. Rev. X **6**, 031021 (2016).

[107] I. Belopolski, S.-Y. Xu, Y. Ishida, X. Pan, P. Yu, D. S. Sanchez, H. Zheng, M. Neupane, N. Alidoust, G. Chang, T.-R. Chang, Y. Wu, G. Bian, S.-M. Huang, C.-C. Lee, D. Mou, L. Huang, Y. Song, B. Wang, G. Wang, Y.-W. Yeh, N. Yao, J. E. Rault, P. Le Fèvre, F. Bertran, H.-T. Jeng, T. Kondo, A. Kaminski, H. Lin, Z. Liu, F. Song, S. Shin, and M. Z. Hasan, Phys. Rev. B **94**, 085127 (2016).

[108] F. Y. Bruno, A. Tamai, Q. S. Wu, I. Cucchi, C. Barreteau, A. de la Torre, S. McKeown Walker, S. Riccò, Z. Wang, T. K. Kim, M. Hoesch, M. Shi, N. C. Plumb, E. Giannini, A. A. Soluyanov, and F. Baumberger, Phys. Rev. B **94**, 121112 (2016).

[109] Y. Wu, D. Mou, N. H. Jo, K. Sun, L. Huang, S. L. Bud'ko, P. C. Canfield, and A. Kaminski, Phys. Rev. B **94**, 121113 (2016).

[110] C. Wang, Y. Zhang, J. Huang, S. Nie, G. Liu, A. Liang, Y. Zhang, B. Shen, J. Liu, C. Hu, Y. Ding, D. Liu, Y. Hu, S. He, L. Zhao, L. Yu, J. Hu, J. Wei, Z. Mao, Y. Shi, X. Jia, F. Zhang, S. Zhang, F. Yang, Z. Wang, Q. Peng, H. Weng, X. Dai, Z. Fang, Z. Xu, C. Chen, and X. J. Zhou, Phys. Rev. B **94**, 241119 (2016).

[111] Z. Wang, Y. Sun, X.-Q. Chen, C. Franchini, G. Xu, H. Weng, X. Dai, and Z. Fang, Phys. Rev. B **85**, 195320 (2012).

[112] S.-Y. Xu, C. Liu, S. K. Kushwaha, R. Sankar, J. W. Krizan, I. Belopolski, M. Neupane, G. Bian, N. Alidoust, T.-R. Chang, H.-T. Jeng, C.-Y. Huang, W.-F. Tsai, H. Lin, P. P. Shibayev, F.-C. Chou, R. J. Cava, and M. Z. Hasan, Science **347**, 294 (2015).

[113] Z. Wang, H. Weng, Q. Wu, X. Dai, and Z. Fang, Phys. Rev. B **88**, 125427 (2013).

[114] K. Mullen, B. Uchoa, and D. T. Glatzhofer, Phys. Rev. Lett. **115**, 026403 (2015).

[115] C. Fang, Y. Chen, H.-Y. Kee, and L. Fu, Phys. Rev. B **92**, 081201 (2015).

[116] Y. Chen, Y. Xie, S. A. Yang, H. Pan, F. Zhang, M. L. Cohen, and S. Zhang, Nano Lett. **15**, 6974 (2015).

[117] H. Weng, Y. Liang, Q. Xu, R. Yu, Z. Fang, X. Dai, and Y. Kawazoe, Phys. Rev. B **92**, 045108 (2015).

[118] Y. Kim, B. J. Wieder, C. L. Kane, and A. M. Rappe, Phys. Rev. Lett. **115**, 036806 (2015).

[119] R. Yu, H. Weng, Z. Fang, X. Dai, and X. Hu, Phys. Rev. Lett. **115**, 036807 (2015).

[120] L. S. Xie, L. M. Schoop, E. M. Seibel, Q. D. Gibson, W. Xie, and R. J. Cava, APL Mater. **3**, 083602 (2015).

[121] Y.-H. Chan, C.-K. Chiu, M. Y. Chou, and A. P. Schnyder, Phys. Rev. B **93**, 205132 (2016).

[122] M. Zeng, C. Fang, G. Chang, Y.-A. Chen, T. Hsieh, A. Bansil, H. Lin, and L. Fu, arXiv:1504.03492 (2015).

[123] A. Yamakage, Y. Yamakawa, Y. Tanaka, and Y. Okamoto, J. Phys. Soc. Jpn. **85**, 013708 (2015).

[124] J. Zhao, R. Yu, H. Weng, and Z. Fang, Phys. Rev. B **94**, 195104 (2016).

[125] G. Bian, T.-R. Chang, H. Zheng, S. Velury, S.-Y. Xu, T. Neupert, C.-K. Chiu, S.-M. Huang, D. S. Sanchez, I. Belopolski, N. Alidoust, P.-J. Chen, G. Chang, A. Bansil, H.-T. Jeng, H. Lin, and M. Z. Hasan, Phys. Rev. B **93**, 121113 (2016).

[126] M. Hirayama, R. Okugawa, T. Miyake, and S. Murakami, Nat. Commun. **8**, 14022 (2017).

[127] G. Bian, T.-R. Chang, R. Sankar, S.-Y. Xu, H. Zheng, T. Neupert, C.-K. Chiu, S.-M. Huang, G. Chang, I. Belopolski, D. S. Sanchez, M. Neupane, N. Alidoust, C. Liu, B. Wang, C.-C. Lee, H.-T. Jeng, C. Zhang, Z. Yuan, S. Jia, A. Bansil, F. Chou, H. Lin, and M. Z. Hasan, Nat. Commun. **7**, 10556 (2016).

[128] Y. Wu, L.-L. Wang, E. Mun, D. D. Johnson, D. Mou, L. Huang, Y. Lee, S. L. Bud'ko, P. C. Canfield, and A. Kaminski, Nat. Phys. **12**, 667 (2016).

[129] A. Yamakage, Y. Yamakawa, Y. Tanaka, and Y. Okamoto, J. Phys. Soc. Jpn. **85**, 013708 (2015).

[130] D. Samal, H. Nakamura, and H. Takagi, APL Mater. **4**, 076101 (2016).

[131] P. Dziawa, B. J. Kowalski, K. Dybko, R. Buczko, A. Szczerbakow, M. Szot, E. Łusakowska, T. Balasubramanian, B. M. Wojek, M. H. Berntsen, O. Tjernberg, and T. Story, Nat. Mater. **11**, 1023 (2012).

[132] T. Liang, Q. Gibson, J. Xiong, M. Hirschberger, S. P. Koduvayur, R. J. Cava, and N. P. Ong, Nat. Commun. **4**, 2696 (2013).

[133] X. Xi, X.-G. He, F. Guan, Z. Liu, R. D. Zhong, J. A. Schneeloch, T. S. Liu, G. D. Gu, X. Du, Z. Chen, X. G. Hong, W. Ku, and G. L. Carr, Phys. Rev. Lett. **113**, 096401 (2014).

[134] T. Yoshida, K. Tanaka, H. Yagi, A. Ino, H. Eisaki, A. Fujimori, and Z.-X. Shen, Phys. Rev. Lett. **95**, 146404 (2005).

[135] V. N. Strocov, M. Shi, M. Kobayashi, C. Monney, X. Wang, J. Krempasky, T. Schmitt, L. Patthey, H. Berger, and P. Blaha, Phys. Rev. Lett. **109**, 086401 (2012).

[136] J. P. Perdew, K. Burke, and M. Ernzerhof, Phys. Rev. Lett. **77**, 3865 (1996).

[137] G. Kresse and J. Hafner, Phys. Rev. B **47**, 558 (1993).

[138] P. M. C. Rourke and S. R. Julian, Comput. Phys. Commun. **183**, 324 (2012).

[139] A. A. Abrikosov, Phys. Rev. B **58**, 2788 (1998).

[140] Y. L. Chen, J.-H. Chu, J. G. Analytis, Z. K. Liu, K. Igarashi, H.-H. Kuo, X. L. Qi, S. K. Mo, R. G. Moore, D. H. Lu, M. Hashimoto, T. Sasagawa, S. C. Zhang, I. R. Fisher, Z. Hussain, and Z. X. Shen, Science **329**, 659 (2010).

[141] M. N. Ali, J. Xiong, S. Flynn, J. Tao, Q. D. Gibson, L. M. Schoop, T. Liang, N. Haldolaarachchige, M. Hirschberger, N. P. Ong, and R. J. Cava, Nature **514**, 205 (2014).

[142] S.-Y. Xu, I. Belopolski, D. S. Sanchez, C. Zhang, G. Chang, C. Guo, G. Bian, Z. Yuan, H. Lu, T.-R. Chang, P. P. Shibayev, M. L. Prokopovych, N. Alidoust, H. Zheng, C.-C. Lee, S.-M. Huang, R. Sankar, F. Chou, C.-H. Hsu, H.-T. Jeng, A. Bansil, T. Neupert, V. N. Strocov, H. Lin, S. Jia, and M. Z. Hasan, Sci. Adv. **1**, e1501092 (2015).

[143] S. Souma, Z. Wang, H. Kotaka, T. Sato, K. Nakayama, Y. Tanaka, H. Kimizuka, T. Takahashi, K. Yamauchi, T. Oguchi, K. Segawa, and Y. Ando, Phys. Rev. B **93**, 161112 (2016).

[144] Y. Obata, R. Yukawa, K. Horiba, H. Kumigashira, Y. Toda, S. Matsuishi, and H. Hosono, Phys. Rev. B **96**, 155109 (2017).

[145] A. L. Friedman, J. L. Tedesco, P. M. Campbell, J. C. Culbertson, E. Aifer, F. K. Perkins, R. L. Myers-Ward, J. K. Hite, C. R. Eddy, G. G. Jernigan, and D. K. Gaskill, Nano Lett. **10**, 3962 (2010).

[146] D.-X. Qu, Y. S. Hor, J. Xiong, R. J. Cava, and N. P. Ong, Science **329**, 821 (2010).

[147] H. Tang, D. Liang, R. L. J. Qiu, and X. P. A. Gao, ACS Nano **5**, 7510 (2011).

[148] C. Shekhar, S. Ouardi, A. K. Nayak, G. H. Fecher, W. Schnelle, and C. Felser, Phys. Rev. B **86**, 155314 (2012).

[149] X. Huang, L. Zhao, Y. Long, P. Wang, D. Chen, Z. Yang, H. Liang, M. Xue, H. Weng, Z. Fang, X. Dai, and G. Chen, Phys. Rev. X **5**, 031023 (2015).

[150] C. Zhang, C. Guo, H. Lu, X. Zhang, Z. Yuan, Z. Lin, J. Wang, and S. Jia, Phys. Rev. B **92**, 041203 (2015).

[151] A. Narayanan, M. D. Watson, S. F. Blake, N. Bruyant, L. Drigo, Y. L. Chen, D. Prabhakaran, B. Yan, C. Felser, T. Kong, P. C. Canfield, and A. I. Coldea, Phys. Rev. Lett. **114**, 117201 (2015).

[152] J. Feng, Y. Pang, D. Wu, Z. Wang, H. Weng, J. Li, X. Dai, Z. Fang, Y. Shi, and L. Lu, Phys. Rev. B **92**, 081306 (2015).

[153] M. Novak, S. Sasaki, K. Segawa, and Y. Ando, Phys. Rev. B **91**, 041203 (2015).

[154] Z. Wang, Y. Zheng, Z. Shen, Y. Lu, H. Fang, F. Sheng, Y. Zhou, X. Yang, Y. Li, C. Feng, and Z.-A. Xu, Phys. Rev. B **93**, 121112 (2016).

[155] T. Coffey, Z. Bayindir, J. F. DeCarolis, M. Bennett, G. Esper, and C. C. Agosta, Rev. Sci. Instrum. **71**, 4600 (2000).

[156] J. Xiong, Y. Luo, Y. Khoo, S. Jia, R. J. Cava, and N. P. Ong, Phys. Rev. B **86**, 045314 (2012).

[157] Y. Ando, J. Phys. Soc. Jpn. **82**, 102001 (2013).

[158] S. Jeon, B. B. Zhou, A. Gyenis, B. E. Feldman, I. Kimchi, A. C. Potter, Q. D. Gibson, R. J. Cava, A. Vishwanath, and A. Yazdani, Nat. Mater. **13**, 851 (2014).

Acknowledgement

This study was carried out in *Hosono, Kamiya, Hiramatsu &Matsuishi Laboratory* at the Tokyo Institute of Technology from April 2013 to March 2018. Numerous people have contributed to this study.

First of all, I would like to thank my adviser Prof. ***Hideo Hosono*** for his great support, advice, and continuous encouragement for my research over the past five years. He taught me the essence of solid-state chemistry and physics. Moreover, I am grateful for the freedom he gave me and other members in our group to pursue individual interests in our research work. He allowed us to come up with our unique research projects, design experiments, and ask experts in relevant areas such as ARPES techniques and high-field experiments. He is always energetic, fair, and encouraging. I am very fortunate to have such a great adviser.

I am also deeply grateful to Associate Prof. ***Satoru Matsuishi*** for guiding me through my graduate studies. His comments always grasp the essence and allowed me to figure out what should be improved and what is lacking, which greatly deepened my understanding of materials science. The discussions with him led to many fruitful ideas and new results. I would like to express my sincere thanks to Prof. ***Toshio Kamiya*** and Associate Prof. ***Hidenori Hiramatsu*** for their kind guidance, discussions, and important suggestions.

I am indebted to Prof. ***Satoru Fujitsu***, Prof. ***Hideya Kumomi***, Prof. ***Toshiharu Yokoyama***, Associate prof. ***Masaaki Kitano***, Associate prof. ***Tomofumi Tada***, Associate prof. ***Hiroshi Mizoguchi***, Associate prof. ***Takayoshi Katase,*** Assistant Prof. ***Yoshitake Toda***, Assistant prof. ***Fuji Funabiki***, Assistant prof. ***Soshi Iimura***, Assistant prof. ***Keisuke Ide***, Assistant prof. ***Junghwan Kim***, Dr. ***Hechang Lei*** (currently at Renmin University of China), Dr. ***Fumitaka Hayashi,*** Dr. ***Jiangang Guo*** (currently at Chinese Acdemicy of Sciences)**,** Dr. ***Yanpeng Qi*** (currently at Max Planck Institute for Chemical Physics of Solids)**,** Dr. ***Zhang Xiao*** (currently at Beijing University of Posts and Telecommunications), Dr. ***Kosuke Matsuzaki***, Dr. ***Lu Yangfan***, Dr. ***Wu Jiazhen***, Dr. ***Taku Hanna*** (currently at ULVAC, Inc.), Dr. ***Yoshinori Muraba***, Dr. ***Sehoon Jeong*** (currently at Samsung Electronics Co., Ltd), Dr. ***JoonHo Ban*** and Dr. ***Hikaru Sato*** (currently at General Electric, Inc.) for their kind help and suggestions.

I also would like to thank, Mr. ***Junichi Ishida***, Mr. ***Takeshi Arai***, Mr. ***Yudai Tomota***, Mr. ***Nobuhiro Nakamura***, Mr. ***Hongsheng Yang***, Mr. ***Kota Hanzawa,*** Mr. ***Sang Won Park,*** Mr. ***Taehwan Jun,*** Mr. ***Takuya Nakao,*** Mr. ***Naoto Watanabe,*** Mr. ***Yutaro Kobayashi,*** Mr. ***Yoshiyasu Sato,*** Mr. ***Shogo Matsuda***, Mr. ***Takashi Muramoto***, Mr.

Sunagawa, Mr. ***Kyohei Ishikawa***, Mr. ***Takeshi Inoue***, Mr. ***Norihiko Miyokawa***, and other members of the *Hosono, Kamiya, Hiramatsu & Matsuishi Laboratory*.

Furthermore, I am indebted to Mr. ***Yuji Kondo*** for helping me to analyze the chemical composition. Also, I am very grateful to Prof. ***Hiroshi Kumigashira***, Associate prof. ***Koji Horiba***, Associate prof. ***Masaki Kobayashi***, Assistant prof. ***Makoto Minohara***, Assistant prof. ***Ryu Yukawa***, Dr. ***Miho Kitamura***, and other members of the *Kumigashira* Laboratory at KEK-PF for helping me with SX-ARPES experiments. In addition, I would like to express deep appreciation to Associate Prof. ***Yoshimitsu Kohama*** at ISSP for helping me with high-field measurements to observe SdH oscillations. I would like to thank Secretaries Ms. ***Kanako Ochiai***, Ms. ***Mayumi Nakano***, and Ms. ***Hanae Murayama***.

Finally, I would like to express utmost appreciation to my family and friends.

March 2018

Yukiko Obata

Publication Lists

Y. Obata, R. Yukawa, K. Horiba, H. Kumigashira, Y. Toda, S. Matsuishi, and H. Hosono
"ARPES studies of the inverse perovskite Ca_3PbO: Experimental confirmation of a candidate 3D Dirac fermion system"
Physical Review B **96**, 155109-1 – 155109-6, (2017).

Y. Obata, Y. Kohama, S. Matsuishi, and H. Hosono
"Shubnikov-de Haas oscillations in the 3D Dirac fermion system Ca_3PbO"
Physical Review B **99**, 115133-1 – 115133-6, (2019).

Y. Obata, S. Matsuishi, and H. Hosono
"Flux growth and magneto-transport properties of cubic antiperovskite Ca_3PbO single crystals"
Mater. Res. Bull. **106**, 1 – 6, (2018).

Presentation Lists

International presentation

Oral

Y. Obata, S. Matsuishi and H. Hosono
"Effects of Bi Substitution on Transport Properties of $Ca_3Pb_{1-x}Bi_xO$ Single Crystals"
The 10th International Conference on the Science and Technology for Advanced Ceramics (STAC-10), Yokohama, Japan, August 1–3, 2017.

Y. Obata, R. Yukawa, K. Horiba, H. Kumigashira, Y. Kohama, Y. Toda, S. Matsuishi, and H. Hosono
"Angle-Resolved Photoemission Spectroscopy and Shubnikov-de Haas Measurements of $Ca_3Pb_{1-x}Bi_xO$," American Physical Society March Meeting, Los Angeles, US, March 5–9, 2018.

Domestic presentation

Oral

小畑由紀子, 上田茂典, 松石聡, 戸田喜丈, 細野秀雄
「Ca_3PbO の輸送特性とバルク敏感光電子分光」
『日本物理学会 第 71 回年次大会』(2016/3/19~3/22, 宮城)

小畑由紀子, 湯川龍, 堀場弘司, 組頭広志, 松石聡, 戸田喜丈, 細野秀雄
「Ca_3PbO の軟 X 線角度分解光電子分光」
『 日本物理学会 第 72 回年次大会』 (2017/3/17~3/20, 大阪)

Poster

小畑由紀子, 湯川龍, 堀場弘司, 組頭広志, 松石聡, 戸田喜丈, 細野秀雄
「$Ca_3Pb_{1-x}Bi_xO$ の角度分解光電子分光」
『 第 11 回 物性科学領域横断研究会(領域合同研究会)』 (2017/11/17, 千葉)